Multiferroism in multifunctional rare earth metals-doped $BiFeO_3$ nanostructures

A Thesis Submitted to the

THAPAR UNIVERSITY, PATIALA

For the degree of

Doctor of Philosophy

By

Gurmeet Singh

Regn. No. 900912016

Under the supervision of

Dr. N. K.Verma

Senior Professor

School of Physics & Materials Science

Thapar University, Patiala - 147 004

INDIA

December 2013

DECLARATION

It is certified that the thesis is entirely my own and that the ideas and references cited herein have been duly acknowledged.

(Gurmeet Singh)

Attestation by supervisor

(Dr. N. K. Verma)

Senior Professor

School of Physics and Materials Science

Thapar University

Patiala – 147 004

INDIA

CERTIFICATE

This is to certify that the thesis entitled, "**Multiferroism in multifunctional rare earth metals-doped $BiFeO_3$ nanostructures**", submitted by Mr. Gurmeet Singh in the fulfilment of the requirement for the award of the degree of Doctor of Philosophy in the School of Physics and Materials Science, Thapar University, Patiala, is a record of candidate's own work carried out by him under my supervision and guidance. The matter presented in this thesis has not been submitted in part or full for the award of any degree in any other University or Institute.

Attestation by supervisor

(Dr. N. K. Verma)

Senior Professor

School of Physics and Materials Science

Thapar University

Patiala – 147 004

INDIA

Dedicated to my father

Late Mr. Manjit Singh Lotey

Acknowledgement

I humbly prostrate myself before the Almighty for HIS grace and abundant blessings which enabled me to complete this work successfully with my full satisfaction.

I would like to express my sincere gratitude and great appreciation to my research supervisor **Dr. N. K. Verma,** Senior Professor, School of Physics and Materials Science, Thapar University, Patiala for his outstanding scientific expertise, continuous guidance, patience, motivation, immense knowledge as well as wholehearted support. I successfully overcame many difficulties and learned a lot. His understanding, encouragement and personal attention have provided me, good and smooth basis for my PhD tenure. His unflinching courage and conviction will always inspire me, and I hope to continue to work with his noble thoughts. Through his Socratic questioning, Dr. Verma brought me closer to the reality, I had initially perceived, eventually enabling me to grasp its rich complexity. His capacity to combine critique with an immediate empathy and commitment towards co-workers and others engaged in struggle will always inspire me.

Uncountable words of thanks, love, and regards for **Dr. (Ms) Rama Verma,** for her motherly affection, homely care, motivation and blessings.

I, gratefully acknowledge the **Department of Science and Technology (DST)**, Government of India, for awarding me the **DST-INSPIRE** fellowship

I wish to express my gratefulness to **Dr. S.S. Sekhon**, Professor, University of the West Indies, West Indies, and **Dr. R. Thangaraj**, Professor, Guru Nanak Dev University , Amritsar, for introducing me to the fascinating world of research and their valuable guidance.

I am profoundly obliged to **Dr. K.K. Raina,** Director, Thapar University, Patiala, **Dr. Kulvir Singh**, Professor and Head, School of Physics and Materials Science, Thapar

University, Patiala, **Dr. O.P. Pandey**, Senior Professor, School of Physics and Materials Science, Thapar University, Patiala, for their good wishes and motivation.

I would like to thank my doctoral committee: **Dr. S.D. Tiwari,** Assistant Professor, School of Physics and Materials Science, **Dr. B. N. Chudasama,** Assistant Professor, School of Physics and Materials Science, and **Dr. Bonamali Pal,** Associate Professor, School of Chemistry and Biochemistry, for their encouragement, constructive criticism and inspirations. Loving support of faculty of School of Physics and Materials Science is appreciable.

I would like to thank **Dr. Sanjeev Kumar**, Associate Professor, PEC University of Technology, Chandigarh, and **Dr. Poonam Sharma,** Post-Doctoral Research Associate, Department of Chemistry, St. Francis Xavier University, Nova Scotia, Canada for their unmatched cooperation. I shall always remain indebted to **Ms. Meenu Dutta**, Lecturer, Govt. School, Pakhowal, Ludhiana, for her encouragement and inculcating me zeal for hard work.

I appreciate **Dr. Claudia Felser**, Professor, Johannes Gutenberg University of Mainz, Germany, **Dr. Ratnamala Chatterjee**, Professor, Indian Institute of Technology, Delhi, **Dr. S. R. Vadera,** Director, Defence Laboratory, Jodhpur, Rajasthan, and **Dr. Manoj Patra,** Scientist, Defence Laboratory, Jodhpur, Rajasthan for the electric and magnetic characterization. Most of the results described in this thesis would not have been possible without the help of laboratories at the institutes like, Punjab University, Chandigarh, IIT Delhi, JNU Delhi, NPL Delhi, JNCASR Bangalore, IISc Bangalore.

I am thankful to my senior lab-mates, **Dr. Zinki Jindal, Dr. Sanjeev Kumar** for their timely help and support especially in the early days when even the word `Research/PhD` was new to me. I would like to show my gratitude to my co-researchers, **Manveen Kaur, Lavanya Khanna**, **Kamaldeep Kaur, Imanpreet Kaur, Jaspal Singh, Gitanjali Dhir, Sunil Kumar,** for their lively discussions.

This thesis has gradually emerged amid the friendship of a few that provided the most lasting lessons. A special thanks to my friends, **Simrjit Singh** and **Sanjeev Kumar,** for their timely support and encouragement. It is a pleasure to mention the names of my good friends: **Parveer Kaur, Chandani Khurana, Rohit Singh, Inderpreet Singh, Alka Sharma, Tapsi Nagpal, Bhupinder Singh, Meenakshi Verma, Gurkirpal Singh Parmar, Harjinder Singh, Dr. Ravi Shukla.**

I would like to thank **Ms. Praveen Kumari**, **Mr. Vijay Kumar**, and the other secretarial staff of the School of Physics and Materials Science, Thapar University, Patiala.

I would like to pay high regards to my mother **Mrs. Balvinder Kaur Lotey** and my father late **Manjit Singh Lotey** for their love, affection and blessings. I am extremely happy to fulfil their ultimate desire that today, I achieve. The words of inspiration and encouragement told by my father in pursuit of excellence, still linger on.

I feel an immense admiration and humble obligation for my elder brother **Mr. Hardeep Singh Lotey,** sister-in-law **Mrs. Ramandeep Kaur Lotey** and younger brother **Mr. Manpreet Singh Lotey** for their support, co-operation throughout my research work to achieve great academic pursuits. The most special thanks to my wife **Dr. Jaspinder Kaur** for her love and understanding.

A special thanks to my nephews **Sehajpreet Singh Lotey**, **Simrjit Singh Lotey** and **Kulwant Singh Naggi**, whose smiling face always made me refreshing.

_____

Gurmeet Singh

List of Figures

List of Tables

Contents

List of Publications

I. Papers in SCI/refereed journals

1. Gurmeet Singh Lotey, NK Verma, Structural, magnetic, and electrical properties of Gd-doped $BiFeO_3$ nanoparticles with reduced particle size, Journal of Nanoparticles Research 14 (2012) 742 (Springer).
2. Gurmeet Singh Lotey, NK Verma, Phase-dependent multiferroism in Dy-doped $BiFeO_3$ nanowires, Superlattices and Microstructures 53 (2013) 184-194 (Elsevier).
3. Gurmeet Singh Lotey**,** NK Verma, Multiferroic properties of Tb-doped $BiFeO_3$ nanowires, Journal of Nanoparticles Research 15 (2013) 1553 (Springer).
4. Gurmeet Singh Lotey, NK Verma Multiferrosim in rare earth metals-doped $BiFeO_3$ nanowires, Superlattices and Microstructures 60 (2013) 60-66(Elsevier).
5. Gurmeet Singh Lotey, NK Verma, Magnetodielectric properties of rare earth metal-doped $BiFeO_3$ nanoparticles, Journal of Materials Science: Materials in Electronics, 24 (2013) 3723-3729 (Springer).
6. Gurmeet Singh Lotey, NK Verma, Magnetoelectric coupling in multiferroic $BiFeO_3$ nanowires, Chemical Physics Letters 579 (2013) 78-84 (Elsevier).
7. Gurmeet Singh Lotey, NK Verma, Magnetoelectric coupling in multiferroic Tb-doped $BiFeO_3$ nanoparticles, Materials Letter, 111 (2013) 55-58 (Elsevier).
8. G Dhir, Gurmeet Singh Lotey, P Uniyal, NK Verma, Size-dependent magnetic and dielectric properties of Tb-doped $BiFeO_3$ nanoparticles, Journal of Materials Science: Materials in Electronics, 24 (2013) 4386-4392 (Springer).
9. Gurmeet Singh Lotey, NK Verma**,** Structural, magnetic, electric and magnetodielectric properties of Dy-doped $BiFeO_3$ nanoparticles, Advances in Condensed Matter Physics, July 2013 (Minor Revision)
10. Gurmeet Singh Lotey, NK Verma, Magnetoelectric coupling in Dy-doped $BiFeO_3$ nanoparticles, July 2013 (Communicated).
11. Gurmeet Singh Lotey, NK Verma, Phase dependent Raman spectra study of Tb-doped $BiFeO_3$ nanoparticles (In Pipeline).

II. Papers in non-SCI journals

1. Gurmeet Singh Lotey, NK Verma, Structural, electrical, magnetic and multiferroism in Dy-doped $BiFeO_3$ nanoparticles, AIP Conference Proceeding 1536 (2013) 55-56 (American Institute of Physics).
2. Gurmeet Singh Lotey, G Dhir, NK Verma, Effect of reduced size and Ba-doping on multiferroic properties of $BiFeO_3$ nanoparticles, AIP Conference Proceeding 1536 (2013) 969-970 (American Institute of Physics).
3. Gurmeet Singh Lotey, NK Verma, Structural and multiferroics properties of rare earth metal ions (Gd^{3+}, Tb^{3+}, Dy^{3+})-doped $BiFeO_3$ nanoparticles, Excel India Publishers (2013) 2160-2165.
4. NK Verma, Imanpreet Kaur, Kamaldeep Kaur, Gurmeet Singh Lotey, Enhanced efficiency of Au-deposited $BiFeO_3$ nanoparticles based dye-sensitized solar cells, Advanced Materials Research 856 (2013) 184-187 (Trans Tech Publications).

III. Throughout the course of this work, I have also contributed to the following publications not directly related to the present thesis

1. Gurmeet Singh Lotey, N K Verma, Synthesis and characterization of $BiFeO_3$ nanowires and their applications in dye-sensitized solar cells, Materials Science in Semiconductor Processing, Accepted (2013).
2. Gurmeet Singh Lotey**,** N K Verma**,** Gd-doped $BiFeO_3$ nanoparticles - A novel material for highly efficient dye-sensitized solar cells, Chemical Physics Letters 574 (2013) 71-77 (Elsevier).
3. Gurmeet Singh Lotey, Jaspal Singh, N K Verma, Room temperature ferromagnetism in Tb-doped ZnO dilute magnetic semiconducting nanoparticles, Journal of Materials Science: Materials in Electronics, 24 (2013) 3611–3616 (Springer).
4. Gurmeet Singh Lotey, Zinki Jindal, Vaishali Singhi, N. K. Verma, Structural and photoluminescence properties of Eu-doped ZnS nanoparticles, Materials Science in Semiconductor Processing, Accepted (2013) (Elsevier).
5. Kamaldeep Kaur, Gurmeet Singh Lotey, NK Verma, Structural, magnetic, dielectric and magnetodielectric properties of Gd-doped CdS nanorods, Materials Science in Semiconductor Processing, 19 (2014) 6-10 (Elsevier).

6. Kamaldeep Kaur, Gurmeet Singh Lotey**,** NK Verma, Ferromagnetism in Gd-doped CdS dilute magnetic semiconducting nanorods, Journal of Materials Science: Materials in Electronics, DOI 10.1007/s10854-013-1587-2, (2013) (Springer), .
7. P Uniyal, Gurmeet Singh Lotey, A Gautam, NK Verma, K L Yadav, Multiferroic properties of $(Bi_{0.9}Gd_{0.1}FeO)_{1-x}(BaTiO_3)_x$ ceramics, Journal of Superconductivity and Novel Materials, DOI 10.1007/s10948-013-2311-4 (2013) (Springer).
8. Kamaldeep Kaur, Gurmeet Singh Lotey, NK Verma, Structural, optical and magnetic properties of cobalt-doped CdS dilute magnetic semiconducting nanorods, Materials Chemistry and Physics, 143 (1) (2013) 41-46 (Elsevier).
9. S Singh, Noor Jahan, Atul Khanna, Gurmeet Singh Lotey, N K Verma,Room temperature ferromagnetic behavior of indium-doped SnO_2 dilute magnetic semiconductor nanocrystalline thin films, Chalcogenide Letters 9 (2) (2012) 73 – 78 (Forum of chalcogeniders)
10. P Sharma, Gurmeet Singh Lotey, S Singh, N K Verma, Solution-combustion: the versatile route to synthesize silver nanoparticles, Journal of Nanoparticles Research 13 (10) (2011) 2553–2561 (Springer).
11. Gurmeet Singh Lotey, N K Verma, Fabrication and characterization of Cu-CdSe-Cu nanowire heterojunctions, Journal of Nanoparticles Research 13(10) (2011) 5397-5405 (Springer).
12. S Kumar, D Saini**,** Gurmeet Singh Lotey,N K Verma, Electrochemical synthesis of copper nanowires in anodic alumina membrane and their impedance analysis, Superlattices and Microstructures50 (6) (2011) 698-702 (Elsevier).
13. J Singh, Gurmeet Singh Lotey,N K Verma, Structural, optical and magnetic properties of Cr-doped CdSe nanoparticles, Digest Journal of Nanomaterials and Biostructures, 6(4) (2011) 1733-1740 (Forum of chalcogeniders)

IV. Papers in conference proceedings

1. Gurmeet Singh Lotey. NK Verma, Magnetoelectric coupling in rare earth ion substituted $BiFeO_3$ nanostructures, 6^{th} European School of Multiferroics (ESMF6), Martin-Luther University, Halle-Wittenberg, Germany, 21-26 July (2013).

2. Gurmeet Singh Lotey, Z Jindal, V Kumar, NK Verma, Study on room temperature magnetic behaviour of Tb-doped ZnO nanoparticles, Nanotech Conference & Expo 2012, 18-21 June, Santa Clara, CA, USA (2012).
3. Gurmeet Singh Lotey, NK Verma, Size dependent multiferroic behavior of Dy-doped $BiFeO_3$ nanoparticles, International Conference on Frontiers of Nanoscience, Nanotechnology and their applications (NanoSciTech-2012) Panjab University, Chandigarh, 15-18 February (2012).
4. Gurmeet Singh Lotey, NK Verma, Study on size dependent structural and magnetic properties of Dy-doped $BiFeO_3$ nanoparticles, International Conference and Workshop on Nanostructured Ceramics and other Nanomaterials (ICWNCN 2012), University of Delhi, Delhi, 13-16 March (2012).
5. Gurmeet Singh Lotey, NK Verma, Growth and characterization of highly ordered CdS nanowires embedded in anodic alumina membrane by non-galvanic technique, International Conference on Composites and Nanocomposites (ICNC-2011), IMSE, Kottayam, Kerala, India, 7-9 January (2011) Page no.22.
6. Gurmeet Singh Lotey, NK Verma, Template assisted electrochemical synthesis of ZnTe nanowires and their optical band gap determination, International Conference on Emerging Trends in Mechanical Engineering (ICETME-2011), Deptt.of Mech. Engg., Thapar University, Patiala, 24-26 February (2011) Page no. 98.
7. Gurmeet Singh Lotey, NK Verma, Room temperature magnetic behavior of Tb-doped ZnO nanoparticles, National Conference on Recent Advances in Polymer Nanocomposites (NCPN-1), Department of Physics, Zakir Hussian College, University of Delhi, 14-15 January (2011) Page no. 50-54.
8. Gurmeet Singh Lotey, NK Verma, Size dependent multiferroic properties of Gd doped $BiFeO_3$ nanoparticles, National Seminar on Advanced Materials and Devices (NSAMD-2011) GVM Girls College, Sonepat, Haryana, 3-4 July (2011), Page no. 23.
9. Gurmeet Singh Lotey, NK Verma, Study on size dependent magnetic and electrical properties of Gd-doped $BiFeO_3$nanoparticles, International Conference on Advances in Materials & Manufacturing Technology (AMMT-2011), Department of Mechanical Engineering, Chitkara University, Punjab, 20-21 July (2011) Page no.186-189.

10. Gurmeet Singh Lotey, NK Verma, Study on size dependent multiferroic behavior of Tb-doped $BiFeO_3$ nanoparticles, National Conference on Nanoscience Fundamentals & Applications (NCNFA-2011), Department of Applied Sciences Chitkara University, Punjab, 23-24 July (2011) Page no.25.
11. Gurmeet Singh Lotey, NK Verma, Study on size dependent structural and magnetic properties of Dy-doped $BiFeO_3$ nanoparticles, International Conference on Energy-Efficient Materials Manufacturing Methods & Machineries for Ceramics Industries (IC2E4MCI-11), Indian Ceramics Society, Agra, India, 19-22 December (2011).
12. Gurmeet Singh Lotey, NK Verma, Study on multiferroic properties of Dy-doped $BiFeO_3$ nanoparticles, Winter School on Chemistry and Physics of Materials-2011, JNCASR, Bangalore 5-10 December (2011) Page no. 59.
13. Gurmeet Singh Lotey, NK Verma, Synthesis and Characterization of Cu-CdSe-Cu nanowires by Galvanic technique, International Conference and School on Nucleation, aggregation and Growth (NAG-2010), JNCASR, Bangalore, India, 26 July to 6 August (2010) Page no. 49.

Abstract

In the development towards device miniaturization and high-density data storage system, it becomes highly desirable to integrate multifunctions in a single material. Multifunctional materials are the demand of future technology. Nanoscience environment provides more platforms to explore multifunctionality nanostructured multiferroics.

Bismuth ferrite ($BiFeO_3$) is hitherto the most studied multiferroic material as well as so far the only known single compound exhibiting room temperature multiferroism. However, $BiFeO_3$ is not explored for practical device applications due to several issues such as high leakage current density, secondary phase impurities, chemical fluctuations, low magnetoelectric coupling, and also the inhomogeneous magnetic spin structure. These issues should be resolved before realization in devices. Efforts have been made to overcome the above problems using substitution. These may lower the leakage current density, oxygen vacancies, and enhances the multiferroism properties. But the cancellation of magnetism due to spiral spin structure, with an incommensurate spiral period of 62 nm superimposed on the antiferromagnetic ordering, and the low magnetoelectric coupling, are still challenges of this field.

The incommensurate spiral spin structure and antiferromagnetic ordering in $BiFeO_3$ can be broken and high magnetoelectric coupling may be achieved if the size of the $BiFeO_3$ nanostructure should be less than that of the spin-spiral period, i.e., <62 nm, and simultaneously doping of rare earth metal ions will further enhance magnetoelectric coupling.Therefore, this thesis focuses the synthesis of $BiFeO_3$ nanostructures viz., nanoparticles and nanowires, and study of their multiferroic properties. The doping of rare earth metal ions (Gd^{3+}, Tb^{3+}, Dy^{3+}) has been done, and, the effect of doping and reduced size of $BiFeO_3$ nanostructures (< 62 nm) on their structural, magnetic, electric, dielectric and multiferroics properties, presented.

Preface

This thesis presents the multiferroism in multifunctional rare earth metal-doped $BiFeO_3$ nanostructures viz., nanoparticles and nanowires. The effect of doping of rare earth ions on the multiferroic properties of $BiFeO_3$ nanostructures has been investigated. The present thesis is divided into five chapters:

Chapter 1: Introduction

Deals with the introductory aspects and literature survey on multiferroic materials with specific attention paid on $BiFeO_3$ vis-à-vis their structure, multiferroic properties and applications.

Chapter 2: Synthesis and experimental techniques

Deals with the techniques used for synthesis and characterization of pure and rare earth metals doped-$BiFeO_3$ nanostructures. Pure and rare earth metals-doped $BiFeO_3$ ($Bi_{1-x}RE_xFeO_3$) nanoparticles (RE=Gd^{3+}, Tb^{3+}, Dy^{3+})with x = 0 to 0.15 have been synthesized by sol-gel method, while colloidal-dispersion capillary force-induced filling of anodic alumina oxide (AAO) template technique have been adopted for the synthesis of $Bi_{1-x}RE_xFeO_3$ nanowires. To understand the potential of synthesised nanoparticlesand nanowires, a deeper knowledge of their properties is required. Therefore, the synthesized nanoparticles and nanowires of pure and RE-doped $BiFeO_3$ have been characterized by their crystallographic structure, elemental and compositional, morphological, electrical, magnetic and magnetoelectric coupling properties. The techniques used include x-ray diffraction (XRD), scanning electron microscopy (SEM), transmission electron microscopy (TEM), high-resolution TEM (HRTEM) microscopy, x-ray photoelectron spectroscopy (XPS), superconducting quantum interface device (SQUID), polarization versus applied electric field (P–E) hysteresis loops, leakage current density versus applied electric field (J-E) characteristics, dielectric, magnetoelectric coupling coefficient (MD) and magnetoelectric coupling (ME) coefficient measurements.

Chapter 3: **Multiferroism in rare earth metal doped $BiFeO_3$ nanoparticles**

Deals with the study of multiferroic properties of rare earth metal ions (Gd^{3+}, Tb^{3+}, Dy^{3+})-doped $BiFeO_3$ nanoparticles synthesized by the sol-gel method. The effect of rare earth metal ion doping as well as the nanosize of the as-synthesized nanoparticles on morphology, structure,

magnetic, electric, dielectric and magneto-dielectric/electric coupling properties have been investigated. Synthesized nanoparticles have been found to possess spherical morphology with average particle size lying between 15- 50 nm. Structural study reveals that the doping of the rare earth metal ions in $BiFeO_3$ nanoparticles results in structural transformation from rhombohedral to orthorhombic phase. Magnetic study confirms that the synthesized nanoparticles exhibit well saturated hysteresis loops and possess ferromagnetic character. Dielectric measurements show that doping results in high dielectric constant as compared to that of pure $BiFeO_3$. To check the magnetoelectric coupling in the synthesized nanoparticles, magnetodielectric and magnetoelectric coefficient measurements have been done. The observed trend in the properties of the synthesized nanoparticles has been explained on the basis of doping of rare earth metal ions, structural transformation as well as the size of the synthesized nanoparticles.

Chapter 4:Multiferroism in rare earth metal doped $BiFeO_3$ nanowires

Deals with the study of magnetoelectric coupling in pure and rare earth metal ions (Gd^{3+}, Tb^{3+}, Dy^{3+})-doped $BiFeO_3$ nanowires synthesized by colloidal dispersion template-assisted technique. The effects of doping of rare earth metal ions as well as the nanosize of the synthesized nanowires on structural, magnetic, electric, dielectric and magneto-dielectric/electric coupling have been investigated. For the comparative study, nanowires of size, 100 nm (bulk in the present case), and 20 nm have been synthesized. Doping of the rare earth metal ions, in $BiFeO_3$ nanowires, results in structural transformation from rhombohedral to orthorhombic phase. Magnetic study confirms that the bulk nanowires possess antiferromagnetic behaviour. The reduction in the size of nanowires from 100 nm to 20 nm, and, at the same time, doping of rare earth metal ions, results in ferromagnetism in the synthesized nanowires. The dielectric measurements also show that doping results in high dielectric constant as compared to that of the pure $BiFeO_3$. To check the magnetoelectric coupling in the synthesized nanowires, magnetodielectric and magnetoelectric coupling coefficients have been measured.

Chapter 5: Conclusions and future scope

Presents the brief summary of the results obtained, as described in chapters 3 and 4. At the end of this chapter, future scope of the work has also been discussed.

Chapter 1
Introduction

Overview

This chapter deals with the introductory aspects and literature survey on multiferroic materials with specific attention paid on $BiFeO_3$ vis-à-vis their structure, multiferroic properties and applications.

1.1 Background

Multifunctional materials are the materials which perform multiple functions simultaneously when externally stimulated by electric, magnetic, stress fields. These materials are the demand of future technological devices and have attracted great attention due to their huge applications in intelligent devices. Multifunctionality is a milestone for modern electronics. In the development towards device miniaturization and high density data storage system, it becomes highly desirable to integrate multifunctions in a single material. The Information and data storage technology is a foundation of modern society. Presently, there are two kinds of memory systems used in computers viz., ferroelectric random access memories (FeRAMs) and magneto-resistance random access memories (MRAMs). Both have their own advantages and disadvantages. The high speed and large data storage capacity of computers is demand of the hour. The writing speed of the FeRAMs is faster than MRAMs, but readability is poor. On the other hand, readability with MRAMs is easier, but high magnetic field is required to write information. This necessitates that there is need of a memory device system that possess the best functionalities of FeRAMs and MRAMs, i.e., writing by ferroelectric means and reading by magnetic means [1-9]. Therefore, the present technology demands one such material that simultaneously possess non-volatile, robust, fast, less energy consuming and miniature in size. Multiferroics materials possess both the functionalities of FeRAMs and MRAMs and are the requisites one to design futuristic memory devices. This would results in data storage system that possesses high writing speed, low energy consumption and results into device miniaturization [4-10]. Nanostructured materials are believed to be the futuristic materials possessing at least one dimension in the nano-regime (1-100 nm). The appropriate control of size, shape and their dimensionality leads to tuning of their physical, chemical, electronic, electrical, dielectric, magnetic or magnetoelectric properties as compared to their bulk counterpart. This happens precisely due to the large surface to volume ratio, quantum confinement and high chemical reactivity. The changes in size and shape can further be harnessed for improving the existing technology, and have potential for extremely broad range of promising applications, which justify a rapidly expanding research at the nanoscale. The ability to engineer the desired properties in nanomaterials, their easiness in fabrication as well as integration on integrated circuits (ICs) makes them ideal candidates for future nanoelectronics [11-13].

1.2 Multiferroism

"Multiferroics" term is coined by Schmid [14]. Multiferroics are the materials possess at least two ferroic order, i.e., ferroelectricity, ferromagnetism, ferroelasticity [14, 15].

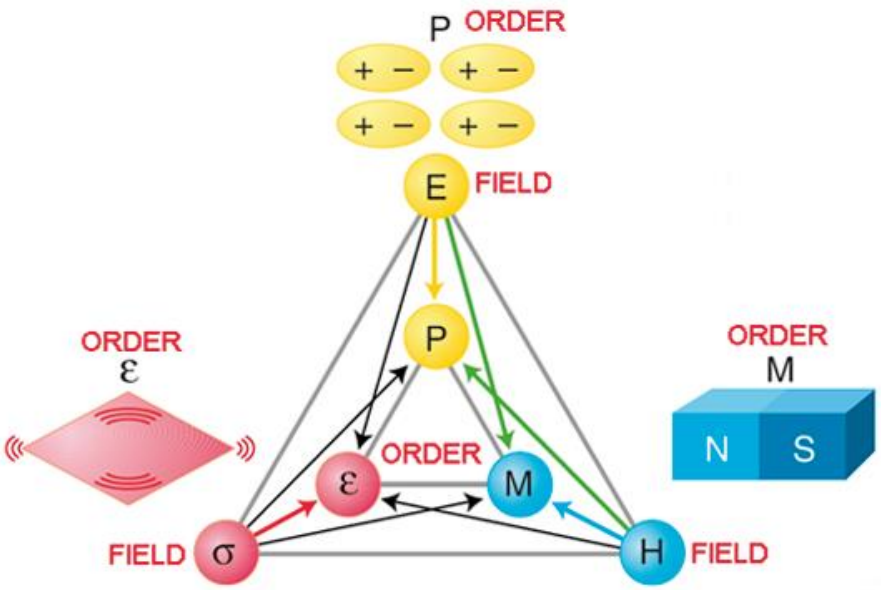

Figure 1.1 Magnetoelectric coupling between different ferroic orders and fields [15]

However, multiferroism is a mutually exclusive phenomenon, owing to the contrast between prerequisites of ferroelectricity and ferromagnetism, which make these materials rare [15, 16] (Figure 1.1). In 1984 the magnetoelectricity has been predicted by Pierre Curie [17]. Magnetoelectricity in Cr_2O_3 was theoretically and experimentally confirmed in 1959-1960 by Dzyaloshinsky and Astrov, respectively [14, 18-19]. Schmid, in 1966 experimentally observed magnetoelectric effect in nickel-iodine boracite ($Ni_3B_7O_{13}I$) [14, 20, 21]. However, due to the very small magnetoelectric coupling occurring in the materials and thereby difficulties in the implementation of their applications, the research activities in this field went into decline [22-24]. The revival of interest in this field has been initiated by the theoretical investigation by NA Hill in 2000 [24]. Nanostructured multiferroics, owning to their smaller size and the strong magnetoelectric coupling, open up exciting innumerable ways for designing future nanoelectronic and spintronic device applications. The semiconductor-based electronic industry is under threat as we are at the verge of fundamental limit of integration (i.e., the number of

device components such as transistors on integrated circuit). Therefore, for the miniaturization and high performance of electronic devices either a new technology or multifunctional materials are required. Multiferroic nanostructure materials with strong magnetoelectric coupling in different ferroic orders are requisite ones and have the potential to explore their applications in nanoelectronic and spintronic devices such as field effect transistors, electrical switching, nanoelectronics, magnetoelectric random access memories (MERAMs), sensors. Multiferroics enable "four-state memories" based on magneto-resistance and electro-resistance because of the four different combinations of magnetisation and polarisation [1, 3-5, 10-13, 22, 25-30].

The enthusiasm to work in this research area has been arisen due to their multifunctionality and unprecedented integration density possible at nanoscale [4-6, 10-12, 22, 30-34].The fundamental understanding of materials at the nanoscale will be core knowledge, enabling technological advancements in memory storage systems (e.g. spintronics). Moreover, the stability of the ferroic ordering phenomena and the underlying mechanisms responsible for multiferroism and magnetoelectric coupling at nanoscale is still at research level. Such insight is vital to the search for new and improved material systems. Moreover, understanding the behavior of ferroic ordering phenomena at the nano-scale is of outmost importance to the ever ongoing miniaturization of electronic devices [1-8, 11-13, 25-27, 35].

1.3 Bismuth Ferrite ($BiFeO_3$)

Bismuth ferrite ($BiFeO_3$) is the hitherto most studied multiferroic material as well as the only known single compound exhibiting room temperature multiferroism. Although many researchers anticipated strong magnetoelectric coupling in $BiFeO_3$, until the first evidence for this coupling in 2003 by Ramesh group [36]. The unexpectedly large remnant polarisation with large ferromagnetism than bulk counterpart has been reported. The observed enhancement is corroborated by first principle calculations and found to originate from small changes in lattice parameters. $BiFeO_3$ possess rhombohedral distorted perovskite structure with Curie temperature (TC ~ 830◦C). It is G-type antiferromagnetic with Neel temperature (TN ~ 370◦C) spiral-modulated spin structure. This is encouraging to use $BiFeO_3$ for multiferroics-based devices [5, 15-16, 24, 36-40].

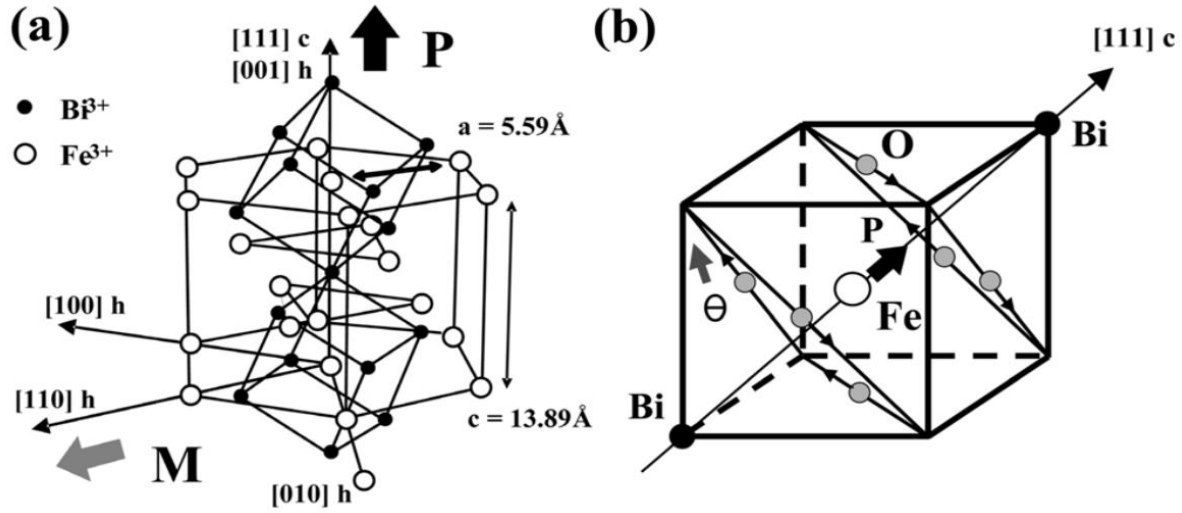

Figure 1.2 Hexagonal and pseudocubic crystallographic representations of $BiFeO_3$ with R*3c* symmetry [38, 39]

Figure 1.2 (a) shows the hexagonal and pseudo-cubic structure of $BiFeO_3$ with R*3c* symmetry. It shows that the spontaneous polarization in $BiFeO_3$ develop along the hexagonal $[001]_h$ direction or its equivalently direction $[111]_c$ in pseudo-cubic, due to the displacement of Bi, Fe and O relative to one another [38, 39]. Figure 1.2 (a) shows the unit cell of $BiFeO_3$ $[001]_h$, $[100]_h$, $[110]_h$, $[010]_h$ (hexagonal axes). The oxygen atoms occupy face-centered sites. Figure 1.2 (b) shows the schematic of pseudo-cubic structure of $BiFeO_3$ revealing a tilting of the oxygen octahedron about the threefold $[111]_c$ axis [38, 39]. The rhombohedral $BiFeO_3$ possess spiral spin-density wave of a wavelength (~620 Å) [15-16, 24-25, 34, 36, 38, 40-42] with its propagation along the hexagonal $[110]_h$ direction as shown in Figure 1.2. The R*3c* symmetry is further characterized by an anti-ferrodistortive clockwise tilting (θ) of the FeO_6 octahedron unit along the threefold pseudo-cubic $[111]_c$ direction (equivalently, $[001]_h$ direction) (Figure 1.2(b) [15-16, 24-25, 34, 36, 38, 42-43]. The magnetic structures of $BiFeO_3$ reveals that the neighboring spins are arranged as an antiparallel with respect to each other and this resulting in G-type antiferromagnetic ordering (Figure 1.3) [10, 14, 39, 40, 43-45]. The bulk $BiFeO_3$ is antiferromagnetic. The G-type antiferromagnetic spin structure of $BiFeO_3$ leads to cooperative magnetism in $BiFeO_3$; it originates from the half-filled and localized ($t^2_{2g}e^2g$) Fe^{3+}. The Fe^{3+} ions in the high spin state prefer to form the G-type antiferromagnetic ordering as the Pauli Exclusion

Principle allows the transfer of electron to the neighbouring ion in an antiparallel direction only. Neutron diffraction revealed that $BiFeO_3$ has a long-wavelength modulation that forms a spin cycloid with a wave-vector that is oriented along $[110]_h$, which is perpendicular to the $[111]_c$, as shown in Figure 1.3 (b). This modulation results in a zero value for the volume-averaged magnetoelectric effect and spontaneous magnetization [44-46].

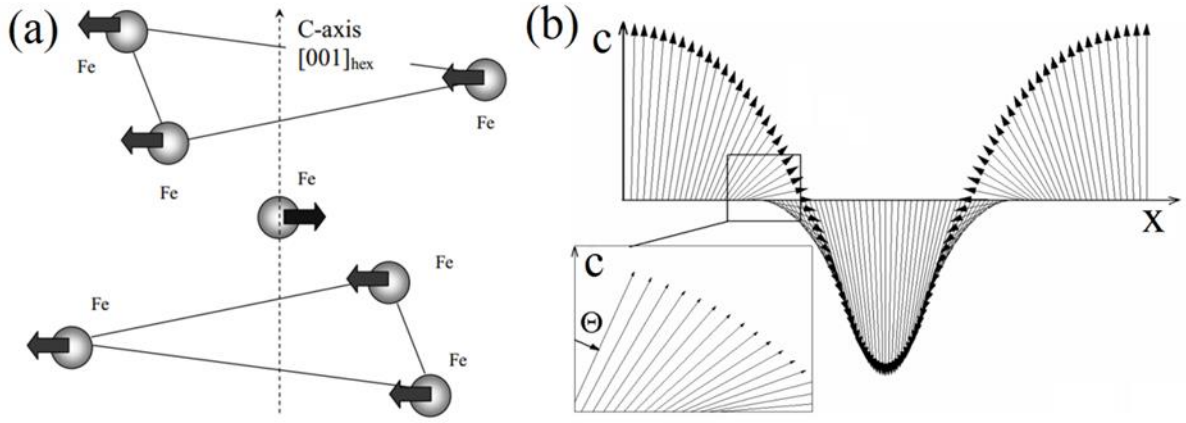

Figure 1.3 (a) Magnetic structure of $BiFeO_3$ and (b) long range magnetic order: incommensurate spin cycloid. The arrows represents the antiferromagnetic vector L and its orientation in space $\theta = \theta(x)$ [38, 39]

1.3.1. Ferroelectricity in $BiFeO_3$

The ferroelectric polarization in the bulk $BiFeO_3$ is along the diagonals of the perovskite unit cell ($[111]_{pseudocubic}/[001]_{hexagonal}$). As explained in section 1.3.1 that the spontaneous polarization in $BiFeO_3$ is developed along the hexagonal $[001]_h$ direction or equivalently along the pseudo-cubic $[111]_c$ direction, due to the displacement of Bi, and Fe, O relative to one another. The high ferroelectric Curie temperature observed in $BiFeO_3$ may refer to the large polarization since other typical ferroelectrics with such Curie temperature have a polarization about 100 μCcm^{-2}. Ferroelectricity in the bulk $BiFeO_3$ measured in 1960s and 1970s reveals their very small values of the polarization, $Pr \sim 6\mu Ccm^{-2}$ [40, 47]. The reason for this small polarization is possibly due to the high leakage current as a result of defects and the non-stoichiometry of the test materials.

There are numerous reports are available with conflicting results and the observed polarization explained on the basis of different factors [15-16, 34, 36, 40-42].

1.3.2. Magnetoelectric coupling in $BiFeO_3$

The value of magnetoelectric coupling in bulk $BiFeO_3$ is very small. The basic cause behind this is the cycloidal modulation of the spin structure that prevents a macroscopic weak ferromagnetic moment and linear magnetoelectric effect (Figure 1.3). However, at very large magnetic fields, above 20 T, the cycloidal modulation is suppressed and linear magnetoelectric coupling is possible.

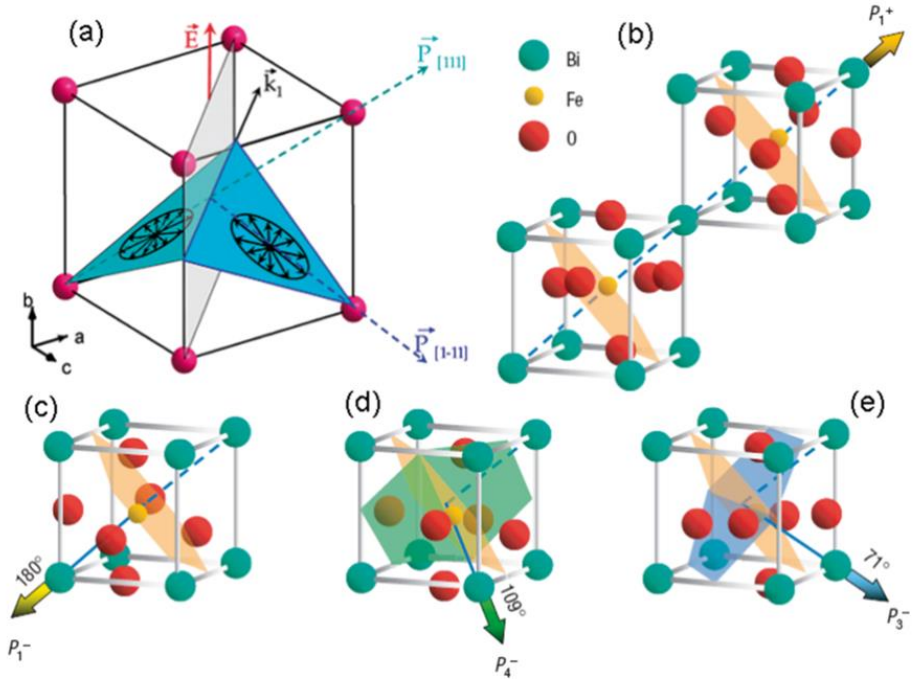

Figure 1.4 (a) 71° domain wall (light grey) and polarisation vectors with pseudo-cubic indices (b-d) The antiferromagnetic plane is normal to the polarisation and does not change with 180° switching (b) ↔ (c), but rotates when the ferroelastic state is altered (d) and (e) [52, 53]

The possible origin of the cycloidal spin structure is due to be the ferroelectric polarisation, as polarisation can couple to magnetisation gradients and induce the spin cycloid [40, 48-49]. $BiFeO_3$ is a proper ferroelectric with weak ferromagnetism (antiferromagnetic) due to the Dzyaloshinskii-Moriya interactions. It is theoretically found that the direction of the weak

ferromagnetic moment can be reversed by switching the direction of antiferrodistortive rotation of the FeO_6 octahedra. However, this is invariant under 180° switching of the direction of polar displacements of the Bi^{3+} and Fe^{3+} cations [50]. The exact mechanism of magnetoelectric coupling in $BiFeO_3$ is not fully understood yet. Magnetoelectric coupling in $BiFeO_3$ is mediated by magnetostriction and piezoelectricity [51]. The theory behind these effects is subtle.

The special about $BiFeO_3$ is that, in addition to the canting, there is also a ferroelectrically induced spin cycloid that averages out the local canted magnetism (Figure 1.4) [7, 49-55]. Although the cycloid averages out the macroscopic canting moment, this is locally still present at the unit-cell level (Figure 1.4). High magnetic fields can destroy the cycloid, thereby recovering the canted state. In this state, the linear magnetoelectric is allowed, so both effects in (Figure 1.4) are consistent with each other. The spin cycloid can also be destroyed by doping [56-57] or by epitaxial strain, [58] so fully strained epitaxial thin films can in principle display a weak remnant magnetization, although is not as high as initially reported [58].

1.4. Motivation of this thesis

In spite of the many investigations spanning nearly 50 years, the multiferroic properties of $BiFeO_3$ have not been realized: except under extremely high field. In a nutshell, this disappointment is due to the trapping of the magnetic vector and linear magnetoelectric interactions within a spin cycloid: which can be destabilized at high fields. It is fundamental that electronic configurations that favour magnetism are antagonistic to those favour polarization – compromise is necessary [15-16, 37].

In the search of multifunctional futurist multiferroic materials, $BiFeO_3$ is one of the scariest, possess a prodigious attraction, as it exhibits spontaneous polarization and weak ferromagnetism (antiferromagnetism) with rhombohedral perovskite structure having space group R*3c*, which has been a great attraction for the scientific community in recent years. Incorporation of $BiFeO_3$ into practical device application has been mired by leakage problems that lead to low resistivity - presumably due to defects, secondary impurities and non-stoichiometry related issues. $BiFeO_3$ also could not be exploited for device applications due to other major problems such as weak magnetization – it being essentially an antiferromagnetic below T_N, large loss factor - because of oxygen non-stoichiometry, and low magnetoelectric coupling [3]. Difficulties persist as the magneto-electric exchange and magnetism are locked within its spin cycloid structure. The

electronic structures/configurations, those favour magnetism, are antagonistic to ferroelectricity; thus, an appropriate compromise between them is badly needed. Several research groups have tried A-site (Bi-site) or B-site (Fe-site) substitution of rare-earth/alkaline/alkali metal-ions to modify the multiferroic properties of $BiFeO_3$; it minimizes the conductivity and the loss factor, improves the ferroelectric and ferro/antiferromagnetic properties, which in turn enhance the magnetoelectric coupling at room temperature.

The substitution of the rare-earth element for Bi-site eliminating the secondary phases; structural and phase transition (from rhombohedral to orthorhombic or tetragonal) improve its ferroelectric properties; increases magneto-crystalline anisotropy; destroy the spin-cycloidal structure; as well as resulting in substitution-induced suppression of spin-cycloid structure. The most effective way to induce spontaneous magnetization in $BiFeO_3$ is related to the substitution of such ions (say rare-earth elements), which have a large difference in size as compared to the size of Bi^{3+} ions [3].This necessitates the use of rare earth metal ions having smaller size than Bi^{3+} (R_{Bi}^{3+} = 0.103 nm) ions, as the most appropriate choice among the rare earth elements and the motivation for present thesis. However, existing literature does not give a clear understanding of size, doping and crystal structure dependent multiferroism in rare earth metal ion-doped $BiFeO_3$. Different research groups have reported different value of solubility limits of rare earth metal ions ranging from 0.1 to 0.2 with contradictory results of structural transformation from rhombohedral (R*3c*) to orthorhombic (Pnm*a* or Pn2_1*a*) and tetragonal (Pmn*a*). Moreover, the reported phase transition relations of the system are not consistent with each other.

This thesis discusses the synthesis and characterization of pure and rare earth metal (Gd^{3+}, Tb^{3+}, Dy^{3+})-doped $BiFeO_3$ nanostructures viz., nanoparticles and nanowires. The effect of doping and reduced nano-size on their structural, magnetic, electric and multiferroics properties, presented.

1.4.1. Objectives of the thesis

- The synthesis of rare earth metal (Gd, Tb, Dy) doped $BiFeO_3$ nanostructures, viz., nanoparticles, nanowires by chemical synthesis route.
- The effect of doping on multiferroic properties viz. ferroelectric, magnetic and dielectric of synthesized nanostructures will be explored.

- The characterization of synthesized $BiFeO_3$ nanostructures; structurally by X-ray diffraction (XRD), morphologically by Scanning Electron Microscopy (SEM), Transmission Electron Microscopy (TEM).
- The electrical, dielectric studies using respectively by Polarization versus Electric field (PE) loop tracer, LCR meter.

1.5. Materials and nanostructures under present study

The following nanostructures of multiferroics have been synthesised for the investigation:

Group I: Nanoparticles of rare earth metals-doped $BiFeO_3$

a. $Bi_{1-x}Gd_xFeO_3$ where x = 0, 0.02, 0.04, 0.06, 0.08, 0.10, 0.12 and 0.15

b. $Bi_{1-x}Dy_xFeO_3$ where x = 0 and 0.15

c. $Bi_{1-x}Tb_xFeO_3$ where x = 0 and 0.15

Group II: Nanowires of rare earth metals-doped $BiFeO_3$

a. $Bi_{1-x}Gd_xFeO_3$ where x = 0 and 0.15

b. $Bi_{1-x}Dy_xFeO_3$ where x = 0 and 0.15

c. $Bi_{1-x}Tb_xFeO_3$ where x = 0. 0.05, 0.10 and 0.15

1.6. Organization of the thesis

The present thesis is divided into five chapters:

Chapter 1 deals with introductory aspects and literature survey on multiferroic materials with specific mention of $BiFeO_3$ their structure, multiferroic properties and applications.

Chapter 2 deals with the techniques used for the synthesis and characterization of pure and rare earth metal (RE), viz., Gd, Tb, Dy-doped $BiFeO_3$ ($Bi_{1-x}RE_xFeO_3$) nanostructures.

Chapter 3 deals with the study of multiferroic properties of pure and rare earth metal ions (Gd^{3+}, Tb^{3+}, Dy^{3+})-doped $BiFeO_3$ nanoparticles synthesized by the sol-gel method. The effect of rare earth metal ion doping as well as the nanosize of the as-synthesized nanoparticles multiferroic

properties has been investigated.A part of this chapter has been published in the form of following research papers:

1. *Gurmeet Singh Lotey*, NK Verma, Structural, magnetic, and electrical properties of Gd-doped $BiFeO_3$ nanoparticles with reduced particle size, Journal of Nanoparticles Research, 14 (2012) 742 (Springer).
2. *Gurmeet Singh Lotey*, N.K. Verma, Magnetodielectric properties of rare earth metal-doped $BiFeO_3$ nanoparticles, Journal of Materials Science: Materials in Electronics, 24 (10) (2013) 3723-3729 (Springer).
3. *Gurmeet Singh Lotey*, N.K. Verma, Magnetoelectric coupling in multiferroic Tb-doped $BiFeO_3$ nanoparticles, Materials Letter, 111 (2013) 55-58 (Elsevier).
4. G Dhir, *Gurmeet Singh Lotey*, P. Uniyal, N.K.Verma, Size-dependent magnetic and dielectric properties of Tb-doped $BiFeO_3$ nanoparticles, Journal of Materials Science: Materials in Electronics, (2013), 24:4386-4392 (Springer).
5. *Gurmeet Singh Lotey,* N K Verma, Structural, electrical, magnetic and multiferroism in Dy-doped $BiFeO_3$ nanoparticles, AIP Conference Proceeding 1536 (2013) 55-56 (American Institute of Physics).

Chapter 4 deals with the study of magnetoelectric coupling in pure and rare earth metal ions (Gd^{3+}, Tb^{3+}, Dy^{3+})-doped $BiFeO_3$ nanowires synthesized by colloidal dispersion template-assisted technique. The effects of doping of rare earth metal ions as well as the nanosize of the synthesized nanowires on multiferroic properties have been investigated. For the comparative study, nanowires of size, 100 nm (bulk in present case) and 20 nm, have been synthesized. A part of this chapter has been published in the form of following research papers:

1. *Gurmeet Singh Lotey*, NK Verma, Magnetoelectric coupling in multiferroic $BiFeO_3$ nanowires, Chemical Physics Letters,579 (2013) 78-84(Elsevier).
2. *Gurmeet Singh Lotey*, NK Verma, Phase-dependent multiferroism in Dy-doped $BiFeO_3$ nanowires, Superlattices and Microstructures, 53 (2013) 184–194 (Elsevier).
3. *Gurmeet Singh Lotey***,** NK Verma, Multiferroic properties of Tb-doped $BiFeO_3$ nanowires, Journal of Nanoparticles Research,15 (2013)1553 (Springer).
4. *Gurmeet Singh Lotey***,** NK Verma Multiferrosim in rare earth metals-doped $BiFeO_3$ nanowires, Superlattices and Microstructures,60 (2013)60-66 (Elsevier).

Finally, **Chapter 5** gives the conclusions and suggestions for future research.

Chapter 2

Synthesis and experimental techniques

Overview

The performance of nanomaterials depends upon their atomic structure, arrangement of atoms in crystal structure, morphotropic phase, purity, defects, crystallinity, homogeneity of size and morphology. These parameters can be controlled by the thermodynamics and kinetics of the synthesis technique. Pure and rare earth metal (RE), viz., Gd, Tb, Dy-doped $BiFeO_3$ *(*$Bi_{1-x}RE_xFeO_3$*) nanostructures, viz., nanoparticles and nanowires with x = 0 to 0.15 have been synthesized by sol-gel method and colloidal-dispersion capillary force-induced filling of anodic alumina oxide (AAO) templates techniques, respectively.*

Characterizations of synthesised nanostructures are required to probe or analyse their crystallographic structure, morphology, electric, dielectric and magnetic properties. Synthesized nanostructures of pure and RE-doped $BiFeO_3$ *have been characterized by their crystallographic structure, elemental and compositional, morphological, electrical, magnetic and magnetoelectric coupling properties. The techniques used include x-ray diffraction (XRD), scanning electron microscopy (SEM), transmission electron microscopy (TEM), high-resolution TEM (HRTEM) microscopy, x-ray photoelectron spectroscopy (XPS), superconducting quantum interface device (SQUID), polarization versus applied electric field (P–E) hysteresis loops, leakage current density versus applied electric field (J-E) characteristics, dielectric, magnetoelectric coupling coefficient (MD) and magnetoelectric coupling (ME) coefficient measurements.*

2.1 Synthesis of $BiFeO_3$ nanostructures

2.1.1 Materials

All the chemicals, Bismuth(III) nitrate pentahydrate ($Bi(NO_3)_3 \cdot 5H_2O$), Iron(III) nitrate nonahydrate ($Fe(NO_3)_3 \cdot 9H_2O$), Gadolinium(III) nitrate hexahydrate ($Gd(NO_3)_3 \cdot 6H_2O$), Terbium(III) nitrate pentahydrate ($Tb(NO_3)_3 \cdot 5H_2O$), Dysprosium(III) nitrate hydrate ($Dy(NO_3)_3 \cdot xH_2O$), Tartaric acid ($HO_2CCH(OH)CH(OH)CO_2H$), Ethylene glycol ($HOCH_2CH_2OH$), 2-methoxyethanol ($CH_3OCH_2CH_2OH$) of analytical grade were procured from Sigma Aldrich and used without further purification.

2.1.2 Synthesis of $BiFeO_3$ nanoparticles by sol-gel method

Pure and rare earth metal (RE), viz., Gd, Tb, Dy, doped $BiFeO_3$ ($Bi_{1-x}RE_xFeO_3$) nanoparticles with x = 0 to 0.15 have been synthesized by sol-gel method [3, 59-62]. It is wet chemical route.

2.1.3 Methodology

For the synthesis of pure and rare earth metal (RE), viz., Gd, Tb, Dy, doped $BiFeO_3$ ($Bi_{1-x}RE_xFeO_3$) nanoparticles, the analytical grade bismuth (III) nitrate pentahydrate ($Bi(NO_3)_3 \cdot 5H_2O$) and iron (III) nitrate nonahydrate ($Fe(NO_3)_3 \cdot 9H_2O$) in the stoichiometric ratio are used to prepare precursor solutions by dissolving them in ethylene glycol [3, 59-62]. The above solutions are mixed. Tartaric acid is used as chelating agent. Tartaric acid in 1:1 molar ratio with respect to precursors is added to the solution. The resultant solution is transparent, brownish, and clear. The mixture is stirred for several hours at 60^oC to obtain gel. The low temperature heating treatment is given to obtain uniform, homogenous and smaller size nanoparticles. The as-obtained samples are subsequently washed with distilled water with an application of sonication, later collected by centrifugation, dried and grounded followed by calcination at 400^oC for 4 hours. The low calcination temperature is employed to minimize the risk of volatilization of bismuth.

The series of samples of rare earth metal (RE) viz., Gd, Tb, Dy, doped $BiFeO_3$ nanoparticles ($Bi_{1-x}RE_xFeO_3$) are prepared by adopting same procedure as mentioned above using Gadolinium(III) nitrate hexahydrate ($Gd(NO_3)_3 \cdot 6H_2O$), Terbium(III) nitrate pentahydrate ($Tb(NO_3)_3 \cdot 5H_2O$), Dysprosium(III) nitrate hydrate ($Dy(NO_3)_3 \cdot xH_2O$) [3, 59-62]. The detailed scheme of sol-gel synthesis of RE-doped $BiFeO_3$ nanoparticles is given in Figure 2.1.

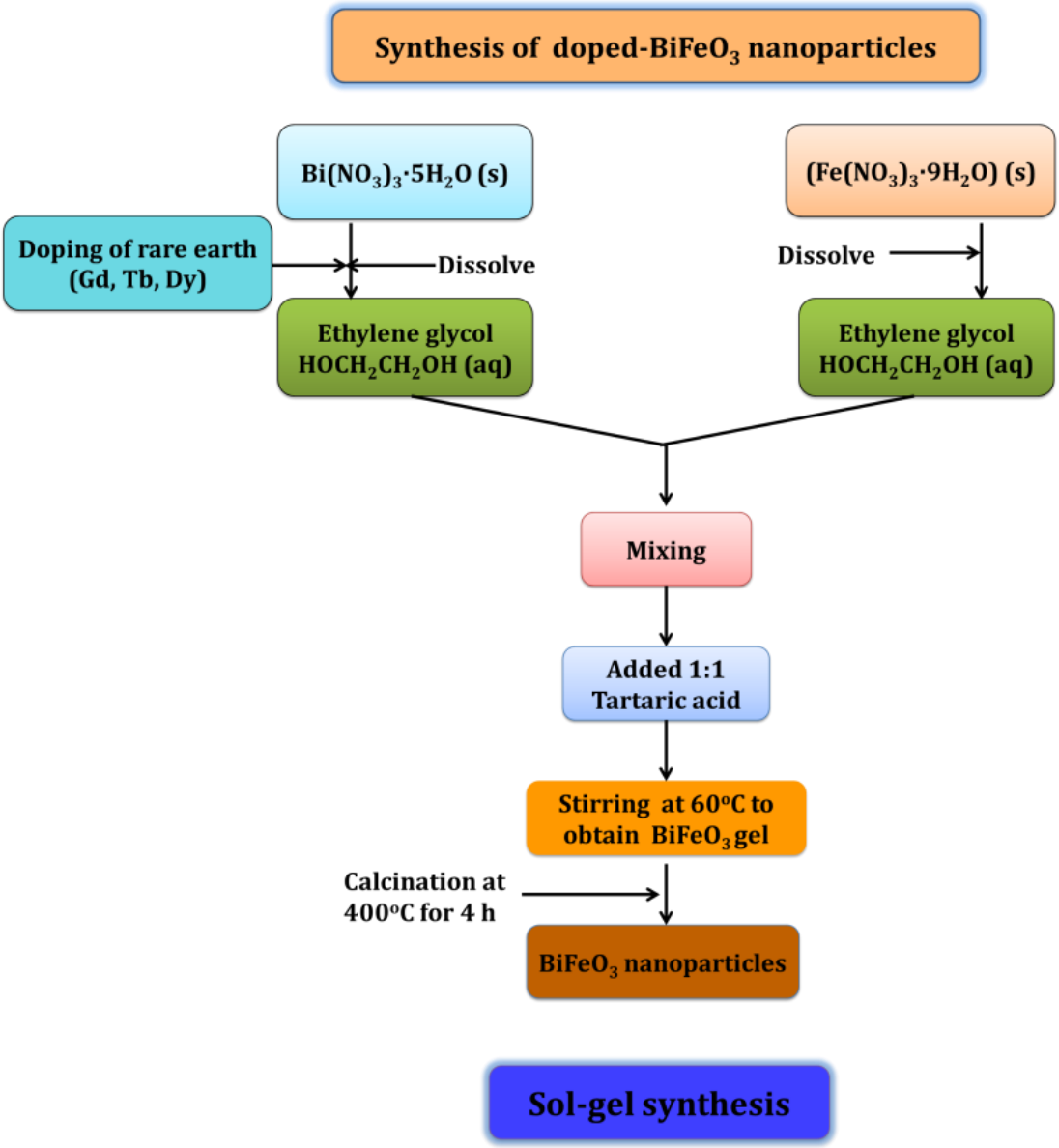

Figure 2.1 Scheme of sol-gel synthesis of RE-doped $BiFeO_3$ nanoparticles

2.1.4 Growth mechanism of $BiFeO_3$ nanoparticles

Figure 2.2 shows the schematic of formation of $BiFeO_3$ nanoparticles by sol-gel method. The precursor solutions of bismuth (III) nitrate pentahydrate (Bi $(NO_3)_3 \cdot 5H_2O$) and iron (III) nitrate nonahydrate (Fe $(NO_3)_3 \cdot 9H_2O$) have been prepared by dissolving these in the stoichiometric ratio in ethylene glycol. Tartaric acid was used as chelating agent. After the reaction proceeds, the precursor solutions form complex of Bi and Fe with chelating agent [62]. The chelating complex

is subsequently heated and this leads to the formation of colloidal suspension of $BiFeO_3$, i.e., solid particulates in a liquid called sol. This dual phase material composed of solvent skeleton filled with solvent called wet-gel through sol-gel transition, i.e., gelation. Finally, the decomposition of sol leads to the formation of $BiFeO_3$ nanoparticles. *Tartaric acid has been found to be the best chelating agent for the synthesis of $BiFeO_3$ nanoparticles and it helps to control their shape, morphotropic phase, size and crystallinity*.

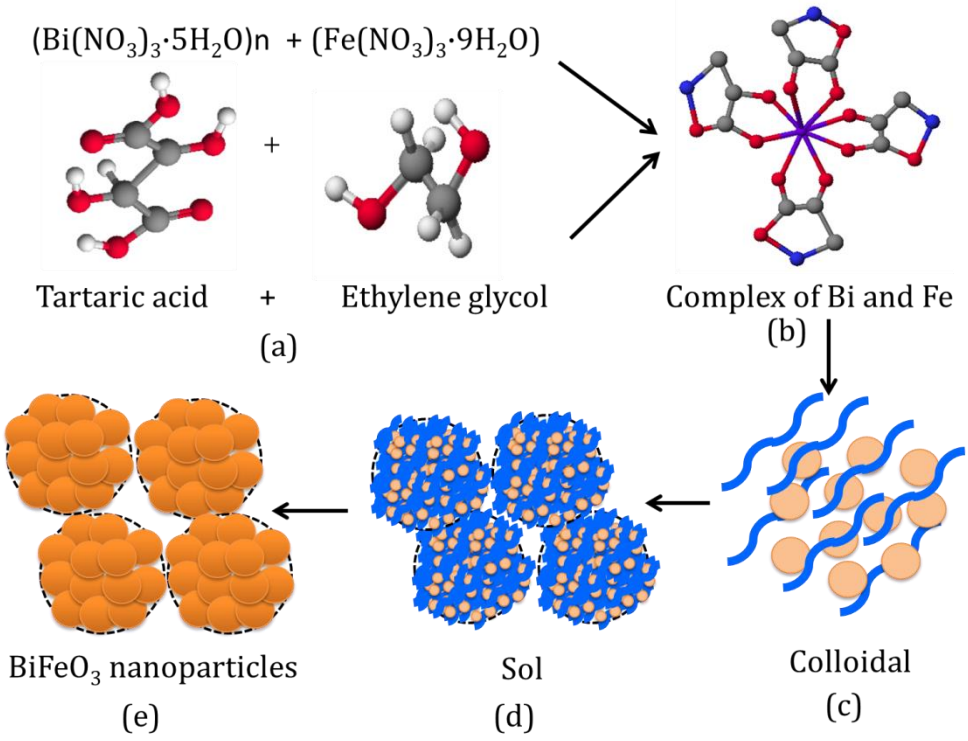

Figure 2.2 Schematic for the formation $BiFeO_3$ nanoparticles by sol-gel method. This involves (a) reaction between precursor (b) formation of complex (purple for Bi, blue for Fe, grey for C) (c) colloidal (d) sol and (e) $BiFeO_3$ nanoparticles

2.1.5 Synthesis of $BiFeO_3$ nanowires by colloidal-dispersion capillary force-induced filling templates technique

Pure and rare earth metals viz., Gd, Tb, Dy (RE)-doped $BiFeO_3$ nanowires have been grown in anodic alumina oxide (AAO) templates by colloidal dispersion capillary force-induced filling of nanochannels of AAO template [63-66]. Colloidal-dispersions are prepared using appropriate

sol-gel processing [3, 59-66]. It is kinetically controlled reaction and may proceed through homogeneous nucleation or by reaction on seeds.

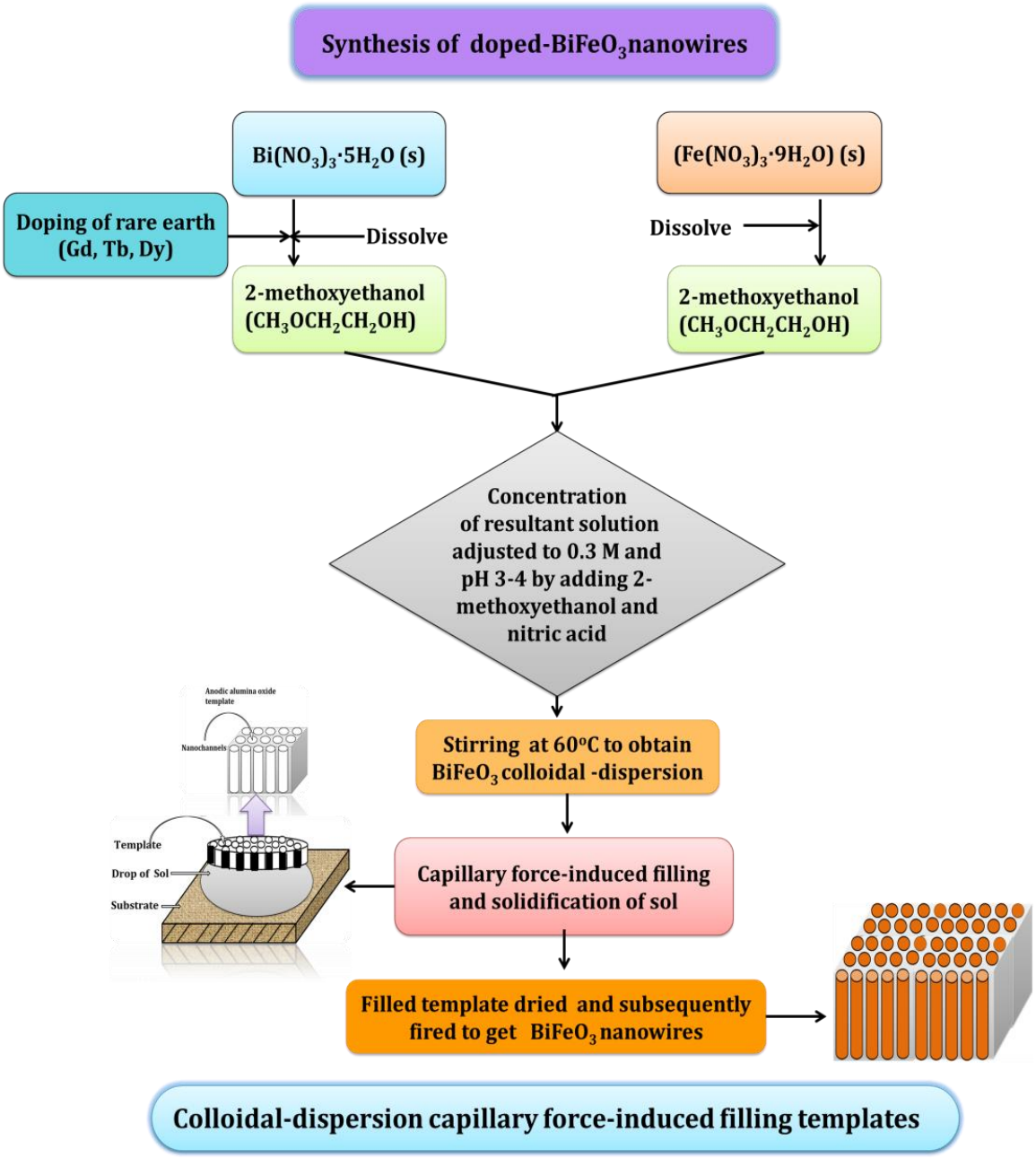

Figure 2.3 Scheme of Colloidal-dispersion capillary force-induced filling templates synthesis of RE-doped $BiFeO_3$ nanowires

In the colloidal-dispersion capillary force-induced filling of templates, to drive the colloidal-dispersion (sol) into the nanochannels of template, surface chemistry of the template pores

modified to have a good wettability for the sol. After the filling of pores with sol, the template is withdrawn from the sol and dried, and, subsequently firing at elevated temperatures, to remove template and densification of nanowires.The possible mechanism could be the diffusion of solvent through the membrane, leading to the enrichment of solid along the internal surface of template pores, a process used in ceramic slip casting.

2.1.6 Methodology

Colloidal dispersion capillary force-induced filling of nanochannels of AAO template involve the synthesis of colloidal dispersions [63-66]. In typical synthesis of colloidal dispersions, appropriate amounts of $Bi(NO_3)_2.5H_2O$ and $Fe(NO_3)_3.9H_2O$ are dissolved in 2-methoxyethanol. The concentration of resultant solution is adjusted to 0.3 M and the pH to around 3-4 by adding 2-methoxyethanol and nitric acid, respectively. The resultant solution is transparent, brownish, and clear. The mixture is stirred for 4 hours at 60^oC to obtain sol. The commercially available AAO templates (Anodisc 25, Whatman, UK) of average pore diameter - 20 and 100 nm have been used. The schematic of synthesis process is shown in Figure 2.3. An excess amount of synthesized sol was dropped onto Indium tin oxide coated glass (ITO) substrate, and subsequently AAO template is placed on top of the solution at ambient conditions of temperature and pressure for 5 h to allow complete filling and solidification of sol [63-66] (Figure 2.3 and Figure 2.4). The filled template on ITO substrate is dried under vacuum at 80^oC for 12 h. Subsequently templates are fired at 600^oC for 1 h to get $BiFeO_3$ nanowires. RE-doped $BiFeO_3$ nanowires ($Bi_{1-x}RE_xFeO_3$) with x = 0 to 0.15 are prepared by adopting same procedure as mentioned above. For a comparative study bulk nanowires having 100 nm diameter nanowires have been synthesized by adopting same procedure [65].

2.1.7 Growth mechanism of $BiFeO_3$ nanowires

Bulk nanowires (having diameter 100 nm), pure and RE-doped $BiFeO_3$ nanowires are grown in AAO template by colloidal dispersion capillary force-induced filling of nanochannels of template - a simple nucleation and growth process [63-66]. The capillary force is believed to drive the sol into the pores of templates. Subsequently, the heating of templates filled with sol for 1h leads to the formation of $BiFeO_3$ nanowires in AAO matrix. Filling of AAO template by colloidal dispersion is kinetically spatially confined, and, the growth is effectively controlled,

which stops when the limited amount of the source materials (sol/colloidal dispersion) is either consumed or the available space is filled[67]. Depending upon the adhesion between the pore walls of template and the filling material, nucleation may start at the center, or from one end of the pore, or uniformly. Figure 2.4 shows the schematic of different steps involved in the capillary force-induced filling of templates [63, 65]. Sol consists of nanosized-particulatesdispersed in a solution [63a, 65].

These nano-particulates induce surface charges and form a double layer as the surface of AAO template is just brought into contact with a sol. As reported earlier by Takahashi et al. [63], if the surface charge or zeta potentials of the nano particulates in the sol and the surface of nanochannels of template are similar, the nanorods will be formed [63, 65]. In our case, the zeta potential of $BiFeO_3$ sol and the nanochannels pores' surface are found to be of same sign, i.e., both of them have positive charges of 5mV and 18.5 mV, respectively. However, in the present study, instead the nanowires have been formed [65].

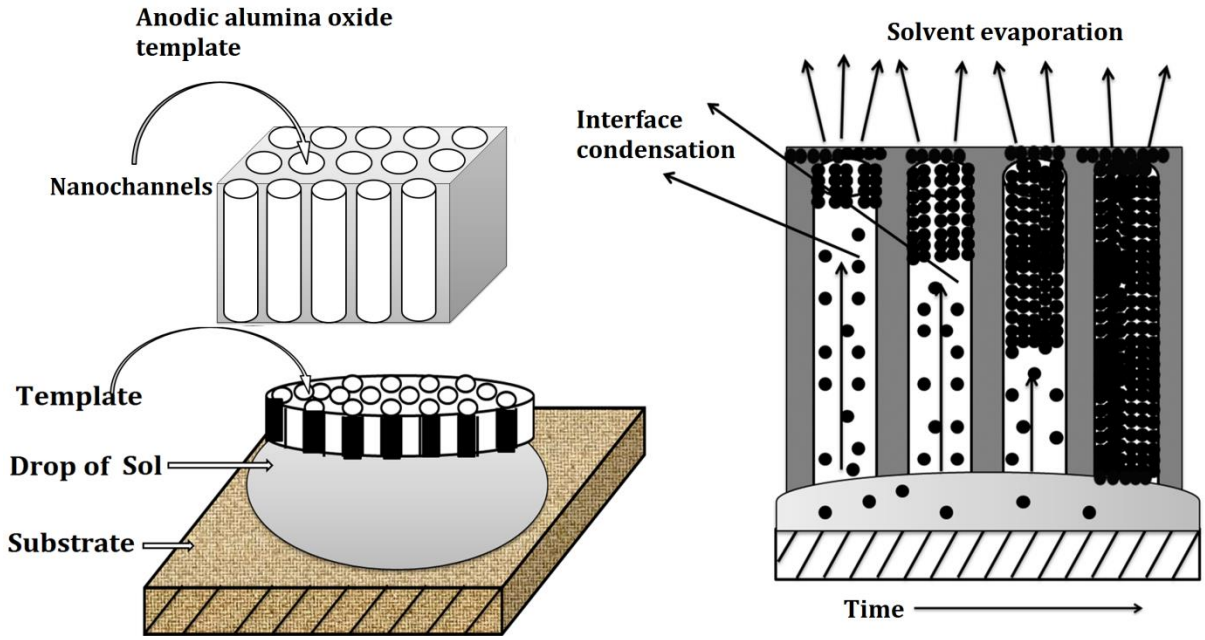

Figure 2.4 Schematic of mechanism of formation of $BiFeO_3$ nanowires in nanochannels of the AAO templates and the different steps involved in the capillary force-induced filling of the templates

2.2 Characterization Techniques

2.2.1Crystallographic and structural characterization by x-ray diffraction

The crystallographic structural analyses, phase identification, phase purity in the synthesized nanostructures have been carried out using x-ray diffractometer of PANalyticalX'PertPRO MPD with Cu-Kα (λ = 1.54060Å) radiation operated at 45 kV and 40 mA. The high intense beam was focused over a small area (~ 10 mm^2) of the sample, and gonio scan has been recorded for 2θ value from 20^o to 90^o[3].

XRD works on the principle of Bragg's law. This technique used to study crystallographic parameters of materials. The crystal is bombarded with x-rays at certain incident angles and the intense reflected x-rays are produced on constructive interference of the scattered x-rays (Figure 2.5). In order for the waves to interfere constructively, the difference in the travel path must be an integral multiple of the incident wavelength and the diffracted beam of x-rays leaves the crystal at an angle equal to that of the incident [68-70].

$$2d \sin\theta = n\lambda$$

where 'λ' is the wavelength of the x-rays, '*d*' inter-planar spacing between planes, θ is the angle of glancing (Bragg's angle) that the x-ray beam makes with the plane of atoms (*hkl*) and 'n' is the order of diffraction. Figure 2.5 shows the geometry of basic components of XRD.

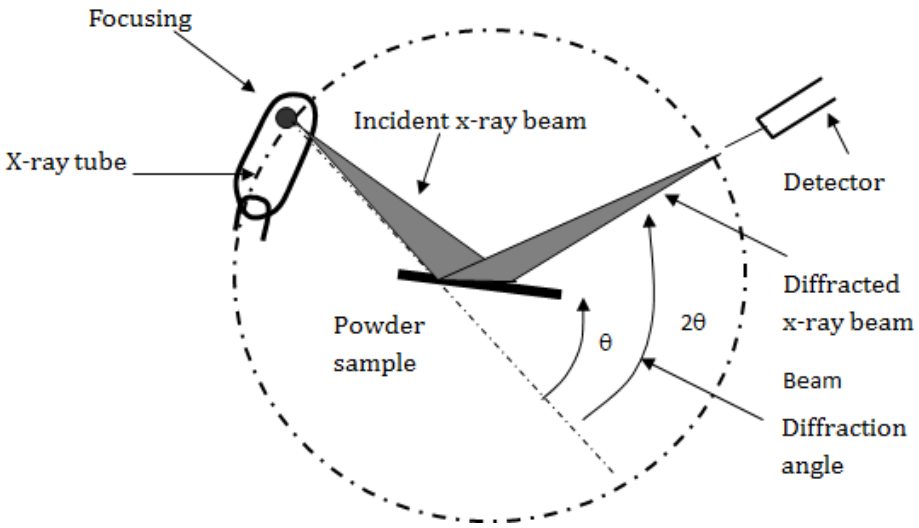

Figure 2.5 Geometry of x-ray diffractometer

In powder XRD method the particles of the powder,acts as tiny crystal oriented at random order with respect to the incident x-ray beam [3]. Therefore, each set of planes will be capable of reflection. The net effect will be equivalent to as if a single crystal is rotated about all possible axes. The shape of the XRD patterns gave information regarding the grain size, strain, structural deformation.

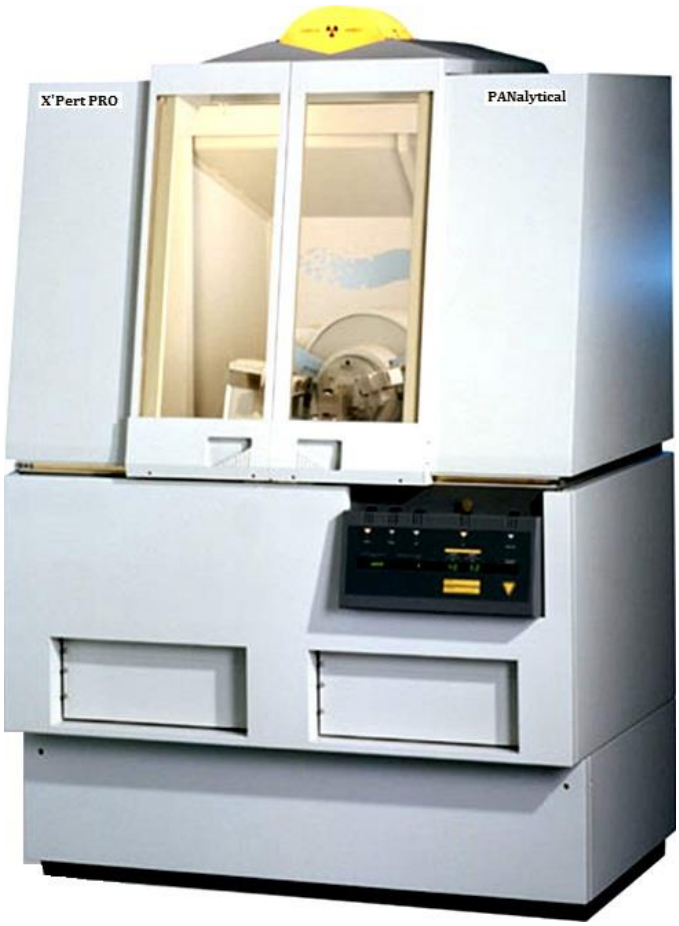

Figure 2.6 Photograph of x-ray diffractometer by PANalytical X'Pert PRO MPD

It has been found that XRD patterns of nanostructural materials get broaden due to availability of the number of parallel planes for diffraction is very small [69-70]. Figure 2.6 shows the photograph of XRD used for the present study. It is composed of an x-ray source, sample stage and x-ray detector like a proportional or scintillation counter to measure the positions of the diffracted beams.

Determination of crystallite size and lattice strain: The crystallite size and lattice strain can be calculated by careful analysis of peak's shape and position. The crystallite size (D) and the

lattice strain (ε) have been calculated from the full-width at half maximum (FWHM), β, of a diffraction peak using Williamson-Hall formula [69-70]:

$$\frac{\beta\, cos\theta}{\lambda} = \frac{1}{D} + \frac{\varepsilon\, sin\theta}{\lambda}$$

where λ stands for the x-ray wavelength, θ - the diffraction angle. To eliminate the additional broadening from the instrument, the observed FWHM has been corrected, using the FWHM from a large-grain Si standard sample:

$$\beta_{corrected} = (FWHM^2_{sample} - FWHM^2_{Si})^{1/2}$$

The Williamson-Hall plot has been drawn between sinθ/λ and βcosθ/λ. The slope and intercepts of plot gives respectively, strain (ε) and crystallite size (D) of the synthesized samples [69-70].

2.2.2 Chemical composition and oxidation state by x-ray photoelectron spectroscopy

X-ray photoelectron spectroscopy (XPS) has been carried out to know the chemical bondingand oxidation states of Bi, Fe, O, and rare earth metal (Gd, Tb, Dy) to corroborate theformation of $BiFeO_3$ using VG Microtech MultiLab ESCA 3000 System[3].

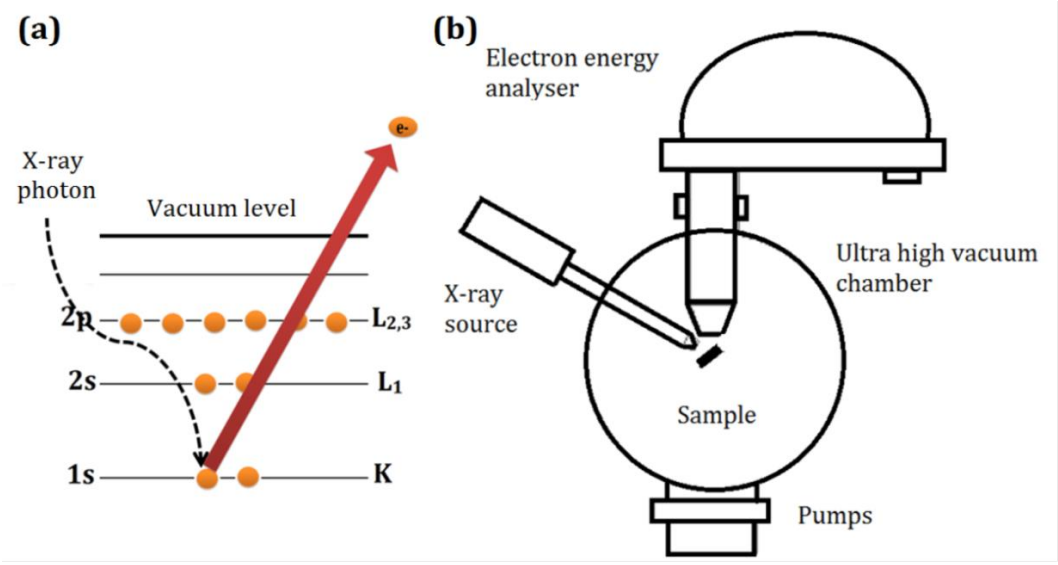

Figure 2.7 Schematic of (a) working principle of XPS and (b) experimental set-up

Figure 2.7 shows the basic experimental set-up and basic working principle of XPS. The

specimen is irradiated with x-rays such that an atom gains energy amount equal to *hv* as explained in Figure 2.7 (a). It then releases an electron to regain its original stable energy state. The released electron retains all the energy from the striking photon, and escape from the atom, and even further from matter and kinetic energy keeps it moving. The principle of conservation of energy allows the energy balance equation, valid for the absorption of a photon carrying energy of *hv* to be written as:

$$h\nu = E_{kinetics} + E_{binding}$$

XPS is used quantitatively analyse the elemental composition, chemical and electronic state of the elements. XPS spectrum has been measured by irradiatingthe requisite sample with x-rays. The kinetic energy and number of electrons has been measured[71-72].

2.2.3 Morphological study by scanning electron microscopy and transmission electron microscopy

2.2.3.1 Scanning electron microscopy

The morphological study of synthesized nanostructures viz., nanoparticles and nanowires has been performed using scanning electron microscopy (SEM). The dried samples are mounted using a double adhesive carbon tape on an especially designed aluminum stub, subsequently, coated with a layer of gold–palladium alloy using (JEOL, FINE SPUTTER JFC-1100) sputter coating unit and viewed under SEM (JEOL, JSM-6510LV) at 25 kV accelerating voltage [3].

A high-energy focused beam of electrons is bombarded on samples to analyseits topography, morphology and chemical composition [73]. Figure 2.8 shows the possible signals include secondary electrons, back-scattered electrons, characteristic x-rays, light (cathode-luminescence), specimen current and transmitted electrons produced by an electron beam incident on the specimen. SEM can achieve resolution better than 1 nanometer[73]. The signals from the secondary and backscattered electrons are used for study morphology, topography and composition of samples.Figure 2.9 shows photograph of SEM of JOEL JSM-6510LV used for present study. SEM analysis required high vacuum inside; therefore the samples need to be dry. The semiconducting or insulating samples must be coated with a thin film of usually gold or gold–palladium alloy and sometimes carbon, to conduct electricity [73].

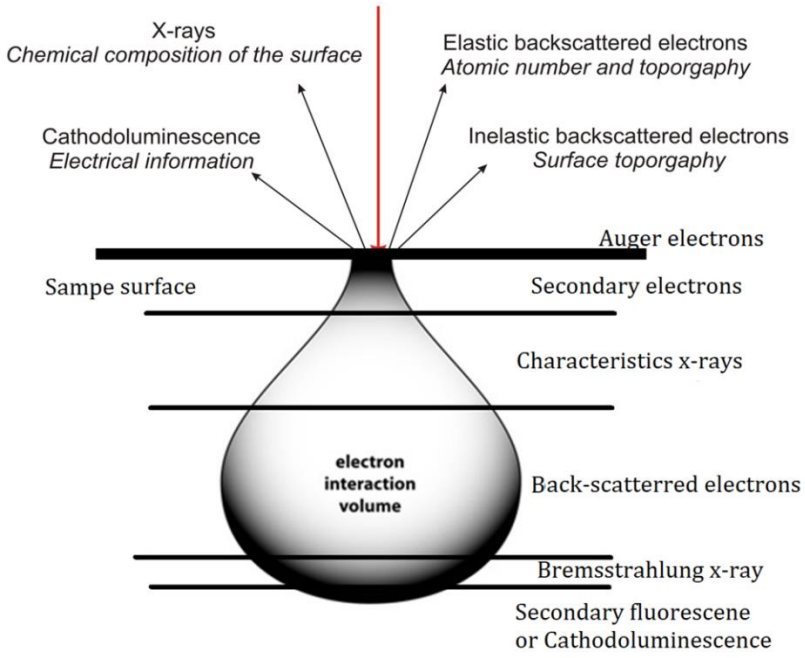

Figure 2.8 Illustration of the signals produced by an electron beam incident on the specimen

Figure 2.9 Photograph of SEM of JOEL JSM-6510LV

2.2.3.2 Transmission electron microscopy

Transmission electron microscopy technique used to gain information regarding size, morphology and phase identification at the nano-scale, defect analysis (such as dislocations, stacking faults), chemical composition (energy dispersive spectroscopy of x-rays,), high resolution images (~0.2 nm resolution). Transmission electron microscopy (TEM) images have taken on a Hitachi-H7650 transmission electron microscope with an accelerating voltage of 300 kV [3].

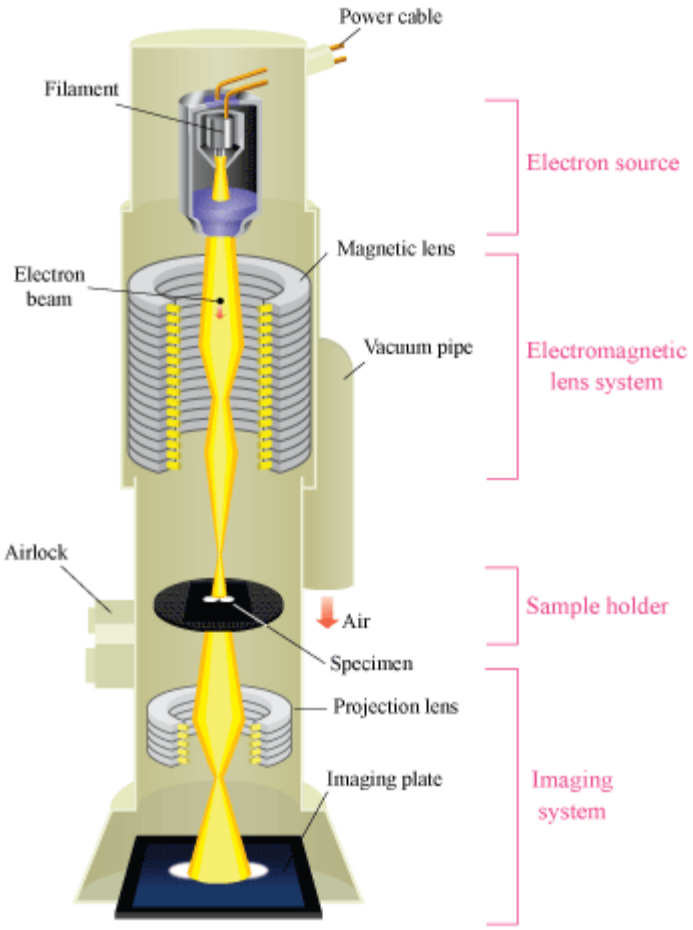

Figure 2.10 Schematic of experimental set-up and working principle of TEM

In TEM microscopy, a beam of highly focused electrons is allows to transmit through an ultra-thin specimen. The interactions of the transmitted electrons used to form image [74].TEM

mainly consist of electron source (gun), electromagnetic lenses, sample holder stage and imaging system as shown in Figure 2.10. The intermediate lens focuses the electron beam on the image plane of the projector lens. All the transmitted and diffracted rays leaving the specimen are combined to form an image at the viewing screen. An image can be formed with those rays passing through one point in the back focal plane [74].Figure 2.11 shows the photograph of Hitachi-H7650 transmission electron microscope used for present study. For TEM measurements, the synthesized sample is dispersed in a solvent using ultra-sonication. A drop of above solution is dropped on a carbon-coated copper grid. The grid is dried with the help of a filter paper under an infrared lamp, and specimen is ready for TEM imaging [74].

Figure 2.11 Photograph of Hitachi-H7650 transmission electron microscope

2.2.4 Magnetic analysis by superconducting quantum interference device magnetometer

The magnetic analysishave been carried out using Magnetic Property Measurement System (MPMS XL) of Quantum Design, superconducting quantum interference device (SQUID).

Superconducting quantum interference device (SQUIDs) is very sensitive magnetometer and can detect small changes in the magnetic field, up to 10^{-15}T. It is the only device which allows to determining the overall magnetic moment of a sample in absolute units. SQUID works on three fundamental characteristics of superconductors, viz., flux quantization, electron-pair wave coherence and the DC Josephson effect as shown in Figure 2.12 (a).

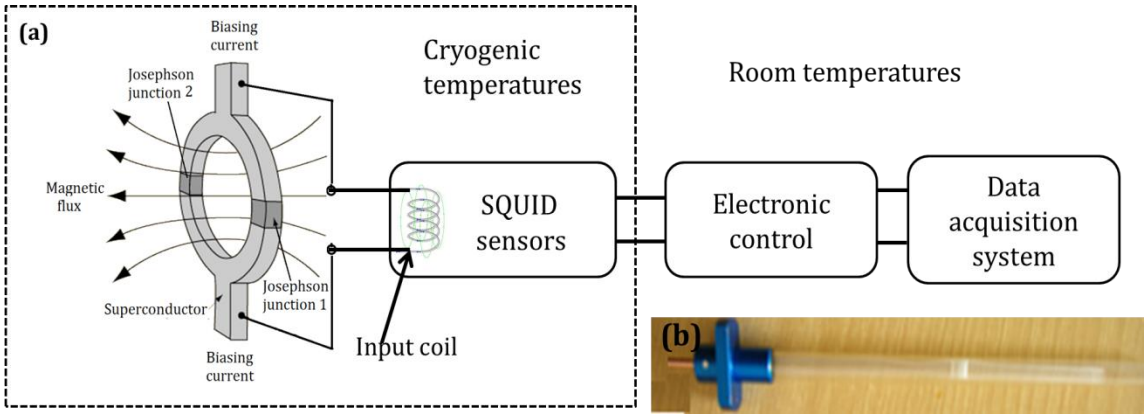

Figure 2.12 (a) Block diagram of SQUID magnetometer and (b) sample holder

Figure 2.13 Photograph of SQUID magnetometer, MPMS XL7 of Quantum design

Figure 2.12 (b) shows the plastic straw used as sample holder for SQUID measurement. It is a diamagnetic sample holder, and moved up and down inside a superconducting coil. Such a movement induces some electric current, which can be detected and measured. The amplitude of the current allows estimating the absolute value of the magnetization of the specimen. Therefore, SQUID magnetometers are versatile instruments that perform both, DC and AC magnetic moment measurement [75]. SQUID Magnetometer is used for magnetic measurements of the synthesized samples [75]. Figure 2.13 shows the photograph of SQUID magnetometer, MPMS XL7 of Quantum design used for the present study.

2.2.5 Ferroelectric analysis by polarizationversus ion of electric field (P–E) hysteresis

The ferroelectric hysteresis loops (P-E) and leakage current density versus applied electric field (J-E) of the synthesized nanostructures have been measured using a Precision Premier II Workstation (Radiant Technology, USA) under an applied electric field [3].

Ferroelectricmaterials exhibit spontaneous electric polarization in the absence of any externally applied field. These materials are consists of regions of uniform polarization called ferroelectric domains. In these regions the electric dipoles of the samples get aligned in the same direction [76]. Precision Premier II Workstation (Radiant Technology, USA as shown in Figure 2.14 (b)) have been be used to measure, polarization hysteresis, remnant hysteresis, leakage, leakage current versus applied DC field.

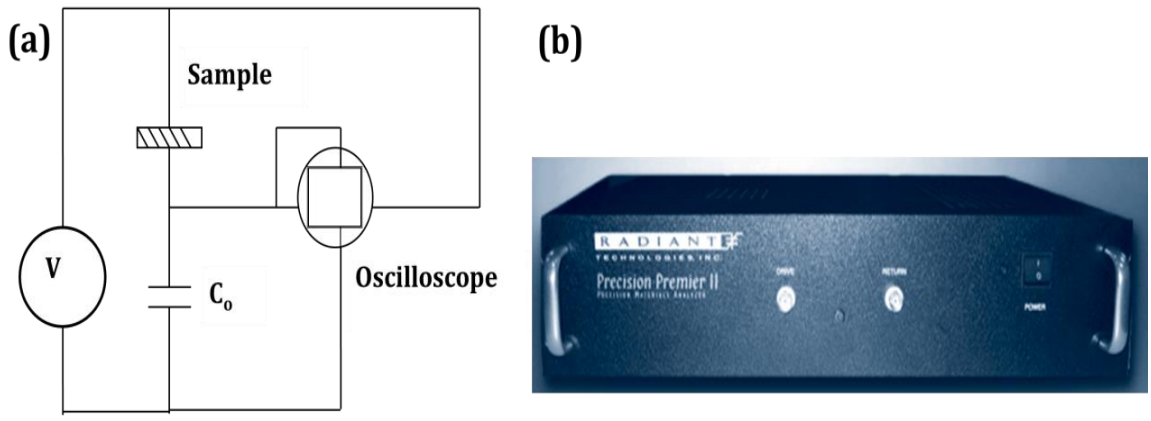

Figure 2.14 (a) Modified Sawyer-Tower Circuit and (b) photograph of Precision Premier II

For the ferroelectric measurements, a sinusoidal voltage is applied to the samples and the corresponding displacement is recorded. By plotting the displacement vs. driving voltage the hysteretic behavior of the samples can be observed. Experimentally, ferroelectric hysteresis loops can be measured using a Sawyer-Tower circuit or a modified version of it as shown in Figure 2.14 (a), by applying an a.c. field [76].

2.2.6 Dielectric measurements

The dielectric behavior, dielectric constant and dielectric losses in the synthesized nanostructures have been measured using an impedance analyzer (Agilent HP 4294A) as shown in Figure 2.15.

Dielectrics are insulator materials and can be polarized upon applied electric field. They do not carry free charge and are non-conductive i.e. these have very high resistivity, and, not allow flow of current ideally under the application of DC voltage conditions [77]. Under the application of direct current voltage, dielectric holds an electrostatic field and a slight movement of charges polarizes the material. Insulators are composed of electric dipole structure in which positively charged species are separated by negatively charged species on a molecular or atomic level as can be seen from Figure 2.15.

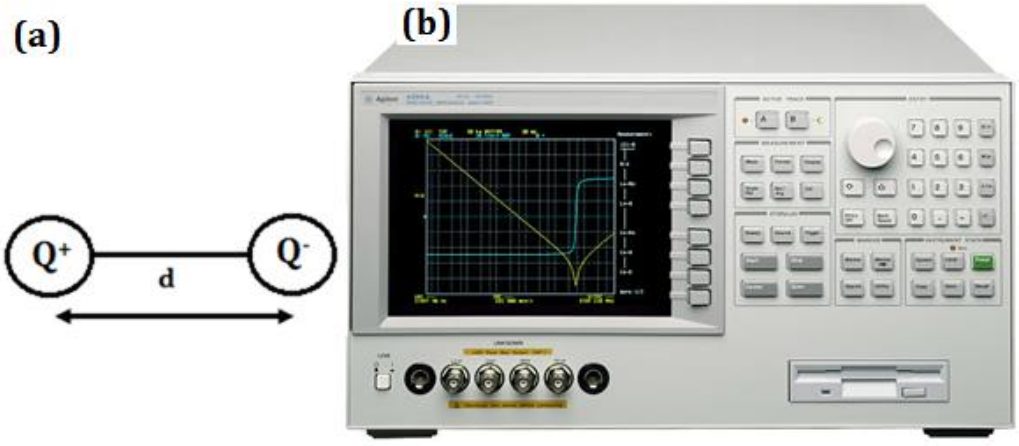

Figure 2.15 Schematic representation of (a) an electrical dipole generated by two equal and opposite charges of magnitude Q and separated by a distance d and (b) photograph of Agilent HP 4294A

Polarization of dielectrics is dipole ordering in space under external applied voltage, and, it is its intrinsic property (Figure 2.15 (a)). The induced dipole moment of individual particle is proportional to the intensity of the applied field, E.

$$P=\alpha E$$

where α is the polarizability of a given particle.

$$P=D-\varepsilon_0 E=(\varepsilon-\varepsilon_0)E$$

where $D = \varepsilon E$ is the dielectric displacement, ε is the permittivity of the material, and, ε_0 is the permittivity of free space [77].

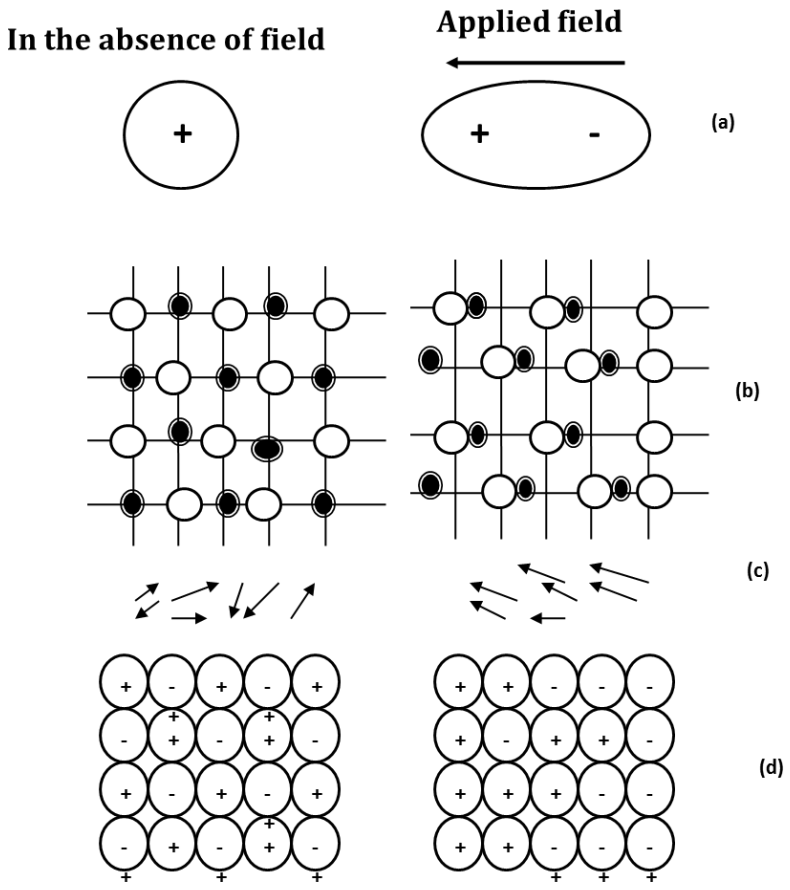

Figure2.16: Four sources of polarization (a) electronic (b) ionic (c) dipolar (d) space charge polarization

Four basic types of polarizations taking place in the dielectric materials are known as electronic, ionic, dipole and space charge polarization (Figure 2.16), and, the total polarization is given by general relation [64-66, 77]:

$$P_{total} = P_e + P_i + P_d + P_s$$

1. Electronic polarization (P_e) which arises due to the displacement of electrons with respect to the atomic nucleus under external field. Under such conditions the centre of gravity of the positive charges i.e. nucleus does not coincide with the electron charge distribution and equilibrium situation is attained in which atom bears a finite dipole moment.
2. Ionic polarization (P_i) originates from the mutual displacements of the ions forming molecules.
3. Orientational or dipolar polarization (P_o) found in materials with permanent dipole moment, induced by the rotation of these dipoles under dc field.
4. Space charge polarization (P_s) occurs in materials that are not perfect dielectrics but in which some long range charge migration may occur, e.g. NaCl[77].

2.2.7 Magnetoelectric coupling measurement

Magnetoelectric coupling can be measured directly or indirectly. The dynamic lock-in technique has been employed to measure the direct magnetoelectric coupling (ME) coefficients, and, the magnetic field-induced changes in the relative dielectric constant i.e., called magnetodielectric employed to measure magnetoelectric coupling indirectly [34, 79-82].

2.2.7.1. Magnetoelectric coupling measurements

Figure 2.17 shows the experimental set up used for ME measurement [79-82]. In this technique the DC magnetic bias field up to 20 kOe has been produced using electromagnetics I and measured with Hall probe (H_{DC}), while a time varying DC magnetic field is produced by DC power source (programmable DC power source of Siemens NTN 35000-200 has been employed)), and, is measured using Hall probe (H_{Ac}). AC magnetic bias field up to 20 Oe with frequency ranging from 1 to 1000 Hz has been produced using the amplified current signal from the internal function generator (F) of the lock-in amplifier (Stanford Research, model SR850) and, it is fed to the Helmholtz coils (H). The Gauss meter, G_{AC} and G_{DC} have also been employed to measure AC and DC magnetic field, respectively. The amplitude of AC field is measured using Keithley-2700 multimeter. Capacitive structures with gold (Au) electrodes (Au-$BiFeO_3$-Au) has been fabricated to measure the ME effect. To measure ME coupling coefficients, the synthesized samples (nanoparticles or nanowires) have been placed in between

the Helmholtz coils; these coils generate an AC magnetic field. A direct current (DC) bias magnetic field is superimposed on the AC magnetic field in parallel. The reorientation of the electrical dipoles in the $BiFeO_3$ by an AC magnetic field induces an AC voltage on the top and bottom surfaces of the sample through magnetoelectric coupling. The induced voltage has been measured using lock-in amplifier. To remove errors in signals due to Faraday induction, the lock-in amplifier is operated in the differential mode. The ME coupling coefficient, (α_{ME}), has been calculated using the following relation: [79-82]

$$\alpha_{ME} = \frac{\delta E}{\delta H} = \frac{V_{out}}{h_o t}$$

where, t is thickness of the sample, V_{out} is the AC magnetoelectric voltage appearing across the sample surface (as measured by the lock-in-amplifier), h_o is the amplitude of the AC magnetic field.

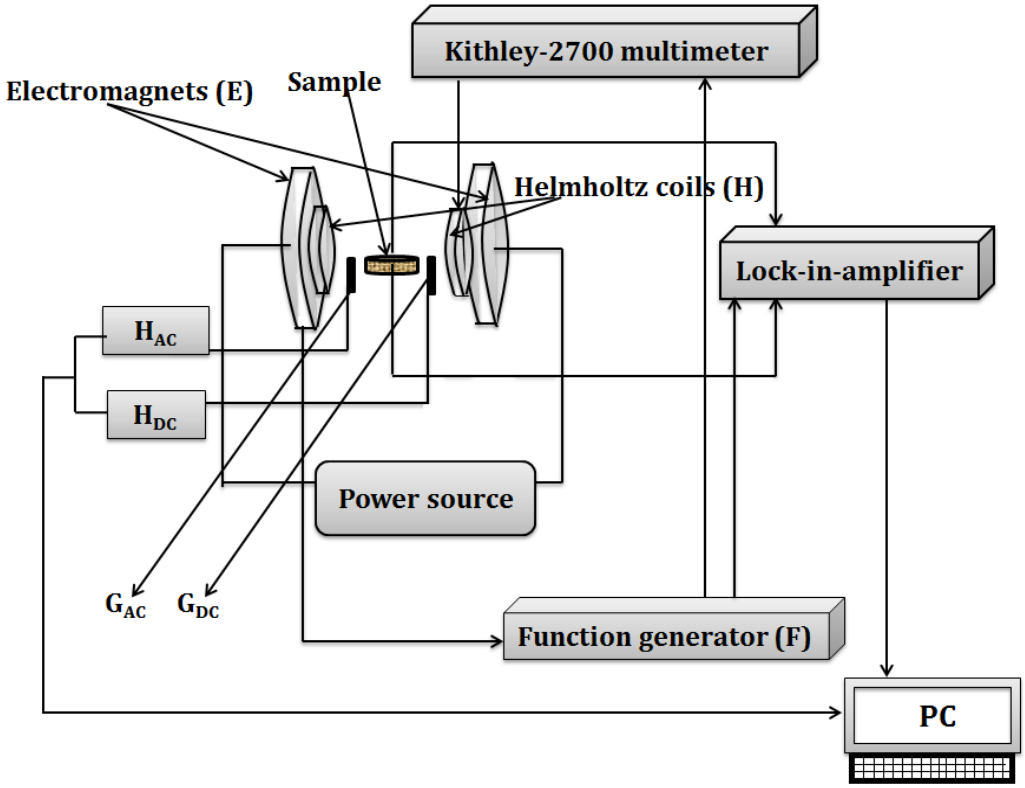

Figure 2.17 Schematic diagram of the dynamic lock-in technique for magnetoelectric coefficient measurements

The ME coupling coefficients have been measured in two modes viz., longitudinal (L-α_{ME}) and transverse (T-α_{ME}) with DC magnetic field parallel with and perpendicular to the direction of induced voltage, respectively. For longitudinal magnetoelectric coupling coefficient measuring mode, i.e., L-α_{ME}, the longitudinal magnetization of sample take place (direction of the applied field is along the sample surface) and the output voltage is measured in transverse direction, and, vice-versa is true for the T-α_{ME} mode. Data acquisition has been conducted by using a LABVIEW™ program.

2.2.7.2 Magnetodielectric measurements

Magnetoelectric coupling investigation can be carried out indirectly by measuring the change in dielectric constant in varying applied magnetic field. The change in dielectric constant has been measured as a function of applied magnetic field. Magnetodielectric coefficient (MD) is defined as [64, 65]

$$\mathrm{MD} = \frac{\Delta\varepsilon_r}{\varepsilon_r(0)} = \frac{\varepsilon_r(\mathrm{H}) - \varepsilon_r(0)}{\varepsilon_r(0)}$$

where$\varepsilon_r(\mathrm{H})$ and $\varepsilon_r(0)$ are the dielectric constants at applied and zero magnetic field, and $\Delta\varepsilon_r$ is the change in dielectric constant with and without magnetic field. MD give the idea regarding the magnetoelectric coupling present in samples.

2.2.8 Ferroelectric, leakage current density, dielectric and magneto-dielectric measurements of nanowires

For ferroelectric, leakage current density, dielectric and magneto-dielectric measurements of synthesized $BiFeO_3$ nanowires, special testing system has been designed, which is attached to the respective measuring instruments as shown in Figure 2.18. For these measurements, the surface of as grown $BiFeO_3$ nanowires embedded in AAO templates was first mechanically polished, and, then Au electrodes are deposited on both sides of the templates for electrical contacts. The measurement has been carried out using specific design instrument as shown in Figure 2.18. The synthesized $BiFeO_3$ nanowires embedded in AAO could be considered as a columnar composite film and their leakage current controlled by the $BiFeO_3$ due to the much higher resistance of AAO [28, 64-65, 78]. Therefore, the leakage current density of the $BiFeO_3$ nanowires within AAO composite remains nearly the same as the total leakage current of the entire

$BiFeO_3$nanowires within AAO composite. Likewise, the polarization, dielectric and magneto-dielectric $BiFeO_3$ nanowires would be the same as the total value of the $BiFeO_3$/AAO sample because of the non-polarization, non-dielectric and non-magneto-dielectric features of the AAO template. To obtain the corresponding intrinsic values, the polarization, leakage current density, dielectric and magneto-electric values were normalized to the area fraction (20%) of $BiFeO_3$ by considering that the contact area between the Cu electrodes and $BiFeO_3$ nanowires embedded in AAO [65, 77].

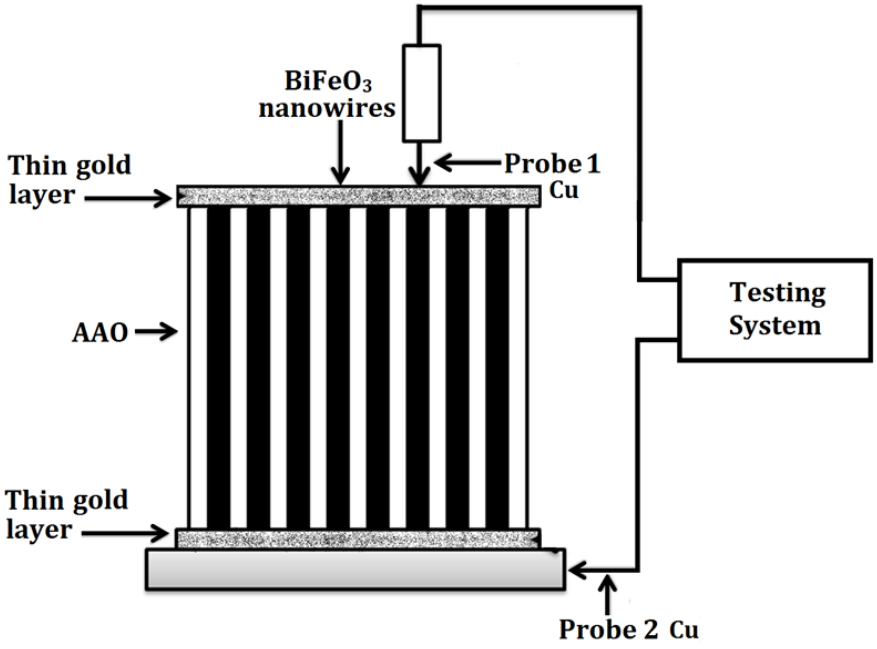

Figure 2.18 Schematic diagram of experimental set-up design to measure ferroelectric, dielectric and magnetodielectric properties of synthesized nanowires.

Chapter 3

Multiferroism in rare earth metal doped $BiFeO_3$ nanoparticles

Overview

This chapter deals with the study of multiferroic properties of rare earth metal ions (Gd^{3+}, Tb^{3+}, Dy^{3+}) doped $BiFeO_3$ nanoparticles synthesized by the sol-gel method. The effect of rare earth metal ion doping as well as the nanosize of the as-synthesized nanoparticles on morphology, structure, magnetic, electric, dielectric and magneto-dielectric/electric coupling properties have been investigated. Synthesized nanoparticles have been found to be possessing spherical morphology with average particle size lying between 15-50 nm. Structural study reveals that the doping of the rare earth metal ions in $BiFeO_3$ nanoparticles results in structural transformation from rhombohedral to orthorhombic phase. Magnetic study confirms that the synthesized nanoparticles exhibit well saturated hysteresis loops and possess ferromagnetic character. Dielectric measurements show that doping results in high dielectric constant as compared to that of pure $BiFeO_3$. To check the magnetoelectric coupling in the synthesized nanoparticles, magnetodielectric and magnetoelectric coefficient measurements have been done. The observed trend in the properties of the synthesized nanoparticles has been explained on the basis of doping of rare earth metal ions, structural transformation as well as the size of the synthesized nanoparticles.

A part of this chapter has been published in the form of following research papers:

1. *Gurmeet Singh Lotey, NK Verma, Structural, magnetic, and electrical properties of Gd-doped $BiFeO_3$ nanoparticles with reduced particle size, Journal of Nanoparticles Research, 14 (2012) 742 (Springer).*
2. *Gurmeet Singh Lotey, N.K. Verma, Magnetodielectric properties of rare earth metal-doped $BiFeO_3$ nanoparticles, Journal of Materials Science: Materials in Electronics, 24 (10) (2013) 3723-3729 (Springer).*

3. *Gurmeet Singh Lotey, N.K. Verma, Magnetoelectric coupling in multiferroic Tb-doped $BiFeO_3$ nanoparticles, Materials Letter, 111 (2013) 55-58 (Elsevier).*
4. *Gurmeet Singh Lotey, N K Verma, Structural, electrical, magnetic and multiferroism in Dy-doped $BiFeO_3$ nanoparticles, AIP Conference Proceeding 1536 (2013) 55-56 (American Institute of Physics).*

3.1 Structural, magnetic and electrical properties of Gd-doped $BiFeO_3$ nanoparticles with reduced particle size

In this section, a systematic study on the effect of both the reduced size of the synthesized nanoparticles as well as the doping on structural, magnetic, and ferroelectric properties of pure and Gd-doped $BiFeO_3$ nanoparticles have been presented. Pure and Gd-doped $BiFeO_3$ nanoparticles have been synthesized by sol-gel method, as discussed in detail in chapter 2. The series of samples of Gd-doped $BiFeO_3$ nanoparticles ($Bi_{1-x}Gd_xFeO_3$) with x = 0, 0.02, 0.04, 0.06, 0.08, 0.10, 0.12 and 0.15 have been prepared [3, 59-62]. The morphological, structural, magnetic, electric and magneto-dielectric/electric coupling properties of the as-synthesized nanoparticles have been measured.

3.1.1 Results and discussion

3.1.1.1 Structural and phase composition analyses

Figure 3.1 shows the XRD patterns of pure and Gd-doped $BiFeO_3$ nanoparticles. All the XRD reflection peaks of pure $BiFeO_3$ are indexed and well matched with rhombohedral structure (R*3c*) and have been found to possess hexagonal phase (JCPDS file no. 86-1518). No additional peaks of secondary impurities such as Fe_2O_3, Bi_2O_3, $Bi_2Fe_4O_9$, $Bi_{24}Fe_2O_{39}$ were detected in pure and $Bi_{1-x}Gd_xFeO_3$ ($x \leq 0.10$)nanoparticles. However, XRD patterns of $Bi_{1-x}Gd_xFeO_3$ (x = 0.12, 0.15) clearly reveal (Figure 3.2 (a)) some other peaks indicated by "*" have been observed; are attributed to secondary impurities phases. This indicates that $BiFeO_3$ doped with Gd remains pure with 'x' upto 0.1, indicating good the incorporation and dispersivity of Gd^{3+} ions into $BiFeO_3$ crystal structure, further increase in Gd content (x > 0.10) lead to formation of secondary phase impurities. This establishes that solution limitation for Gd doping in $BiFeO_3$ is around 10%. *Therefore the present study carried out for $Bi_{1-x}Gd_xFeO_3$ (x=0 to 0.10) nanoparticles.* XRD patterns (Figure 3.2 (b)) clearly indicate the structural transformation

because of increase in Gd content in the host $BiFeO_3$. Complete structural transformation from rhombohedral to orthorhombic takes place (Figure 3.2 (b)) as we increases Gd-doping concentration from 2 to 10 % in the host $BiFeO_3$.

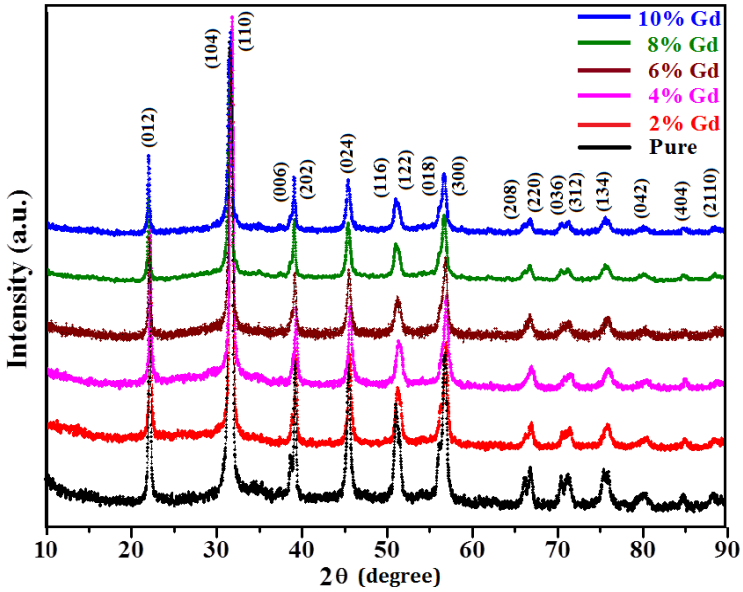

Figure 3.1X-ray diffraction patterns of pure and Gd-doped $BiFeO_3$ nanoparticles

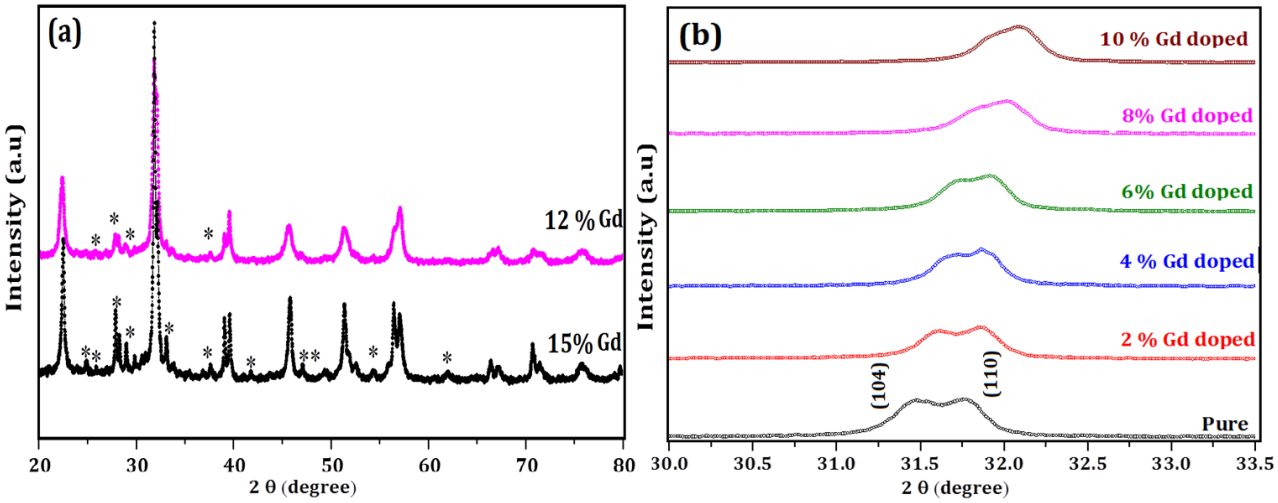

Figure 3.2 (a) XRD patterns of 12% and 15 % Gd-doped $BiFeO_3$ nanoparticles (b) Magnified XRD patterns of (104) and (110) reflection at $2\theta = 32^o$ for pure and Gd-doped $BiFeO_3$ nanoparticles

From Figure 3.2 (b), it is clear that the decrease in the splitting of (104) and (110) peaks in $Bi_{1-x}Gd_xFeO_3$ nanoparticles around $2\theta = 32^o$ indicates reduction of the rhombohedral phase and increase that of the orthorhombic phase ($Pn2_1a$).Similar phenomenon of phase transformation with addition of rare earth metals in $BiFeO_3$ host material had been observed by other groups [83-88].No additional peaks related to Gd in $Bi_{1-x}Gd_xFeO_3$ ($x \geq 0.10$) XRD patterns is observed indicating good dispersivity and incorporation of dopant in the host material.Table 3.1 shows the strain of the pure and Gd-doped $BiFeO_3$ nanoparticles calculated using modified Debye-Scherer equation [85]. It has also been observed from Table 3.1 that lattice strain linearly increases as the concentration of Gd in $BiFeO_3$ is increased, resulting in lattice deformation.

Table 3.1 Effect of Gd-doping on different parameters

Sample	Particle size (nm) TEM	Lattice strain	Saturation Magnetization (emu/g)
Pure $BiFeO_3$	25	0.00687	3.21
$Bi_{0.98}Gd_{0.02}FeO_3$	22	0.00753	3.63
$Bi_{0.96}Gd_{0.04}FeO_3$	21	0.00962	4.29
$Bi_{0.94}Gd_{0.06}FeO_3$	20	0.01050	4.87
$Bi_{0.92}Gd_{0.08}FeO_3$	17	0.01168	6.61
$Bi_{0.90}Gd_{0.10}FeO_3$	15	0.01386	10.11

3.1.1.2 X-ray photoemission (XPS) analysis

Chemical bonding and oxidatiion states of Bi, Fe, O and Gd analyses by XPS through wide range of spectrum from 0 to 1000 eV of pure and 10% doped-$BiFeO_3$ nanoparticles is shown respectively in Figure 3.3 (a) and 3.3 (b).Figure 3.3 (c) show the two main photemission peaks at 711.3 and 723.8 eV, assigned to Fe^{3+}, $2p_{3/2}$ and $2p_{1/2,}$ are spin orbit doublet of Fe^{3+}oxidation state. In addition to these, in Figure 3.3 (c), other three peaks positioned around 706, 715 and 717 eV called, respectively, pre-peak, surface peak and satelitte-peak have been also observed. The pre-peak has been noticed due to surface and lattice defects in nanopartcles. The surface-peak observed at 715 eV is due to decrease of co-ordination number of Fe^{3+} cations located at surface of nanoparticles, and, the satellite-peak around 717 eV, due to shake-up process. In this

process, when the ejection of photoelectrons from 2**p** shell take place, a small amount of kinetic energy of photolectrons is lost during promoting the movement of electron from 3**d** orbital to empty 4**s** orbital, and, as a result of this, a peak related to this corresponding energy loss has been observed.

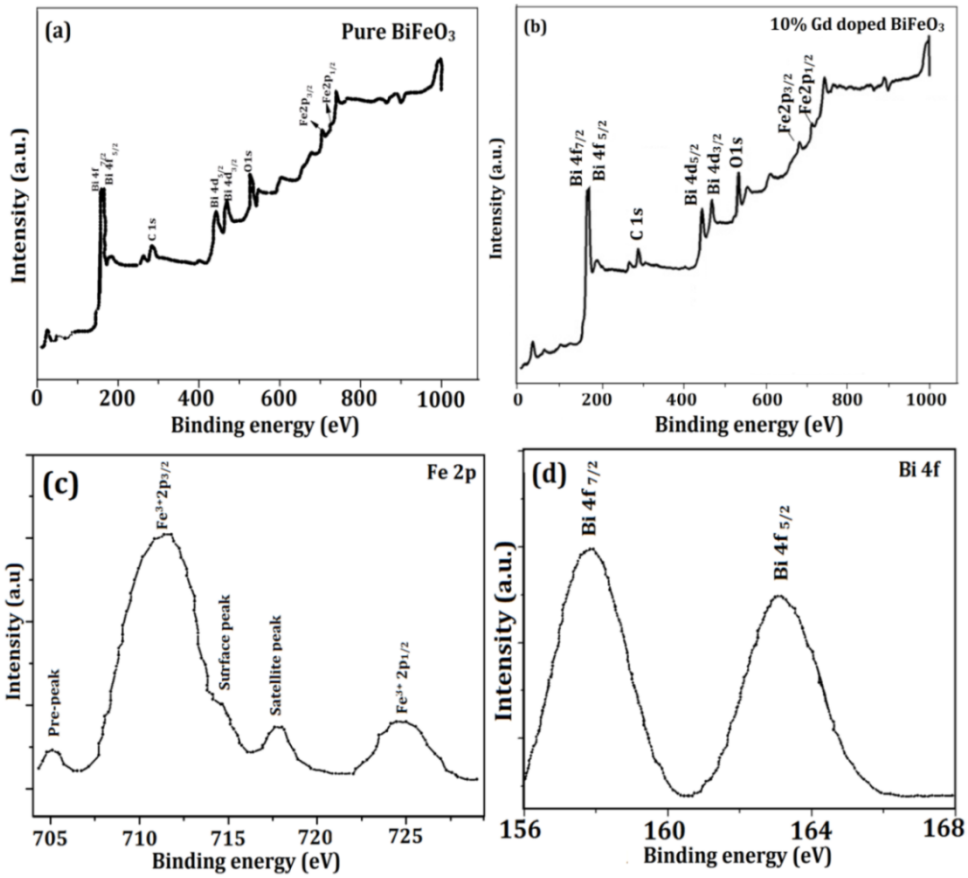

Figure 3.3 XPS wide range spectrum analysis of (a) pure $BiFeO_3$ nanoparticles (b) 10 % Gd-doped $BiFeO_3$ nanoparticles (c) Fe 2p and (d) Bi 4f

No additional peak corresponding to Fe^{2+} oxidation has been observed in XPS, which indicates the dominant role of Fe^{3+} ion for observed ferromagnetism in pure and Gd-doped $BiFeO_3$ nanoparticles in magnetic study (Figure 3.6). Two peaks positioned at 158 and 164 eV corresponding to Bi $4f_{7/2}$ and Bi $4f_{5/2,}$ respectively, in Figure 3.3 (d) confirm the trivalent oxidation states of Bi, i.e., Bi^{3+} in pure and doped-$BiFeO_3$ nanoparticles. No peaks related to Gd in its mettalic or oxide form (Gd and Gd_2O_3) have been observed in XPS (Figure 3.3 (b). This confirms that Gd is likely to play the role of Bi, which also matches the XRD measurement

(Figure 3.1). The peak O1s observed at 530.8 eV is attributed to O^{2-}oxidation state in $BiFeO_3$ lattice. Therefore, the XPS spectrum reveals the presence of Bi, Fe and O without any other trace of impurities except a small amount of adsorbed carbon peak C1s at 285 eV that was used to calibrate the system. In addition to this, no extra peaks of any impurities or secondary phase, observed in XPS spectrum, confirm the high purity of samples [85].

3.1.1.3 TEM, HRTEM and SAED analyses

Figures 3.4 (a) to 3.4 (f) show TEM images of pure, 2%, 4%, 6%, 8% and 10 % Gd-doped $BiFeO_3$ nanoparticles. It is clear from Figure 3.4 that particles are homogenous, well-dispersed, without any aggregation and possess spherical symmetry with the average particle size lying between 25-15 nm, respectively, for pure and Gd-doped $BiFeO_3$ nanoparticles.This observed decrease in crystallites' size is due to smaller radius of Gd^{3+} ions as compared to that of Bi^{3+}. Clear lattice fringes have been observed in both samples indicating the defect-free nature of the samples with high degree of crystallinity. The interplanar distance has been found to be around 1.19 nm and 0.80 nm, respectively, for pure and 10% Gd-doped $BiFeO_3$ nanoparticles.

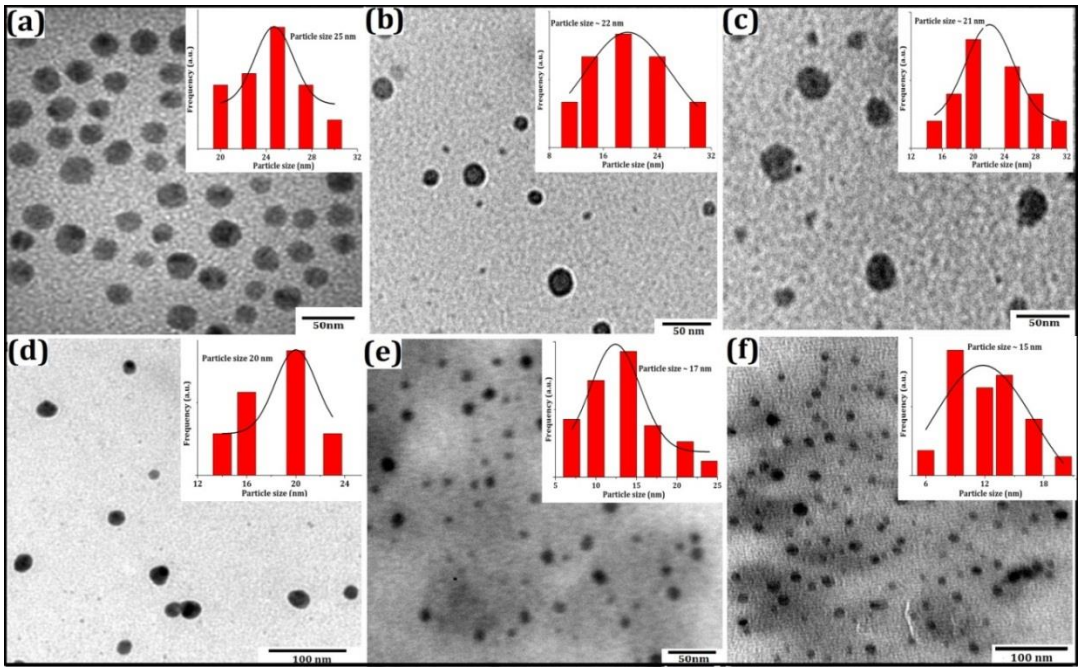

Figure 3.4 TEM image of (a) Pure $BiFeO_3$ (b) 2 % (c) 4 % (d) 6 % (e) 8% (f) 10 % Gd-doped $BiFeO_3$ nanoparticles

Figure 3.5 (b) and (d) show the indexed SAED patterns of pure and 10% Gd-doped $BiFeO_3$ nanoparticles.The sharp circular distinct ring patterns manifesting the crystallinity of the individual nanoparticles and the SAED rings, being discrete spots and not continuous, suggest not only the complex polycrystalline nature but also a preferential orientation of the synthesized pure and Gd-doped $BiFeO_3$ nanoparticles.The indexed electron diffraction patterns also support the rhombohedral and orthorhombic structure of pure and Gd-doped $BiFeO_3$ nanoparticles,respectively, corroborate with XRD.

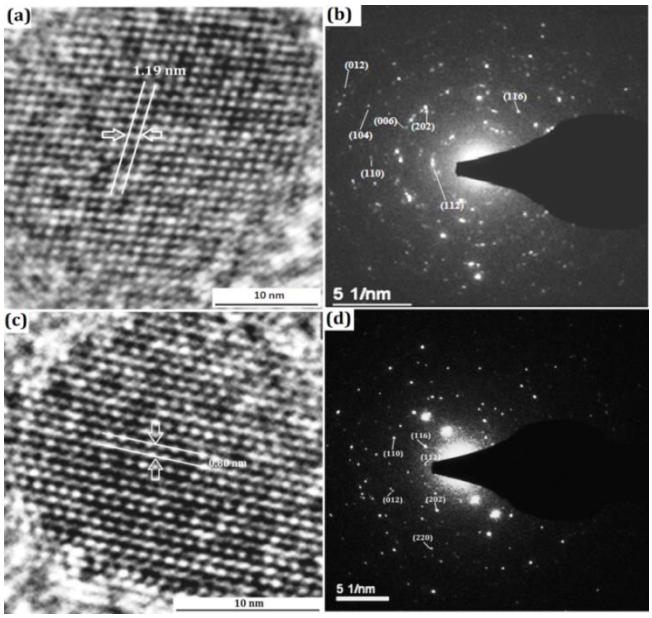

Figure 3.5 HRTEM image of (a) pure and (c)10% Gd-doped $BiFeO_3$ individual nanoparticles. SAED pattern of (b) pure and (d) 10% Gd-$BiFeO_3$ nanoparticles

3.1.1.4 Magnetic analysis

Figure 3.6 shows the room temperature magnetization - the magnetic field (M-H) loop of pure and Gd-doped $BiFeO_3$ nanoparticles. The M-H loops of all the samples measured at room temperature (Figs. 3.6 (a) and (b)), indicating the saturation magnetization (Ms) achieved in pure and $Bi_{1-x}Gd_xFeO_3$ ($x \leq 0.8$) samples within the applied field of 10 kOe, reveal the typical ferromagnetic character of the samples. However 8% and 10% Gd-doped $BiFeO_3$ samples get saturated at higher magnetic field 20 kOe (Figure 3.6 (b)).It has been found (Figure 3.7 (a)) that the doping of Gd ions enhance the saturation magnetization of $Bi_{1-x}Fe_xO_3$ samples, i.e., with

increase in doping concentration of Gd in $BiFeO_3$, the saturation magnetization increases.The saturation magnetization (Ms) of the $Bi_{1-x}Gd_xFeO_3$ nanoparticles have been found to be higher than that of bulk $BiFeO_3$ [84].

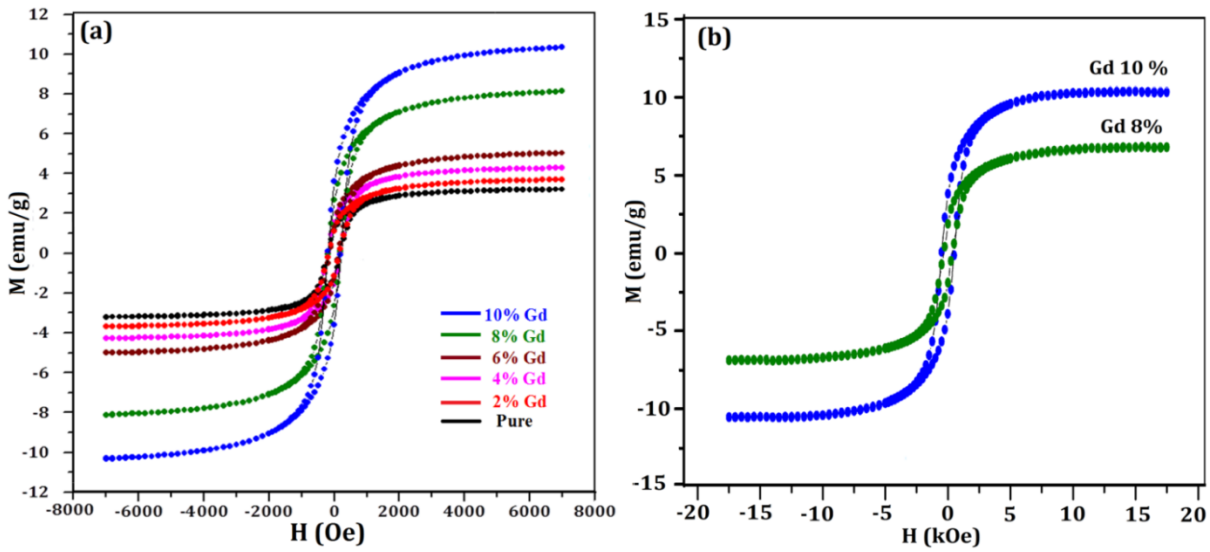

Figure 3.6 (a)M-H hysteresis curves of pure and Gd-doped $BiFeO_3$ nanoparticles and (b) M-H hysteresis curves of 8% and 10 % Gd-doped $BiFeO_3$ nanoparticles recorded at high magnetic field

As discused above (XPS study), the observed ferromagnetic character is not because of the presence of any impurities or due to the presence of Fe^{2+} ion in the pure and doped $BiFeO_3$ nanoparticles. The observed high value of magnetization saturation, and the ferromagnetic character can be explained on the basis of two facts. Firstly,due to the effect of doping of magnetically active ions, which may further be because of two reasons:

- The radius of Gd^{3+} ion being smaller than that of the Bi^{3+} ion result in larger distortion in lattice structure (Table 3.1) thereby leading to suppresion of spiral spin modulation; this is precisely because the spin cycloid of $Gd^{3+}$is destroyed when the structure is changed from rhobhohedral to orthorhombic, as has already been observed in XRD study
- The first principle calculation suggesting that the effective magnetic moment of Gd^{3+} is large (8.0 μB), so the magnetically active Gd^{3+} ions coupled with Fe^{3+} ions can produce improved magnetism [84].

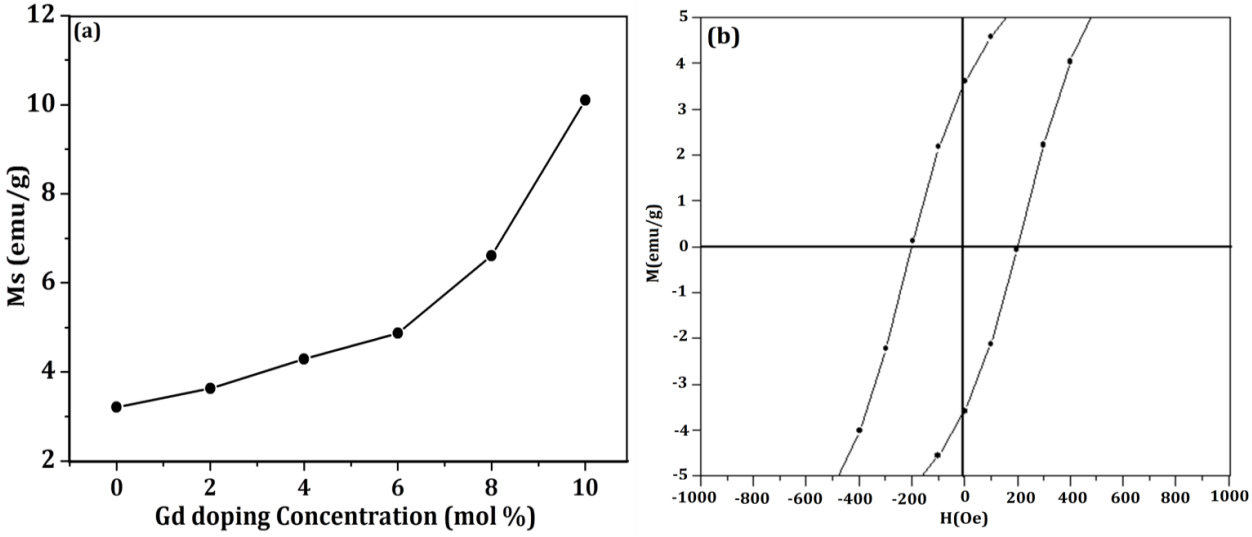

Figure 3.7 (a) Variation of saturation magnetization (Ms) with varying Gd concentration and (b) No shift in hysteresis loop for 10 % Gd-doped $BiFeO_3$ nanoparticles

Secondly, due to the effect of size of pure and Gd-doped $BiFeO_3$ nanoparticles, which may further be because of two reasons:

- Due to the presence of spiral spin structure in bulk $BiFeO_3$, the antiferromagnetic axis rotates through the crystal with an incommensurate long-wavelength period of 62 nm thereby cancelling the macroscopic magneization and inhibiting the linear magnetoelectric effect [86]. However, as in our case, the size of the synthesised pure and Gd-doped $BiFeO_3$nanoparticles lies between 25 - 15 nm, which being less than 62 nm, modifies the cycloidal spin structure and, thus, leads to the observed ferromagnetic ordering as has been reported earlier [40, 84, 87].
- M-H curve for 10% Gd-doped $BiFeO_3$ (Figure 3. 7(b)) shows that there is no shift in the hysteresis loop towards negative or positive axis, indicating no exchange coupling between the antiferromagntic core and ferromagnetic surface [88]. This establishes that the observed ferromagnetism is not due to the exchahge interaction.

Consequently, the small size of pure and Gd-doped $BiFeO_3$ nanoparticles; lattice distortion in the crystal structure; and, doping of magnetically active ion lead to enhancement in the saturation magnetization and ferromagnetic character.

.

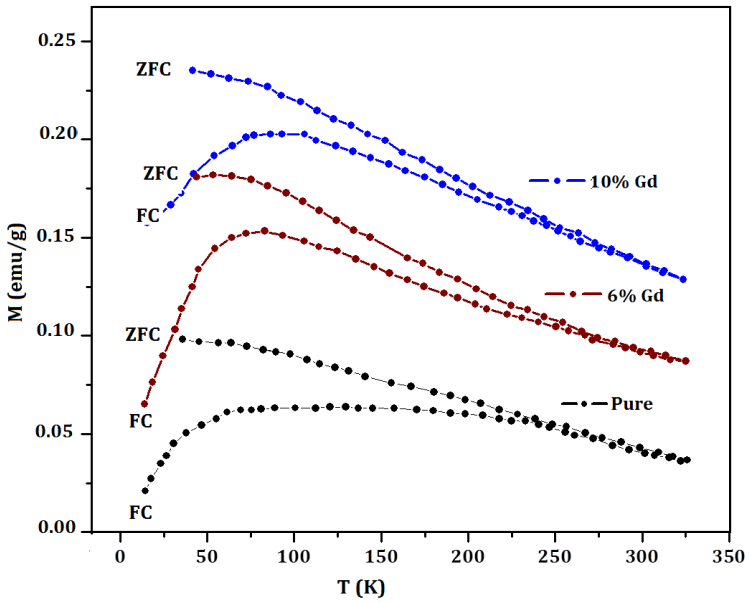

Figure 3.8 Temperature dependence of magnetization for (a) pure, (b) 6 % and (c) 10% Gd-doped $BiFeO_3$ nanoparticles, showing zero field cooling (ZFC) and field cooling (FC) curves with applied field 1000 Oe

Figures 3.8 shows the magnetization versus temperature curves for the pure, 6 % and 10% Gd-doped $BiFeO_3$ nanoparticles showing zero field cooling (ZFC) and field cooling (FC) modes in applied external field of 1000 Oe. The ZFC and FC (Figure 3.8) curves show broad peak at lower temperature due to nanosize effect in pure and Gd-doped $BiFeO_3$ nanoparticles. However, no such peaks are observed in bulk samples having particle size higher than the critical spin spiral ordering (62 nm) [85]. The size of the synthesized $BiFeO_3$ nanoparticles, being smaller than the critical spin spiral struture (62 nm), results in the orientation of Fe^{3+} spins towards the direction of applied field generated by the breaking of antiferromagnetic sprial ordering [85].The splitting between ZFC and FC curves takes place below 250 K and the divergence between ZFC and FC increases with decrease in temperature. These splitting between the ZFC and FC, observed in pure and Gd-doped $BiFeO_3$ nanoparticles, confirms the spin-glass behaviour of the synthesied nanoparticles [89]. The observed spin-glass is due to the nanosize effect, lattice distortion and phase transformation from rhombhohedral to orthorombic as observed in XRD [83].

3.1.1.5 Morphological study

Figures 3.9 (a) to 3.9 (e) show the scanning electron micrographs of sintered pellets of pure and Gd-doped $BiFeO_3$at different magnifications.It is evident from the Figure 3.9 (a) that the grains of pure $BiFeO_3$ sample are large, rectangular in shape, and their size lying between 1.5 – 2.0 μm.

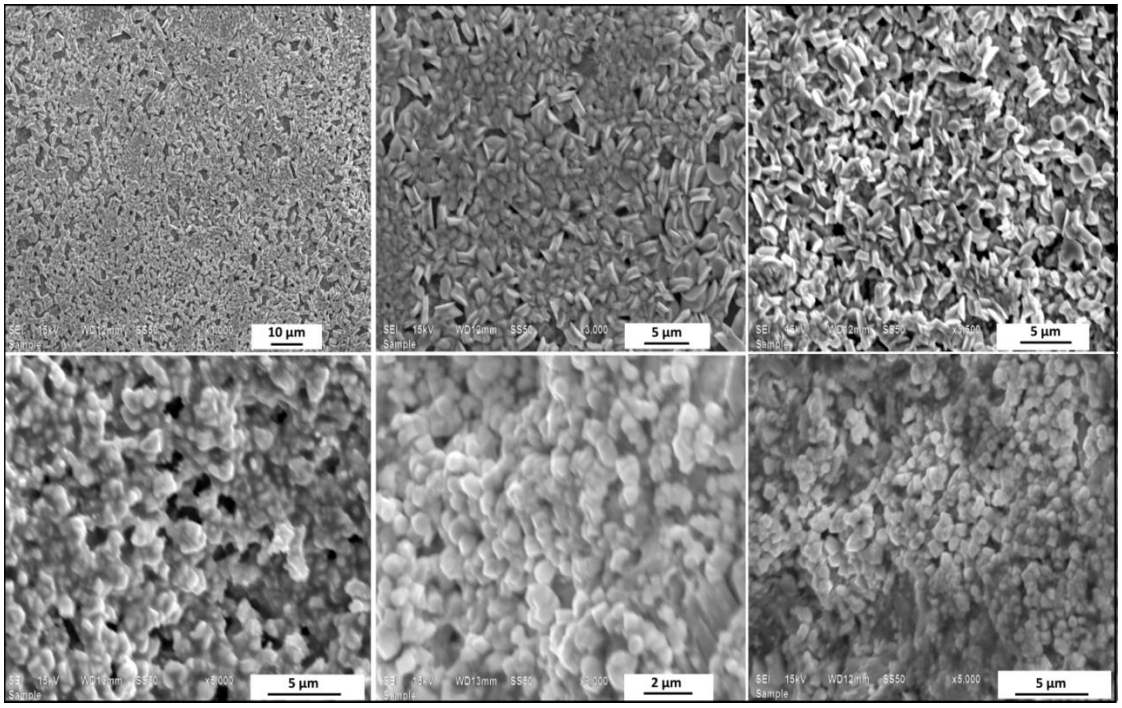

Figure 3.9 SEM micrographs of (a) pure $BiFeO_3$ and (b) 2% (c) 4 % (d) 6 % (e) 8% (f) 10% Gd-doped $BiFeO_3$ pellets

On doping 2% and 4 % Gd in $BiFeO_3$, the grain shape continues to be rectangular but their average size reducing to 0.8 – 1.2μm. However, addition of 6 % Gd in $BiFeO_3$ results in aggregated clusters with non-uniform morphology. Further, changing Gd concentration to 8% and 10% Gd, there results spheroidal grains having still smaller size 0.5 – 0.7 μm. The smaller grain size is due to smaller size of Gd^{3+} ions as compared to those of Bi^{3+}ions, and results in lattice contraction

3.1.1.6 Leakage current (J-E) characteristics

Figure 3.10 shows the leakage current (J-E) characteristics of pure and Gd-doped pellets. At applied fieldof 100 kV/cm, the leakage current density of 10% Gd-doped $BiFeO_3$ comes out to be

about $9.50x10^{-5}$ A/cm^2, which is about four orders of magnitude less than that of pure $BiFeO_3$(8.70×10^{-1} A/cm^2). This clearly reveals that the leakage current density can be effectively reduced by Gd doping in host $BiFeO_3$. The high leakage current observed in pure $BiFeO_3$ is attributed to the space charges such as oxygen vacancies, defects and volatilization of Bi [90].

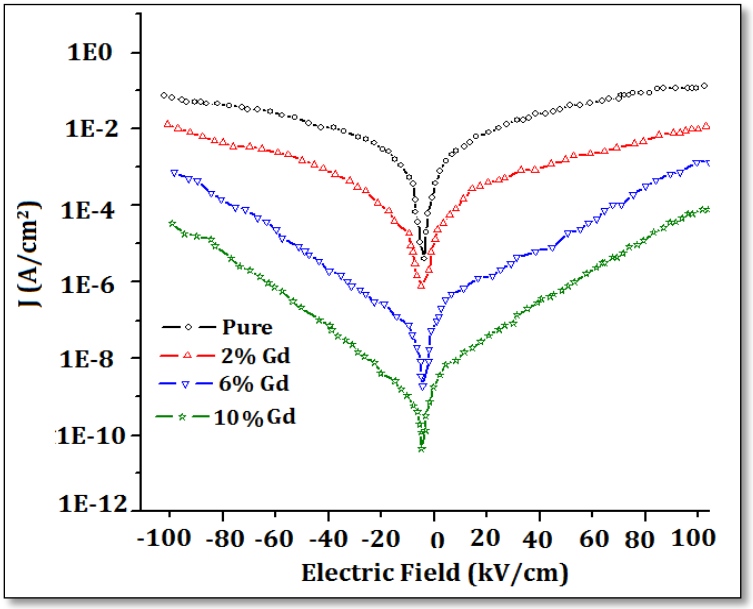

Figure 3.10 Leakage current density (J) versus electric field (E) curves for the pure and Gd-doped $BiFeO_3$

The oxygen vacancies in ceramics act as trapping centers. The trapped electrons can be activated for conduction on applying electric field, which results in increasing the leakage current density in ceramics [88]. However, the substitution of Gd for Bi reduces the defects and decreases the oxygen vacancies as a result, the leakage current density decrease. The ferroelectric properties of doped $BiFeO_3$ also get enhanced due to mismatch between the radii of Bi and Gd ions. The reduction in leakage current density of 10% Gd-doped $BiFeO_3$ can, therefore, be attributed to structural change from rhombohedral to orthorhombic. Abe et al. 2010 [91] report similar observation of reduction in leakage current density on 10 % Ti^{4+} doping in $BiFeO_3$. Due to the large grain boundary area coupled with higher space charge density also results in higher leakage current in $BiFeO_3$ ceramics [92]. However in our case with Gd doping the grain size of doped

$BiFeO_3$ decreases that results in lower space charge density and hence leakage current density decreases.

3.1.1.7 Polarization versus electric field (P-E) loop analysis

Figure 3.11 shows the polarization versus electric field hystersis (P-E) loops of pure and Gd-doped $BiFeO_3$ pellets sintered at 450^{o}C. Further, the Figure 3.11 shows that the P-E loop for pure $BiFeO_3$ has an elliptical shape, which is caused by high leakage current (Figure 3.10). However, the doping of Gd in $BiFeO_3$ significantly effects the ferroelectric properties. Doping of Gd in $BiFeO_3$ host material results in well saturated rectangular shape like P-E loops revealing the good ferroelectric properties.

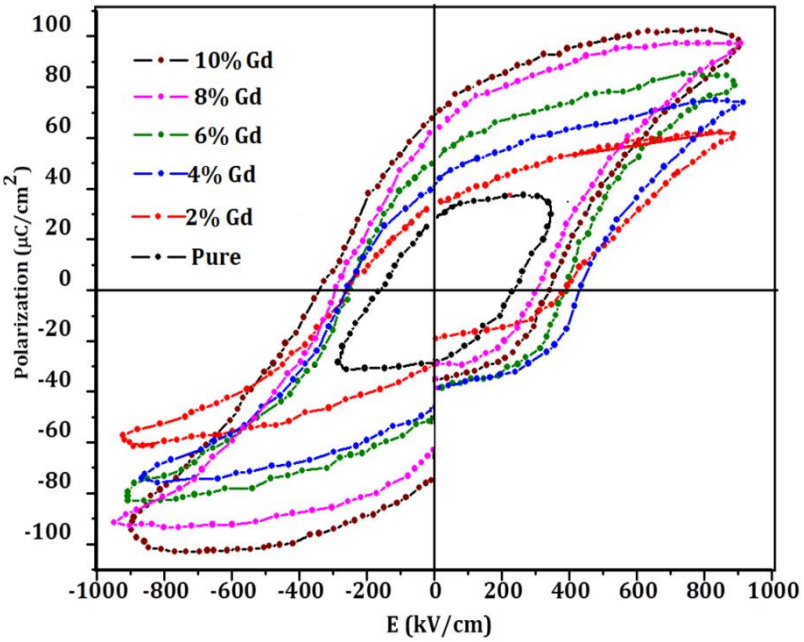

Figure 3.11 Polarization versus electric field (P-E) hysteresis loop of pure and Gd doped $BiFeO_3$

Figure 3.11 (a) shows that increase in Gd doping increases the saturation polarization (Ps).The enhancedment in spontaneous polarization in doped $BiFeO_3$ can be explained as under:

- XRD (Figure 3.1) shows that addition of Gd in $BiFeO_3$ changes its structure from rhombhoheral to orthorhombic, which results in lattice distortion in rhombhohedral perovskite struture – a favorable increase in spontaneous polarization. Doping decreases the oxygen-related defects, which further reduces the leakage current (Figure 3.10)

thereby improving the domain pinning effects [93-94], and enhancing the spontaneous polarization [95].

- Doping decreases the average grain size that results in lower space charge density, smaller leakage current density [92] and this increases spontaneous polarization.

3.2 Magnetoelectric coupling in multiferroic Tb-doped $BiFeO_3$ nanoparticles

In this section, magnetoelectric coupling in multiferroic Tb-doped $BiFeO_3$ nanoparticles have been presented. The effect of Tb-doping and the smaller size of synthesized nanoparticles on structural, magnetic and magnetoelectric coupling have been studied. $Bi_{1-x}Tb_xFeO_3$ nanoparticles (x = 0 to 0.15) have been synthesized by sol-gel method as describes in chapter 2 [59].

3.2.1 Results and discussion

3.2.1.1 Crystallographic and morphological analysis

TEM images of pure and 15% Tb-doped $BiFeO_3$ nanoparticles (Figure 3.12 (a) and (b)) reveal that the average particle size of synthesized nanoparticles is 39 and 30 nm, respectively.

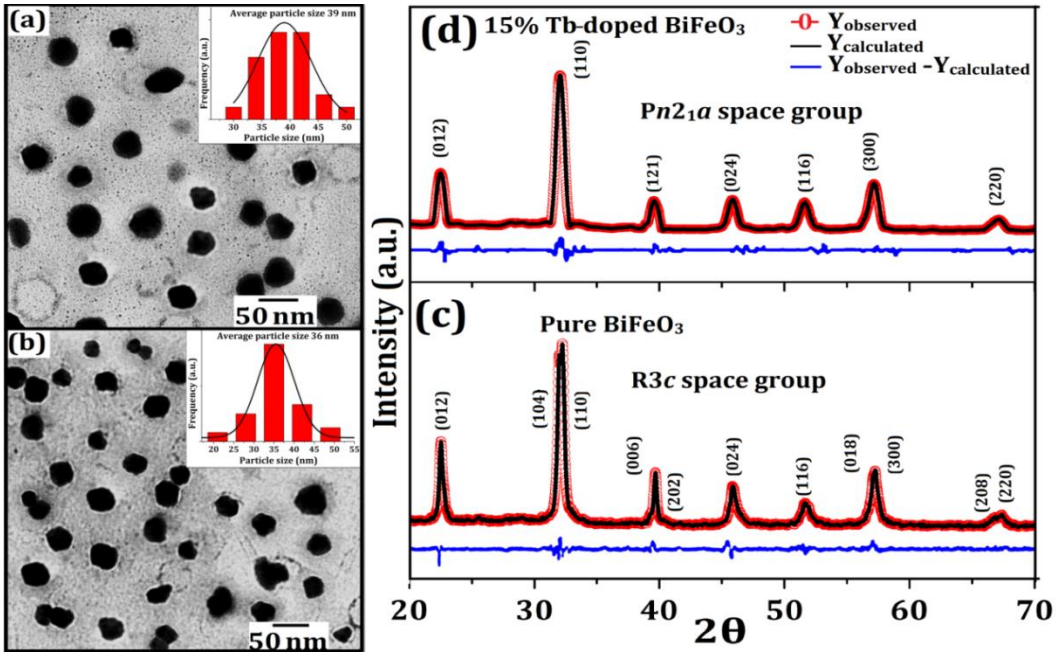

Figure 3.12 TEM images and XRD patterns of (a, c) pure and (b, d) 15% Tb-doped $BiFeO_3$ nanoparticles

The nanoparticles are found to be spherical, homogenous in size, well-dispersed and without any agglomeration. Rietveld refinement of XRD patterns have been performed using MAUD software. The peaks are well indexed with *hkl* planes, and best fitting of XRD patterns has been observed using rhombohedral lattice (R3*c*) for $x \leq 0.10$, and orthorhombic lattice (P$n2_1a$) for x = 0.15.Figure 3.12 (c) shows that pure $BiFeO_3$ nanoparticles possess rhombohedral structure and hexagonal phase with R3*c* space group (JCPDS-86-1518). Two features in XRD patterns have been observed with Tb-doping. First, the reflection peaks around $2\theta = 32^o$; 39^o and 57^o,corresponding to (104), (110); (006), (202) and (018), (300) planes, assigned to rhombohedral phase (R3*c*), have been found to disappear for pure $BiFeO_3$ nanoparticles, whereas they appear as single peaks corresponding to (020), (121) and (222) planes for 15% Tb-doped $BiFeO_3$ nanoparticles. Second, the Rietveld refined XRD pattern of 15% Tb-doped $BiFeO_3$ nanoparticles, as shown in Figure 3.12 (d), matches well with the orthorhombic structure of $BiFeO_3$ having P$n2_1a$ space group. Rietveld refinement establishes that 15% Tb-doped $BiFeO_3$ nanoparticles have orthorhombic structure, while 5% and 10% Tb-doped nanoparticles are composed of mixed phases, R3*c* = 92%, P$n2_1a$ = 8% and R3*c* = 84%, P$n2_1a$ = 16%, respectively (Table 3.2).Therefore, it is concluded that 15% Tb-doping results in complete structural transformation from rhombohedral (R3*c*) to orthorhombic (P$n2_1a$) phase [65, 94].The absence of peaks related to secondary phase or impurities reveal the high purity of the synthesized nanoparticles [65].Table 3.2 lists the crystallographic parameters of the synthesized nanoparticles derived from Rietveld refinement. It also shows that the lattice strain linearly increases as a function of Tb concentration.

3.2.1.2 Magnetic analysis

Figure 3.13 shows M-H hysteresis loops of the synthesized nanoparticles with saturation magnetization; this demonstrates the ferromagnetic character of the synthesized nanoparticles. Bulk $BiFeO_3$ is G-type antiferromagnetic due to the spin-spiral incommensurate modulated structure with large cycloidal period of 62 nm; this originates from the half-filled, high spin and localized ($t^2_{2g}e^2_g$) Fe^{3+} ions [64-65, 95-97]. The size of synthesized nanoparticles is 30-39 nm (Figure 3.12), which is smaller than the cycloidal period; this results in the destruction of spin-spiral incommensurate modulated structure and leads to ferromagnetism. Therefore, it can be said that the quantum confinement is responsible for the ferromagnetism. Further, the non-exact

compensation of the two magnetic sub-lattices at the surface of synthesized nanoparticles produces net magnetic moment and may be a primary cause of ferromagnetism [40, 3, 64-65, 98-99].

Table 3.2 Rietveld structural refinement crystallographic parameters of $Bi_{1-x}Tb_xFeO_3$ nanoparticles

Sample description	Structural model	Lattice parameters (Å)		Atom coordinates			Strain	R_{wp}(%)
				Bi/Tb	Fe	O		
Pure $BiFeO_3$	R3*c*	*a*=5.576	*x*	0.0000	0.0000	0.3511	0.084	9.74
		c=13.85	*y*	0.0000	0.0000	0.2169		
			z	0.0000	0.22512	-0.0879		
5% Tb-doped $BiFeO_3$	R3*c* (92%)	*a*=5.577	*x*	0.0000	0.0076	0.4219	0.097	8.67
		c=13.847	*y*	0.0000	0.0011	0.0221		
			z	0.0000	0.21519	0.0986		
	P*n*2$_1$*a* (8%)	*a*=5.539	*x*	0.1210	-0.0062	0.4029		
		b=7.418	*y*	0.1470	0.0006	0.0929		
		c=5.240	z	0.9771	0.3529	0.3387		
10 % Tb-doped $BiFeO_3$	R3*c* (84%)	*a*=5.5631	*x*	0.0000	0.0000	0.5240	0.134	9.43
		c=13.870	*y*	0.0000	0.0000	0.0250		
			z	0.0000	0.6420	0.4910		
	P*n*2$_1$*a* (16%)	*a*=5.424	*x*	0.0190	-0.0059	0.4260		
		b=7.618	*y*	0.1740	0.0008	0.9420		
		c=5.398	z	0.9690	0.2197	0.3420		
15 % Tb-doped $BiFeO_3$	P*n*2$_1$*a*	*a*=5.522	*x*	0.0290	-0.0074	0.4391	0.163	7.84
		b=7.418	*y*	0.2120	0.0012	0.0963		
		c=5.354	z	0.4740	0.2164	0.3572		
	P*nma*	*a*=5.598	*x*	0.0290	0.0000	0.4413		
		b=7.676	*y*	0.2210	0.0000	0.0974		
		c=5.329	z	0.9730	0.5000	0.1491		

The saturation magnetization (M_s) has been found to increase with doping (inset, Figure 3.13). The maximum Ms, 2.92 emu/g, has been observed for 15% Tb-doped $BiFeO_3$ nanoparticles. Terbium (Tb) ions have high magnetic moment. Therefore, upon their substitution in $BiFeO_3$, spin-interactions between Tb^{3+} and Fe^{3+} may decouple the antiferromagnetic interactions across the Fe^{3+} ions, and results in the ferromagnetic coupling between Tb^{3+} with Fe^{3+}; this enhances ferromagnetism [65]. Tb-doping, also results in different bond interactions between 4f and 5d orbitals of Tb-O and 6p orbitals of Bi-O leading to ferromagnetic coupling. The structural transition from rhombohedral to orthorhombic phase, releases the latent magnetization locked within the spin cycloid, and consequently, this enhances the ferromagnetism [100]. Doping results in high lattice strain (Table 3.2); this results in the higher spin canting and giving rise to ferromagnetism [101-103].

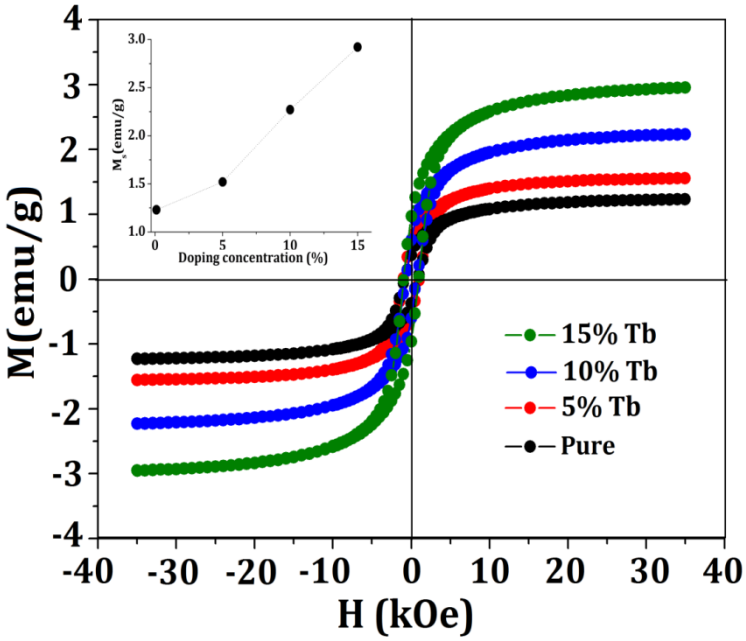

Figure 3.13 M-H hysteresis loops of $Bi_{1-x}Tb_xFeO_3$ nanoparticles

3.2.1.3 Magnetoelectric coupling analysis

Figure 3.14 shows longitudinal (L-α_{ME}) and transverse (T-α_{ME}) ME coefficients of synthesized $Bi_{1-x}Tb_xFeO_3$ nanoparticles at room temperature, reflecting their hysteretic behavior. The ME coefficients (α_{ME}) have been calculated using the following relation [80-81]:

$$\alpha_{ME} = \frac{\delta E}{\delta H} = \frac{V_{out}}{h_o t}$$

where, t is thickness of the sample, V_{out} is the AC magnetoelectric voltage appearing across the sample surface (measured by the lock-in-amplifier), h_o is the amplitude of the AC magnetic field. It has been found that both L-α_{ME} and T-α_{ME} increase quickly with increase in bias magnetic field, and, attain maximum value, L-α_{ME} = 11.01, 10.35, 11.92, 13.18 mV/cm.Oe and T-α_{ME} = 6.81, 6.85, 6.88, 7.86 mV/cmOe, respectively, for x = 0, 0.05, 0.10, 0.15; this showing L-α_{ME} exceeds T-α_{ME}. The observed values of L-α_{ME} and T-α_{ME} are much higher than as reported by Naik [80] for bulk and Caicedo [81]for thin films of $BiFeO_3$. The smaller value of ME coefficients observed in bulk and thin films [80-81] is due to the presence of secondary phases, large grain size, and charge imbalance of Fe, i.e.$Fe^{2+} \leftrightarrow Fe^{3+}$. The observed ME in the present case can be attributed to quantum confinement, spin-exchange constrictions, exchange-interactions and magnetostriction effect [3, 40,64-65, 81, 96-97]. The as-synthesized nanoparticles get strained with applied magnetic field due to the coupling between electric and magnetic domains.

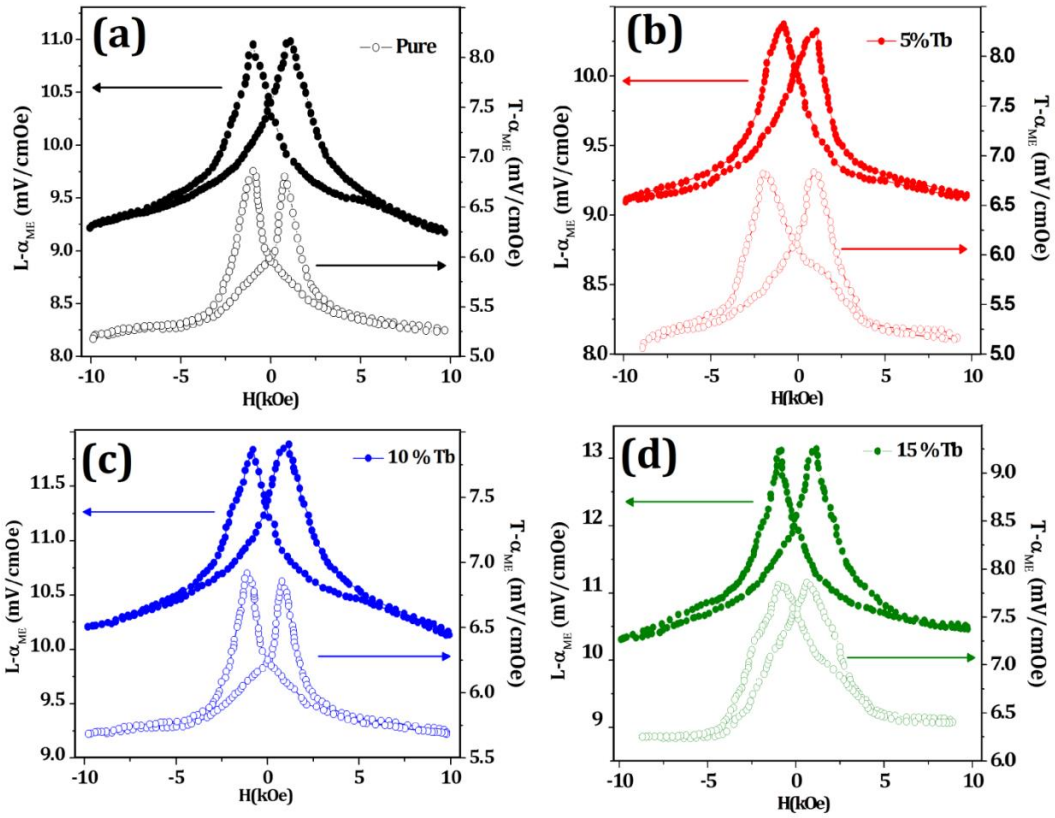

Figure 3.14 ME coefficients of (a) pure (b) 5% (c) 10% and (d) 15% Tb-doped $BiFeO_3$ nanoparticles

This induces stress in it, and generates electric field. The induced electric field orients the ferroelectric domains, and, leads to observed ME. The doping of Tb metal in $BiFeO_3$further enhances ME coefficients. The observed high value of ME coefficients in Tb-doped $BiFeO_3$nanoparticles is attributed to the increase in magnetic ordering with the doping of Tb (as discussed in section 3.2), which strengthen the sub-lattice interactions [64, 65].Also, the exchange interactions and spin-exchange constrictions between the Tb^{3+} and Fe^{3+} spins, collapses the modulated spin-spiral structure, and thereby enhancing ME. The interactions between 4f electrons of Tb^{3+} and 3d electrons of Fe^{3+} spins, when magnetic field is applied, lead to first, parallel distribution of Fe spins with magnetic moments of adjacent Tb^{3+} ions; second, antiparallel distribution of Fe spins with successive Tb^{3+} ions. This result in cooperatively shifting of Tb^{3+} layers towards or away from Fe^{3+} layers with antiparallel or parallel spins through magnetostriction; this results in polarization and consequently ME enhanced [64, 65, 97]. The wide-range scattering in the ME coefficients has been noticed due the nano-size of the synthesized nanoparticles. In bulk $BiFeO_3$, the long range cycloidal period (62 nm) results in antiferromagnetic ordering; this cancels the macroscopic magnetization and inhibits ME effect [40, 3, 64-65, 80-81]. The size of the as-synthesized nanoparticles is 30-39 nm, which is less than the critical size of $BiFeO_3$, i.e., cycloidal period; this leads to destruction of antiferromagnetic ordering, modifies the domain structure, and, thereby results in magnetoelectric coupling [40, 3, 64-65, 80-81]. Table 3.2 shows that synthesized nanoparticles possess high strain, which increase with doping; this may also result in higher spin canting and, consequently ME.

3.3 Magnetodielectric properties of rare earth metal-doped $BiFeO_3$ nanoparticles

In this section, phase-dependent magnetoelectric properties of pure and rare earth metal ions (Gd^{3+}, Tb^{3+}, Dy^{3+})-doped $BiFeO_3$ nanoparticles have been investigated. Pure and rare earth metal-doped $BiFeO_3$ nanoparticles have been synthesized by the sol-gel method as discuss in chapter 2. The effect of doping as well as phase transformation on structural, magnetic, dielectric and magnetodielectric properties of synthesized nanoparticles have been investigated [62].

3.3.1 Results and discussion

3.3.1.1 Morphological and Crystallographic

TEM images of the synthesized nanoparticles reveal their spherical morphology as shown in Figure 3.15. The particle size of the synthesized nanoparticles has been calculated by plotting histograms, as shown in inset of Figure 3.15. It is found to be 44, 46, 25, 36 nm for pure, Gd, Tb and Dy doped$BiFeO_3$ nanoparticles, respectively (Table 3.3). Figure 3.16 shows XRD patterns of pure $BiFeO_3$ nanoparticles appropriately indexed corresponding to polycrystalline rhombohedral distorted perovskite (R3c) structure with hexagonal phase (JCPDS file no. 86–1518) [3, 25, 30, 64-65, 104-107]. A few peaks marked by "*" attributed to secondary impurity such as $Bi_2Fe_4O_9$, have been observed but these impurity phases are found to be non-ferromagnetic at room temperature (JCPDS file no. 20-0836) [104]. XRD patterns of RE-doped $BiFeO_3$ nanoparticles show that the splitting of diffraction peaks observed around $2\theta \sim 31\text{-}32^o$ and $39\text{-}39^o$ in pure $BiFeO_3$ nanoparticlesdecreased, and, got merged to single peak corresponding to the orthorhombic phase with P$n2_1a$ space group (inset Figure 3.16) [3, 64-65, 108-110]. This shows that there is structural transition from rhombohedral (R$3c$) to orthorhombic (P$n2_1a$) phase with doping of 15% RE.

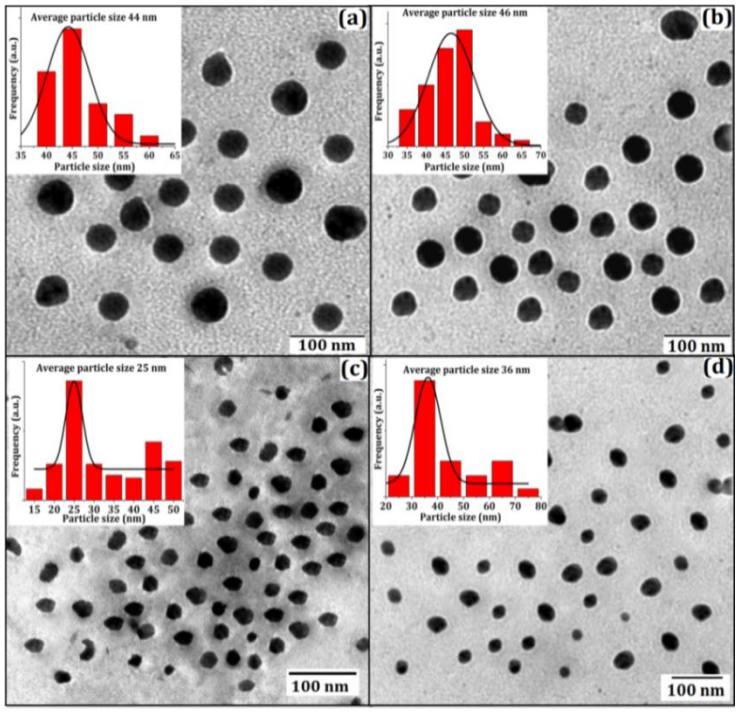

Figure 3.15TEM images of (a) pure and (b) 15% Gd (c) 15 % Tb (d) 15% Dy, doped $BiFeO_3$ nanoparticles. Inset shows histograms used to calculate particle size of synthesized nanoparticles

The orthorhombic ($Pn2_1a$) phase possesses distorted structure, and is non-centrosymmetric; Therefore, RE-doped nanoparticles will have good dielectric and magnetodielectric coupling.The origin of the observed structural transition can be explained on the basis of size effect of RE dopants and tolerance factor (t) [108-110]:

$$t = \frac{(R_A + R_O)}{\sqrt{2}(R_B + R_O)}$$

where R_A, R_B, and R_O are the ionic radii of A, B and O, respectively, in ABO_3 perovskite structure.Table 3.3, shows the value of tolerance factorto be 0.954, 0.951, 0.949 and 0.947, respectively, for the pure, Gd, Tb and Dy-doped $BiFeO_3$ nanoparticles. This shows that there is a decrease in tolerance factor upon doping of RE ions. Tolerance factor has been found to be less than unity; this indicating the tilting or rotation of distorted FeO_6 octahedral in $BiFeO_3$. The less than one value of tolerance factor in RE-doped synthesized nanoparticles signifies that the driving force for the octahedral rotation increases, upon doping, and the Fe–O and Bi^{3+}/RE^{3+}–O bonds are respectively, under compression and tension strain, thereby, resulting in the structural transformation from rhombohedral to orthorhombic [108-110].

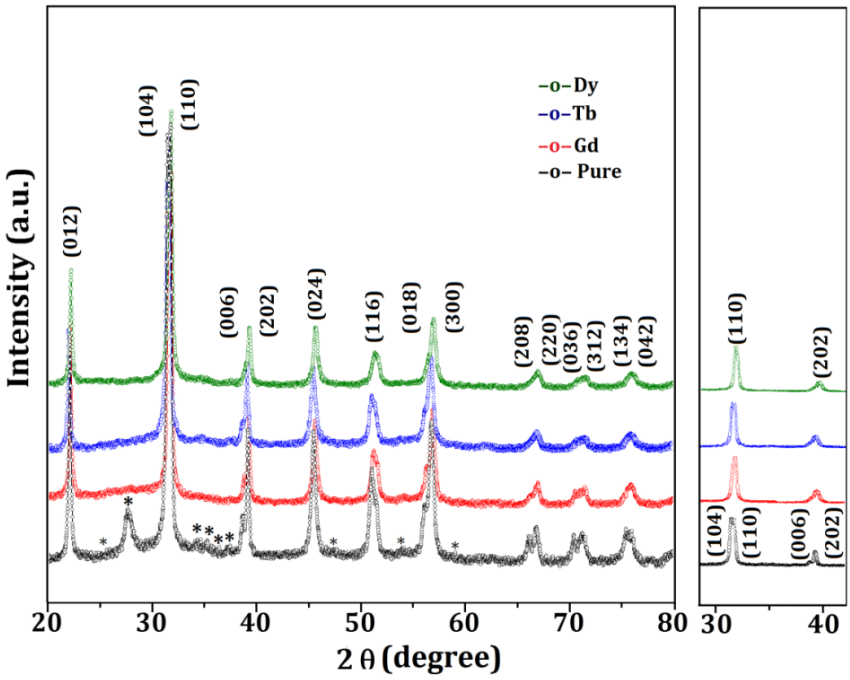

Figure 3.16XRD patterns of pure rare earth metal-doped $BiFeO_3$ nanoparticles. Insets show enlarged view of XRD patterns around 2θ ~ 31-32^o and 30-40^o

More importantly, in RE-doped $BiFeO_3$, the right-shifting of characteristic diffraction peaks towards higher 2θ has been observed. This is precisely due to smaller ionic radii of the RE (Gd^{3+} = 1.27Å; Tb^{3+} = 1.25Å; Dy^{3+} = 1.24Å) as compared to Bi^{3+} = 1.36Å [108-110], and thereby confirming the reduction of lattice parameters and overall unit cell volume. The above two factors validate the induced structural distortions in rhombohedral phase, making it unstable and consequently stabilizes the orthorhombic phase. Such transformations enhance the polarizability, magnetism and finally magnetoelectric coupling. The crystallite size of pure, Gd, Tb and Dy-doped $BiFeO_3$ has been calculated using Debye-Scherer formula and found to be 52, 56, 34 and 43 nm, respectively, corroborating with TEM.No secondary phase or impurity has been detected in RE-doped $BiFeO_3$ nanoparticles, suggesting that the substitution of RE for Bi^{3+} effectively supress the formation of impurity or secondary phase and thus the RE-dopant have entered into the crystal lattice.

Table 3.3 Particle size, tolerance factor, saturation magnetization, dielectric constant, magnetodielectric coefficient of pure and rare earth metal doped $BiFeO_3$ nanoparticles

S. No.	Sample description	Particle size (nm)	Tolerance factor	Saturation magnetization (emu/g)	Dielectric constant (At 100 Hz)	Magnetodielectric Coefficient (%) at 20 kOe
1.	Pure $BiFeO_3$	44	0.954	1.98	138	2.20
2.	15 % Gd	46	0.951	3.00	412	3.47
3.	15 % Tb	25	0.949	4.38	643	4.36
4.	15 % Dy	36	0.947	5.22	900	5.82

3.3.3.2 Magnetic analysis

In bulk $BiFeO_3$ particles, Fe^{3+} ions are ordered antiferromagnetically with G–type canted antiferromagnetic ordering, and their moment alignment constitutes incommensurate space modulated spiral spin structure with a long periodic wavelength of 62 nm resulting in non–zero magnetization with an antiferromagnetism in $BiFeO_3$ [15, 25, 111]. In the present case, as shown in Figure 3.17, the M-H hysteresis loops, at room temperature, reveal that all the synthesized

nanoparticles exhibit ferromagnetic character. The value of saturation magnetization has been found to be 1.98, 3.00, 4.38, 5.22 emu/g for, respectively, for pure, Gd, Tb and Dy-doped $BiFeO_3$ nanoparticles, clearly reflecting that doping of RE leads to higher value of saturation magnetization compared to its pure form (Table 3.3). The highest value of saturation magnetization, 5.22 emu/g, observed in the Dy-doped $BiFeO_3$ nanoparticles, may be due to the large magnetic moment and the smallest size of Dy^{3+} ions amongst the other rare earth ions (Gd, Tb).The observed magnetic behavior and high value of saturation magnetization, in synthesized nanoparticles, can be due to following reasons:

- Size effect: The size of the synthesized nanoparticles, 22- 46 nm, is less than spinspiral cycloid period (62 nm), leading to suppression of helical order, i.e., incomplete rotation of spins, and, thus, resulting in ferromagnetism [11, 15, 25, 40, 64-65, 85, 30, 106-108].

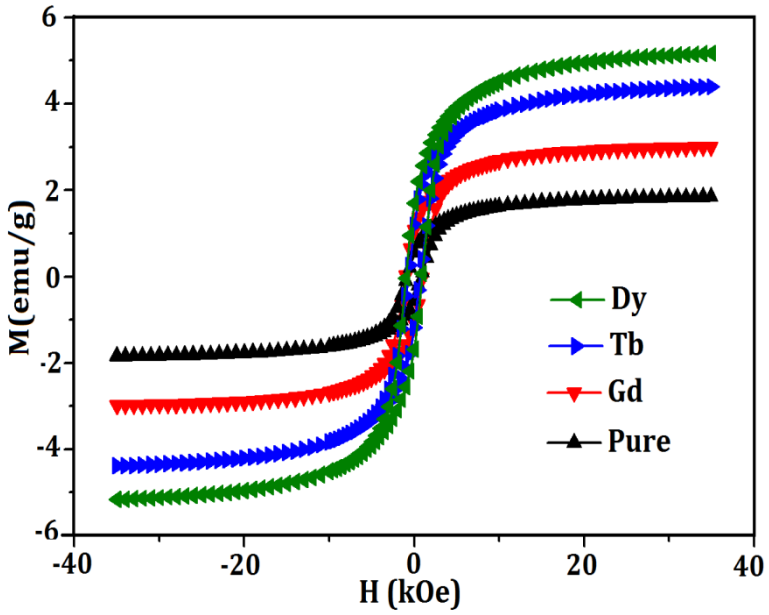

Figure 3.17: The magnetization versus applied magnetic field hysteresis loops of pure and 15 % rare earth metals (Gd, Tb, Dy)-doped $BiFeO_3$ nanoparticles

- Non-exact compensation of magnetic lattices: Bulk $BiFeO_3$ is antiferromagnetic. By reducing its size less than the cycloid period (62 nm), a net magnetic moment is induced due to non-exact compensation of two magnetic sub-lattices resulting in ferromagnetism [11, 98-99, 108].

- Spin-interaction: The spin-interaction between RE and Fe^{3+} ions may decouple the antiferromagnetic interactions between the Fe^{3+} ions, which may lead to ferromagnetism [109].
- Doping of magnetically active RE ions: The doping of magnetically active RE ions, having smaller ionic radii than Bi^{3+}, results in large structural distortions. The spin cycloids of RE ions get destroyed with structural transition leading to destruction of space modulated spin-spiral structure, and, thus results in ferromagnetism. More importantly, the first principle calculations also suggest that the effective magnetic moment of RE is large, and, on their substitution in $BiFeO_3$, there results a coupling between RE ions with Fe^{3+} leading to ferromagnetism [41, 64-65]. The substitutions of RE, also results in different bond interactions between 4f and 5d orbitals of RE-O and 6p orbitals of Bi-O leading to magnetic coupling, i.e., ferromagnetism.
- Lattice strain: Doping of RE ions would result in higher lattice strain as is clear from the calculated tolerance factors. This, in turn, results in the higher spin canting giving rise to ferromagnetism [104].
- Structural transition: Doping of rare earth ions results in structural transition from rhombohedral to orthorhombic and destroys the inhomogeneous spin structure and, therefore, the latent magnetization locked within the spin cycloid is released, subsequently leading to ferromagnetism [100].

Last, the possibility of the presence of Fe^{2+} ions cannot be ruled out, which may be responsible for the observed magnetic behavior [5, 40, 64-65].

3.3.3.3Dielectric analysis

The variation of relative dielectric constant (ε_r) of the synthesized nanoparticles as a function of frequency, at room temperature, is shown in Figure 3.18; which, at low frequencies, shows a monotonous decrease of dielectric constant with increase in frequency, but, at higher frequencies, a constant behaviour.Such a change in the dielectric constant, with frequency, indicates large dispersion due to Maxwell–Wagner [95, 110] type interfacial polarization in agreement with Koops phenomenological theory [111].

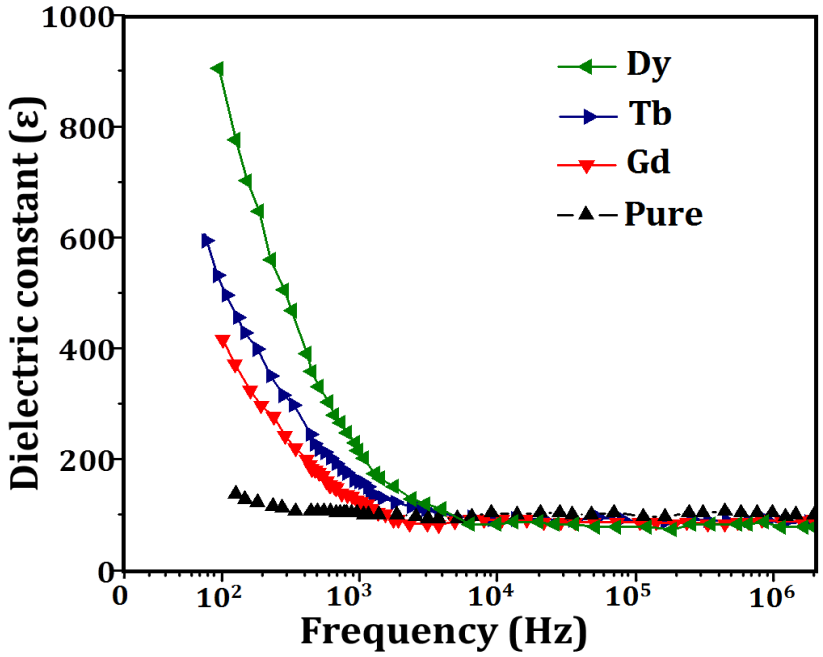

Figure 3.18 Dielectric traits of pure and rare earth metal-doped $BiFeO_3$ nanoparticles

The high values of dielectric constant observed at lower frequencies can be explained on the basis of space charge polarization due to inhomogeneous dielectric structure, where the space charges follow the frequency of applied electric field [112].At low frequency, the dielectric constant is dependent on different types of polarization mechanisms, viz., electronic, atomic, interfacial, and ionic. However at higher frequencies, it arises due to the contribution from electronic polarization. Dielectric constant at 100 Hz has been found to be 138, 412, 643, and 900 respectively, for pure, Gd, Tb and Dy-doped $BiFeO_3$ nanoparticles(Table 3.3).The observed high value of dielectric constant in RE-doped $BiFeO_3$ can be attributed to the following facts:

- Synthesized nanoparticles consist of large number of grain boundary regions, uncompensated surfaces with dangling bonds. The doping of RE ions leads to the inhomogeneity between the grain and grain boundary and reduces the moveable charges, thereby resulting high dielectric constant.
- The formation of large dipole moment may result due to structural transition from rhombohedral phase to orthorhombic, reduction of lattice parameters, and nano-size of the synthesized nanoparticles, which also leads to high dielectric constant [64-65].

The electronic, atomic, ionic as well as the dipolar (or oriental) and interfacial polarizations are the basic mechanisms responsible for the polarization of materials [113]. The observed trend in

dielectric constant can be attributed to dipolar, oriental and interfacial polarization. At lower frequencies (≤ 1 kHz), the migration of carriers stops due to their collection near the physical interface barrier; this produces localized polarization in the material. The dipoles, formed due to the charge defects, track the frequencies of applied field. However, in sub-infrared frequency range (~10^3–10^6 Hz), the dipolar polarization becomes effective, which finally gets saturated as the diploes are completely formed in this frequency range due to high applied field [64-65, 114].

3.3.3.4 Magnetoelectric coupling analysis

The change in dielectric constant on varying magnetic field is indirectly due to what we call the magnetoelectric coupling [34]. Figure 3.19 shows the observed magnetodielectric coupling coefficient (MD) in the synthesized nanoparticles at 10 kHz frequency. MD is defined as [64-65]:

$$\mathrm{MD} = \frac{\Delta\varepsilon_r}{\varepsilon_r(0)} = \frac{\varepsilon_r(\mathrm{H}) - \varepsilon_r(0)}{\varepsilon_r(0)}$$

where $\varepsilon_r(\mathrm{H})$ and $\varepsilon_r(0)$ are the dielectric constants at applied and zero magnetic field, and $\Delta\varepsilon_r$ is the change in dielectric constant with and without magnetic field. Figure 3.19 registers the pronounced effect of RE-doping and the size of the synthesized nanoparticles on the observed MD (Table 3.3). The MD coefficient increases with RE-doping at room temperature. A very high value of MD, around 5.82 %, has been observed for 15 % Dy-doped $BiFeO_3$ nanoparticles, which is almost four times higher than that for pure $BiFeO_3$. The smallest value of tolerance factor in the case of Dy-doped $BiFeO_3$ means large crystallographic distortion and high magnetic moment of Dy^{3+} ions, which may result in maximum MD. The non-linear trend in MD for pure and Gd-doped $BiFeO_3$ nanoparticles has been observed for all the values of applied magnetic field. But, however, for Tb- and Dy-doped $BiFeO_3$ nanoparticles, MD increases linearly up to 10 kOe, and afterwards, it acquires a steady state.

The observed trend in MD can be explained on the basis of the following facts: First, the nano-size of the synthesized particles (less than cycloid period (62 nm)) leads to suppression of helical order; this modifies the cycloidal spin structure of $BiFeO_3$, which may improve the magnetodielectric coupling [15, 25, 30, 104, 115-118]. Second, the structural transformation from rhombohedral to orthorhombic, due to RE ions doping, results in interactions between the ferroelectric and ferromagnetic domains, which is likely to improve MD. The doping of RE ions

also leads to the reduction in lattice parameters as well as overall unit cell volume, which may further improve MD [64-65]. The observed magnetodielectric coupling can also be described using magneto-capacitance. However, Catalan reported the change in dielectric constant, under the applied magnetic field, an indirect evidence of magnetoelectric coupling, which may also be observed due to combination of magneto-resistance and Maxwell-Wagner effect [119].

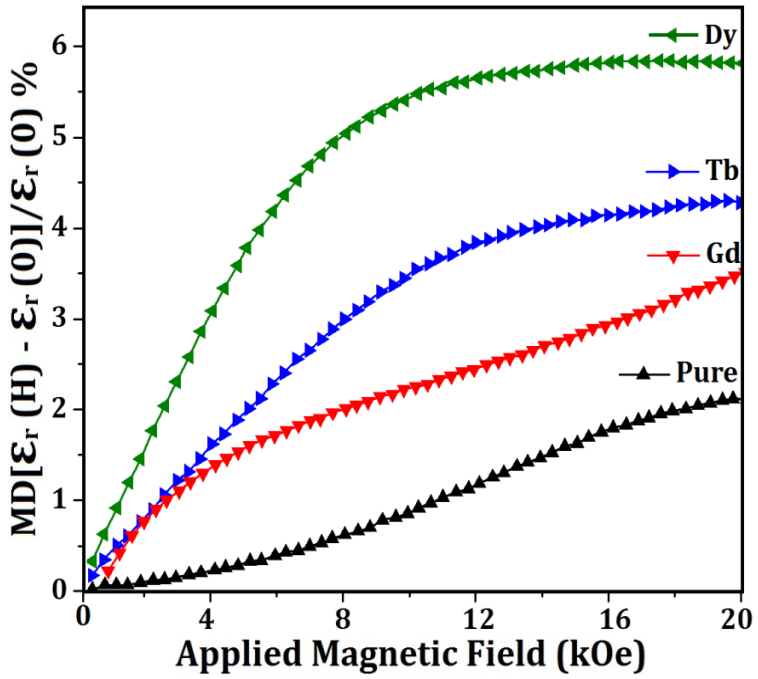

Figure 3.19 Magneto-dielectric coupling in pure and rare earth metal-doped $BiFeO_3$ nanoparticles

Chapter 4

Multiferroism in rare earth metal doped $BiFeO_3$ nanowires

Overview

This chapter deals with the study of magnetoelectric coupling in pure and rare earth metal ions (Gd^{3+}, Tb^{3+}, Dy^{3+})-doped $BiFeO_3$ nanowires synthesized by colloidal dispersion template-assisted technique. The effects of doping of rare earth metal ions as well as the nanosize of the synthesized nanowires on structural, magnetic, electric, dielectric and magneto-dielectric/electric coupling have been investigated. For the comparative study, nanowires of size, 100 nm (bulk in present case) and 20 nm, have been synthesized. Doping of the rare earth metal ions, in $BiFeO_3$ nanowires, results in structural transformation from rhombohedral to orthorhombic phase. Magnetic study confirms that the bulk nanowires possess antiferromagnetic behaviour. The reduction in the size of nanowires from 100 nm to 20 nm, and, at the same time, doping of rare earth metal ions, results in ferromagnetism in the synthesized nanowires. The dielectric measurements also show that doping results in high dielectric constant as compared to that of the pure $BiFeO_3$. To check the magnetoelectric coupling in the synthesized nanowires, magnetodielectric and magnetoelectric coupling coefficients have been measured.

A part of this chapter has been published in the form of following research papers:

1. *Gurmeet Singh Lotey, NK Verma, Magnetoelectric coupling in multiferroic BiFeO3 nanowires, Chemical Physics Letters, 579 (2013) 78-84 (Elsevier).*
2. *Gurmeet Singh Lotey, NK Verma, Phase-dependent multiferroism in Dy-doped BiFeO3 nanowires, Superlattices and Microstructures, 53 (2013) 184–194 (Elsevier).*
3. *Gurmeet Singh Lotey, NK Verma, Multiferroic properties of Tb-doped BiFeO3 nanowires, Journal of Nanoparticles Research, 15 (2013)1553 (Springer).*
4. *Gurmeet Singh Lotey, NK Verma Multiferrosim in rare earth metals-doped BiFeO3 nanowires, Superlattices and Microstructures,60 (2013) 60-66 (Elsevier).*

4.1 Magnetoelectric coupling in multiferroic $BiFeO_3$ nanowires

This section deals with the systematic study of magnetoelectric coupling in multiferroic $BiFeO_3$ nanowires, synthesized by colloidal dispersion template-assisted technique of size 20 nm, as explained in chapter 2. The synthesized nanowires possess rhombohedral structure (R3*c* space group). Magnetic and electrical measurements reveal their ferromagnetic and ferroelectric behaviour and show high saturation magnetization and polarization, 3.82 emu/g and 54 $\mu C/cm^2$, respectively, with small leakage-current. Room temperature magnetoelectric longitude (L-α_{ME}) and transverse (T-α_{ME}) coupling coefficients have been found to be, respectively, 10.738 and 6.866 mV/cmOe using dynamic lock-in technique (explained in chapter 2). The observed magnetoelectric coupling properties have been explained on the basis of their nano-size, phase purity and defect free nature [79].

4.1.1 Results and discussion

4.1.1.1 Morphological, crystallographic and elemental compositional analyses

Figure 4.1 shows SEM micrograph of the synthesized nanowires revealing their dense and uniform growth as well as they are found to be homogeneous, parallel, and well aligned. The diameter of $BiFeO_3$ nanowires has been found to be around 20 nm.

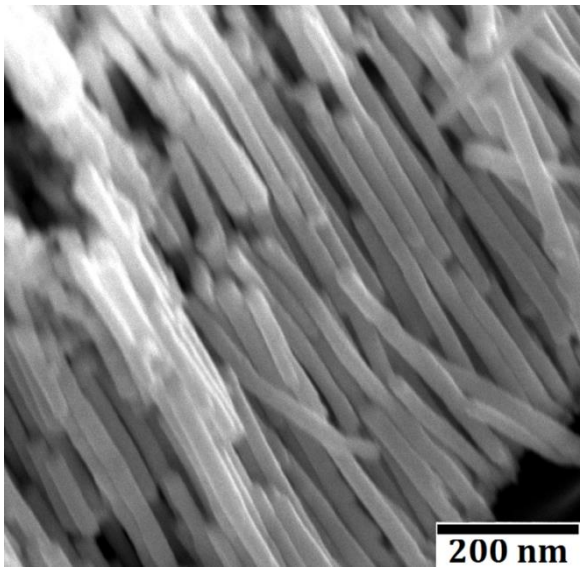

Figure 4.1 SEM micrograph of $BiFeO_3$ nanowires

To determine the structural features of $BiFeO_3$ nanowires, Rietveld refinement of XRD patterns have been performed using the FullProf program.The observed, calculated, and the different refined x-ray diffraction (XRD) patterns of the synthesized nanowires are shown in Figure 4.2.

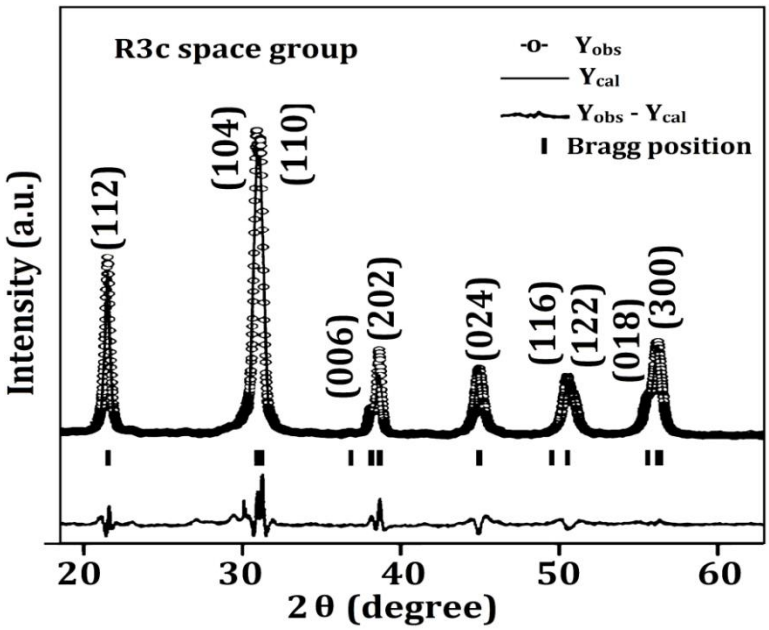

Figure 4.2 Rietveld refined XRD patterns of $BiFeO_3$ nanowires

Table 4.1 Rietveld structural refinement parameters of $BiFeO_3$ nanowires

Lattice parameters (Å)			Atom coordinates x	y	z	Bond length (Å)		Bond angle		R-factors	Microstrain
a = 5.568	Bi	6a	0	0	0	Bi-O	2.21	Fe-O-Fe	154.15°	R_{wp} = 7.89	0.034
c = 13.512	Fe	6a	0	0	0.2316	Fe-O	1.812	O-Bi-O	79.06°	R_F = 4.81	
	O	18b	0.4721	0.0197	-0.0734	Fe-O	2.251			R_B = 8.75	

It has been found that the XRD patterns of synthesized $BiFeO_3$ nanowires embedded in AAO matrix are in well agreement with hexagonal phase of rhombohedral structure with R3*c* space group (JCPDS file no. 86–1518). The lattice parameters, bond angle, bond length, R-factors and microstrain of the nanowires have been calculated, and are shown in Table 4.1. The microstrain has been found to be 0.034. No additional peaks related to any impurity or other phases have been detected in XRD patterns, revealing their defect-free nature without the formation of any

secondary phase. The high intense peaks of XRD patterns demonstrate the high crystalline nature of nanowires. No peak related to anodic alumina oxide (AAO) Al_2O_3 template has been seen in XRD patterns because of their amorphous nature. To check the phase purity, and oxidation state of Fe in $BiFeO_3$, enlarged view of XPS spectrum in the range of 705 to 725 eV has been carefully examined, as shown in Figure 4.3 (a). The background correction has been done using Shirley background subtraction - non-linear least square fitting, and using mixed Gauss-Lorentz function.

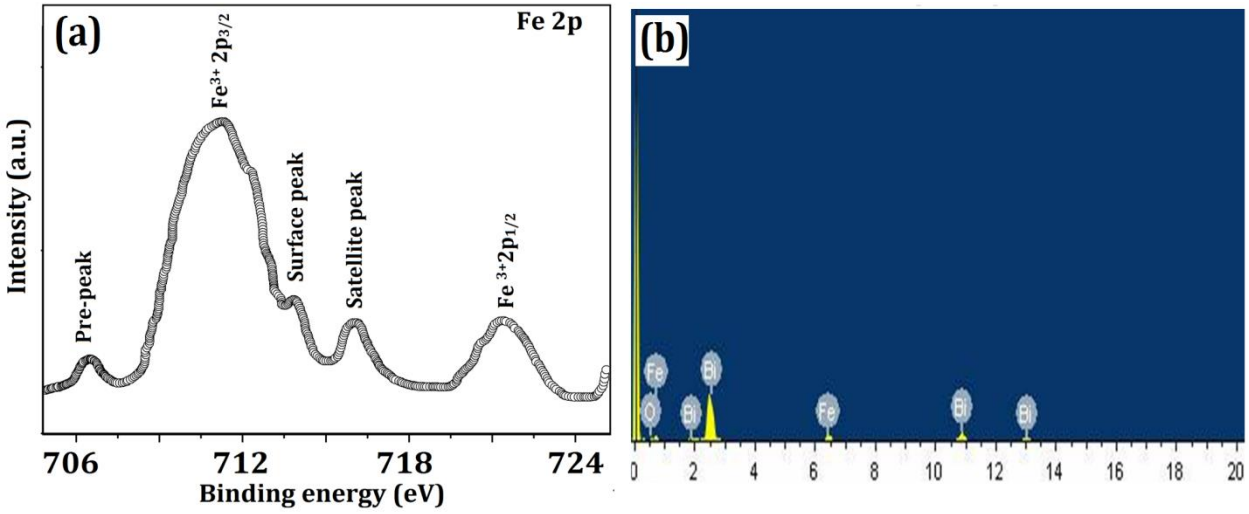

Figure 4.3 (a) Enlarge view of x-ray photoemission spectra of Fe 2p and (b) EDAX spectrum of $BiFeO_3$ nanowires

There are two main photo emission peaks positioned around 711 and 721.7eV assigned to Fe^{3+}. These represent the spin orbit doublet, $2p_{3/2}$ and $2p_{1/2}$ of Fe^{3+} and affirm the 3+ oxidation state of Fe. No peak corresponding 2+ oxidation state of Fe or any other impurity phase has been observed in the XPS spectrum; this endorses the dominant role of Fe^{3+} ions for the observed ferromagnetism (to be discussed in magnetic analysis ahead).Three additional peaks around 706.5, 713.7 and 716 eV have been also seen; these are known as pre-peak, surface peak and satellite peak, respectively [64-65]. The surface peak is related to decrease in co-ordination number of Fe^{3+} ions located at the surface of the nanowires. The satellite peak is associated with shake-up process. Figure 4.3 (b) shows the EDAX spectrum of $BiFeO_3$ nanowires revealing the

presence of Bi, Fe and O. No peak related to any other element or oxide has been observed in EDAX spectrum, which confirms the highly pure nature of $BiFeO_3$ nanowires.

4.1.1.2 Magnetic analysis

The magnetization versus applied magnetic field (M-H) hysteresis loop of synthesized $BiFeO_3$ nanowires at room temperature is shown in Figure 4.4 (a); this indicates that the synthesized nanowires exhibit ferromagnetic behavior with high saturation magnetization, 3.82 emu/g. Similar results of magnetic behavior has been also presented for ultrafine fibers and nanowires of $BiFeO_3$ [64-65, 116].

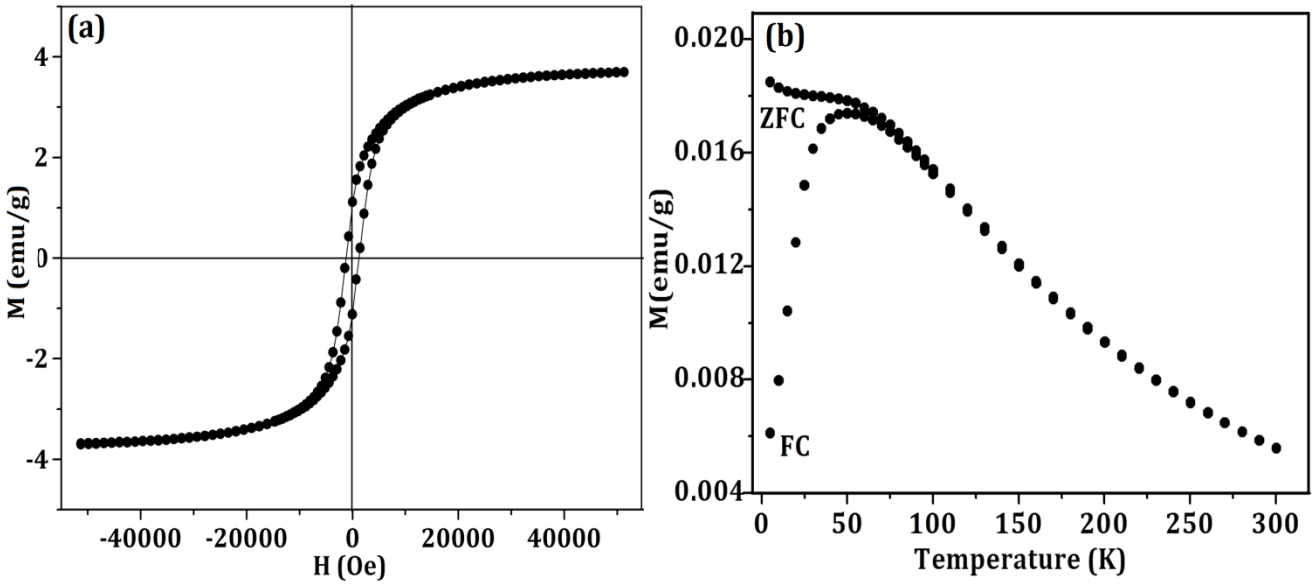

Figure 4.4 (a) Magnetization versus applied field (MH) hysteresis loop and (b) temperature dependence of magnetization of $BiFeO_3$ nanowires

The XRD, EDAX and XPS analyses rule out the presence of any impurity or secondary phase or Fe^{2+} ions; these confirm that the observed ferromagnetic behavior is not associated with the presence of ferromagnetic Fe^{2+} ions or any other impurity phases in the nanowires. The observed magnetic behavior can be described on the basis of following facts: First, bulk $BiFeO_3$ (having size > 62nm) is antiferromagnetic, and possesses spin-spiral incommensurate structure with long range cycloidal period of 62 nm. The antiferromagnetic axis rotates through the crystal with an

incommensurate long-wavelength period of 62 nm, which cancels the macroscopic magnetization, results in anti-ferromagnetism with unsaturated magnetization. However, in the present study, the size of the synthesized nanowires is 20 nm, which is less than the cycloidal period of 62 nm; this destroys the cycloidal structure and, thus, leads to ferromagnetic ordering, as depicted in Figure 4.4 (a) [3, 25, 50, 64-65, 85, 117, 118]. Second, the synthesized nanowires possess large surface-to-volume ratio because of their smaller size, which enhances the overall magnetization of nanowires due to uncompensated spins at the surface of $BiFeO_3$ nanowires, and, results in net magnetic moment produced due to non-exact compensation of the two magnetic sub-lattices [3, 25, 64-65, 98-99, 108]. There are surface imperfections, and surface strain anisotropies dominate magnetic properties of nanoparticles [25, 64-65]. The increase of magnetization in the synthesized nanowires may be due to the contribution of strain anisotropies, and non-collinear magnetic ordering. Third, the MH hysteresis loop is found to be symmetric on both sides of the axis, which establishes that the exchange interactions are not responsible for the magnetic behavior of nanowires [3, 64-65]. Lastly, the synthesized nanowires have been found (Table 4.1) to possess high microstrain, 0.034; this may result in higher spin canting, and give rise to ferromagnetism [101]. Temperature-dependent magnetic study (zero field cooling (ZFC) and field cooling (FC) curves) have been employed to check the existence of inter-nanowire interactions. For the ZFC magnetization measurements, the sample is first cooled from room temperature to 5 K in zero field, and 1000 Oe magnetic field is applied, and, then the magnetization has been measured in the warming cycle with applied field. To perform FC magnetization measurements, the sample is first cooled in the applied magnetic field of 1000 Oe to 5 K, and, the FC magnetization, measured in the warming cycle under the same field (Figure 4.4 (b)). The broad peak has been observed in ZFC and FC curves at lower temperature due to nano-size as shown in Figure 4.4 (b). No such peaks are presented in bulk $BiFeO_3$ having particle size higher than that of the critical spin spiral cycloidal period of 62 nm [85]. Due to nano-size of synthesized nanowires, Fe^{3+} spins orient towards the direction of applied magnetic field, thereby breaking the antiferromagnetic spiral ordering. The splitting between ZFC and FC curves around 80K has taken place. This indicates the spin-glass transition temperature of the synthesized nanowires, representing their spin-glass behavior [85].This can be attributed to the nano-size effect, inter-nanowire interactions, random distribution of anisotropy axes, microstrain as well as the high packing volume fraction with complex interplay between finite size effects in the

synthesized nanowires [25, 61-64, 80-81, 101, 108, 116, 118, 120-129]. Liu [124]reported spin-glass transition temperature, 55K in hydrothermally synthesized $BiFeO_3$ nanowires that is smaller than as observed in the nanowires (80 K).

4.1.1.3 Electrical analysis

4.1.1.3.1 Ferroelectric study

Figure 4.5 (a) shows polarization as a function of applied electric field, about 600 kV/cm with frequency (ν) = 10 kHz (PE), hysteresis loop of $BiFeO_3$ nanowires at room temperature. The observed well-saturated rectangular like PE loop may be due to the presence of less oxygen-related defects, and phase purity of the nanowires. The high value of saturation polarization, around 54 μC/cm^2, has been observed at 535 kV/cm applied electric field.

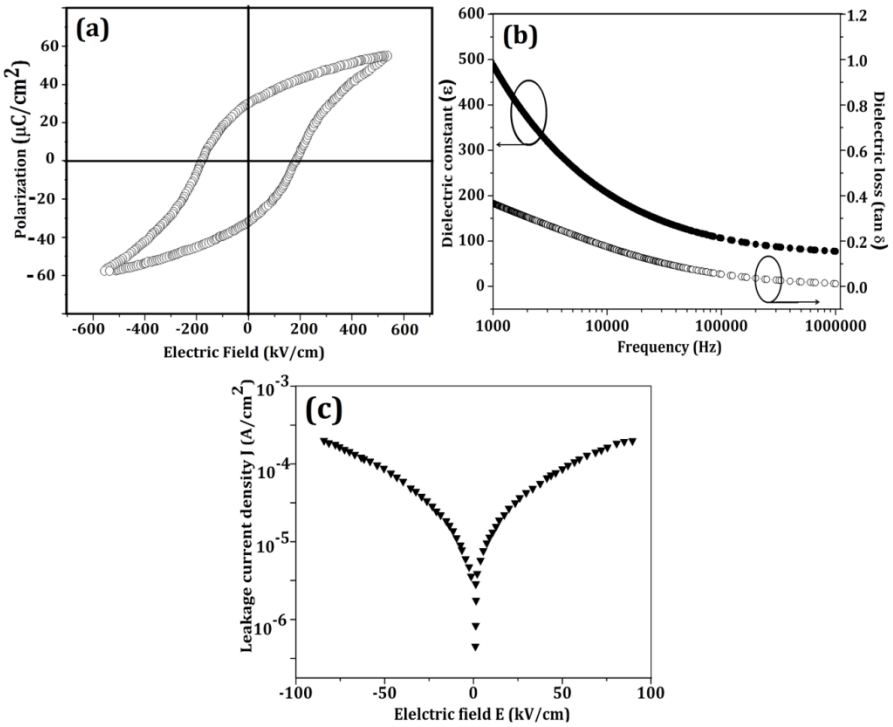

Figure 4.5 (a) Polarization versus electric field hysteresis loop and (b) relative dielectric constant and dielectric loss vs. frequency traits of $BiFeO_3$ nanowires (c) leakage-current density versus applied electric field traits of $BiFeO_3$ nanowires

The smaller leakage current (to be discussed later) may result due to the absence of secondary phases or impurity (corroborating with XRD, EDAX and XPS analyses); this, consequently improves the domain pinning effects and the spontaneous polarization [3, 64-65]. More importantly, the average grain size of the synthesized nanowires is small, which may result in lower space charge density, smaller leakage current density, and consequently resulting in spontaneous polarization.

4.1.1.3.2 Dielectric study

The variation of relative dielectric constant (ε) of the $BiFeO_3$ nanowires as a function of frequency has been shown in Figure 4.5 (b). A monotonous decrease of dielectric constant, and decease in dielectric loss has been registered with increase in frequency. The observed trend in dielectric constant and dielectric loss with frequency indicates large dispersion due to Maxwell–Wagner [110] type interfacial polarization, and is in good agreement with Koops phenomenological theory [111]. The high value of dielectric constant, 492, at 1000 Hz is due to space charge polarization resulting from the inhomogeneous dielectric structure. In our earlier reports [64-65] low value of dielectric constant, as compared to present case, is observed, which may be due to the presence of defects and secondary phases in undoped $BiFeO_3$ nanowires. Zhang [130] reported dielectric constant around 90 at 100 kHz in $BiFeO_3$ nanotubes. At low frequency, the dielectric constant has been found to be dependent on different types of polarization mechanisms such as electronic, atomic, interfacial and ionic whereas at higher frequencies, it arises due to electronic polarization. Synthesized polycrystalline nanowires consist of large number of grain boundary regions, uncompensated surfaces with dangling bonds; this influences the dielectric properties. The observed trend in dielectric constant can be explained on the basis of dipolar, oriental and interfacial polarization. It has been observed that at lower frequency (≤ 1 kHz), the migration of carriers stops due to their collection near the physical interface barrier, thereby producing localized polarization in the material; here, the dipoles track the frequencies of applied field. But in higher frequency range (~10^3–10^6 Hz), the dipolar polarization becomes effective, and finally gets saturated, as the diploes are completely formed due to high applied field [64-65,114].

4.1.1.3.3 Leakage current density versus applied electric field (J-E) characteristics

Leakage current density versus applied electric field (J-E) of the nanowires embedded in AAO templates have been studied to know the leakage current phenomenon associated with the $BiFeO_3$. Figure 4.5 (c) displays J-E curve of the synthesized nanowires, revealing their excellent symmetry under positive and negative applied electric fields. The very small leakage current has been observed in the synthesized nanowires as compared to earlier reports [64-65,117,128] attributed to small defects, high crystallinity, absence of impurity or secondary phases, nano-sized and small grain boundaries in the synthesized nanowires.

4.1.1.4 Magnetoelectric coupling analysis

Figure 4.6 shows longitude (L-α_{ME}) and transverse (T-α_{ME}) magnetoelectric coupling coefficients of synthesized $BiFeO_3$ nanowires measured at room temperature. The magnetoelectric coefficient versus DC bias magnetic field reveals the hysteretic behavior of the nanowires as depicted in the magnetic field cycles shown in Figure 4.6. It has been found that both L-α_{ME}, and T-α_{ME} increase quickly with increase in the bias magnetic field, and, attain maximum value, L-αME = 10.738 mV/cmOe and T-αME = 6.866 mV/cmOe, respectively, at 0.5 and 0.3 kOe. This shows that the longitudinal magnetoelectric coupling coefficient exceeds the transverse magnetoelectric coupling coefficient.

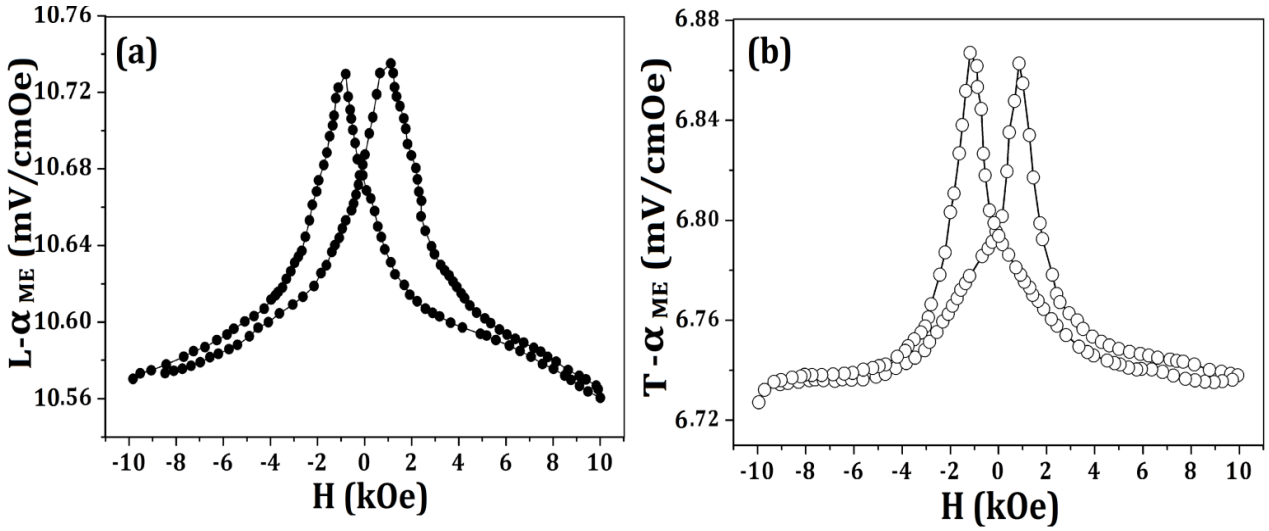

Figure 4.6 Room temperature DC bias magnetic field dependence (a) longitudinal (L-α_{ME}) and (b) transverse (T-α_{ME}) magnetodielectric coupling coefficients of $BiFeO_3$ nanowires

The observed values of L-α_{ME}, and T-α_{ME} are around 17 and 24 times higher than as reported by Naik [81] for bulk, and, one order higher as reported by Caicedo [82]for thin film.The smaller magnetoelectric coupling coefficients observed in bulk and thin films, may be due to the presence of impurity or secondary phases, large grain size and charge imbalance of Fe, i.e.$Fe^{2+}\leftrightarrow Fe^{3+}$[81-82]. The wide-range scattering in the magnetoelectric coefficients has been noticed, and attributed to the nano-size of the synthesized $BiFeO_3$ nanowires. Bulk $BiFeO_3$ has long range cycloidal period of 62 nm, and, is antiferromagnetic with Néel temperature 370^oC [40, 50, 118]. However, in the present case, the size of the synthesized nanowires, 20 nm, being less than the cycloidal period, the antiferromagnetic ordering gets destroyed; it is reflected from the magnetic properties of the synthesized nanowires possessing ferromagnetism. This modifies the domain structure, and, thereby leading to high magnetoelectric coupling [25, 81, 131]. Therefore, the enhancement in magnetoelectric coupling coefficient in the synthesized nanowires can be attributed to their nano-size, and high microstrain. The nano-size of synthesized nanowires enhances the magnetic ordering, which strengthens the sub-lattice interactions, and thereby results in the ME [64-65]. The synthesized nanowires have been found (Table 4.1) to possess high microstrain, 0.034; this may result in higher spin canting, and give rise to ferromagnetism [101]. The contribution of magneto-resistance, and Maxwell–Wagner effect for the observed ME cannot be ignored [40, 119]. The observed intrinsic ME coupling may also be due to magnetostriction effect. The change in lattice parameters occurs with the application of magnetic field. This generates strain in the nanowires due to coupling between ferroics domains, and, induces stress in it, which, in turn, induces an electric field in the nanowires that orients the ferroelectric domains, and, subsequently leads to observed ME. Room temperature occurrence of ferromagnetism and ferroelectricity (Figure 4.4 and 4.5) further supports the observation of multiferrosim and magnetoelectric coupling in the $BiFeO_3$ nanowires.

4.2 Multiferroic properties of Tb-doped $BiFeO_3$ nanowires

In this section multiferroic property of Tb-doped $BiFeO_3$ nanowires have been presented. Bulk nanowires (having diameter 100 nm), pure and Tb-doped $BiFeO_3$ multiferroic nanowires (diameter - 20 nm) have been synthesized by colloidal dispersion template-assisted technique, as explained in chapter 2. The effect of Tb-doping and size of synthesized nanowires on structural, electrical, magnetic, dielectric and magnetodielectric properties have been investigated. X-ray

diffraction (XRD) study reveals that doping of Tb in $BiFeO_3$ nanowires leads to structural transformation from rhombohedral to orthorhombic. X-ray photoemission (XPS) analysis confirms the +3 oxidation state of Fe (Fe^{3+}) and, high purity of samples. Bulk nanowires exhibit antiferromagnetic characteristics whereas the Tb-doped $BiFeO_3$ nanowires show ferromagnetic character. Moreover, with increase in Tb concentration, the saturation magnetization increases. Temperature dependent magnetization study suggests their size-dependent ferro and ferri-magnetic behaviour. Polarization versus electric field (P-E) study reveals that pure $BiFeO_3$ nanowires possess elliptical loop, however doping of Tb results in rectangular loop - a portentous good ferroelectric properties. All synthesized samples exhibit frequency dependent dielectric constant, which decreases with increase in frequency and remains fairly constant at higher frequencies. Leakage current density decreases with increase in Tb concentration, and has been found to be three orders of magnitude less than those of bulk $BiFeO_3$ nanowires. The magnetoelectric coupling (ME) in synthesized nanowires was estimated by measuring magnetodielectric. A very high value of ME, 7.2 %, has been found for 15 % Tb-doped BiFeO3 nanowires [65].

4.2.1 Results and discussion

4.2.1.1 Morphological analysis

Figure 4.7 (a) to 4.7 (e) show cross-sectional view of the SEM micrographs for the bulk nanowires, pure and Tb-doped $BiFeO_3$ nanowires and their dense growth. They are found to be uniformly dense, homogeneous, parallel, and well aligned. Diameter of bulk nanowires has been found to be 100 nm (Figure 4.7 (a)), and, those pure, and Tb-doped $BiFeO_3$ nanowires, 20 nm (Figure 4.7 (b) to 4.7 (c)), respectively. Further, the TEM image (Figure 4.7 (f)) also confirms the diameter of pure $BiFeO_3$ nanowires to be 20 nm, which is consistent with SEM results. Figure 4.7(f) (inset) shows selected area electron diffraction (SAED patterns) rings of pure $BiFeO_3$ nanowires attributed to polycrystalline nature of synthesized nanowires. The d-spacing corresponding to the well-defined diffraction rings of the SAED patterns are in good agreement with the rhombohedral phase of $BiFeO_3$ nanowires, and assigned as (110), (202), (024), (116), (018), (208) in their respective SAED patterns. These results are in good accordance with those of the previous XRD studies.

4.2.1.2 Structural and phase analysis

Figure 4.8 shows the x-ray diffraction (XRD) patterns of bulk nanowires, pure and Tb-doped $BiFeO_3$ nanowires embedded in AAO matrix. It is clear from the XRD patterns of bulk, and pure $BiFeO_3$ nanowires, that these two possess hexagonal phase with rhombohedral structure (JCPDS file no. 86–1,518). Some additional peaks indicated by "*" associated with secondary impurities, have been detected in the bulk $BiFeO_3$ nanowires. No such peaks related to secondary impurities have been observed in pure and Tb-doped $BiFeO_3$ nanowires. However, it is clear from Figure 4.8 (b) that in case of Tb-doped $BiFeO_3$ nanowires, the splitting of peaks indexed as (104) , (110) and (006), (202) for 2θ values positioned around 32^o and 39^o,respectively , decrease upon Tb-doping, and these peaks finally get merged to a single peak at 15 % Tb concentration.

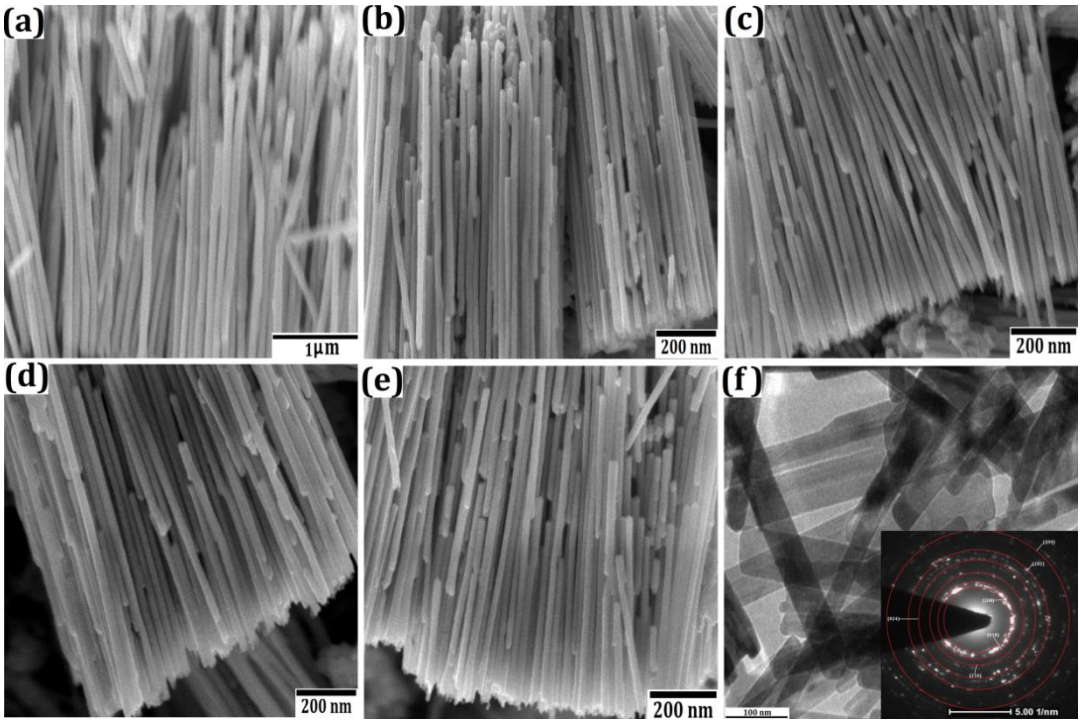

Figure 4.7 SEM micrographs of (a) 100 nm (bulk) (b) pure (c) 5% (d) 10% and (e) 15% Tb-doped nanowires (f) TEM image of pure $BiFeO_3$ nanowires and inset shows SAED of pure $BiFeO_3$ nanowires

This indicates the reduction of the rhombohedral phase (R3*c*), and increase of orthorhombic phase ($Pn2_1a$) with increase in Tb-doping in $BiFeO_3$. Therefore, it is established that the

complete structural transformation from rhombohedral to orthorhombic takes place at 15% Tb-doping concentration in the host $BiFeO_3$. Similar phenomenon of phase transformation with addition of rare earth metal ions in $BiFeO_3$ host material has been observed by the other groups [61, 62, 64, 66, 83-84]. Hume - Rothery rules [132] describe the solubility limit (or structural transformation) of dopants in host materials. It depends upon various factors such as atomic radii, crystal structures, valency, and electronegativity of the dopants. Therefore, depending upon these parameters solubility limit or structural transformation concentration of the rare earth metal ions varies from one dopant to another in the host materials. In the present case, solubility limit of Tb has been found to be 15%. However, in our previous reports, the solubility limit has been 10% and 15%, respectively, for Gd and Dy doped-$BiFeO_3$ nanostructures [3, 62, 64, 66].

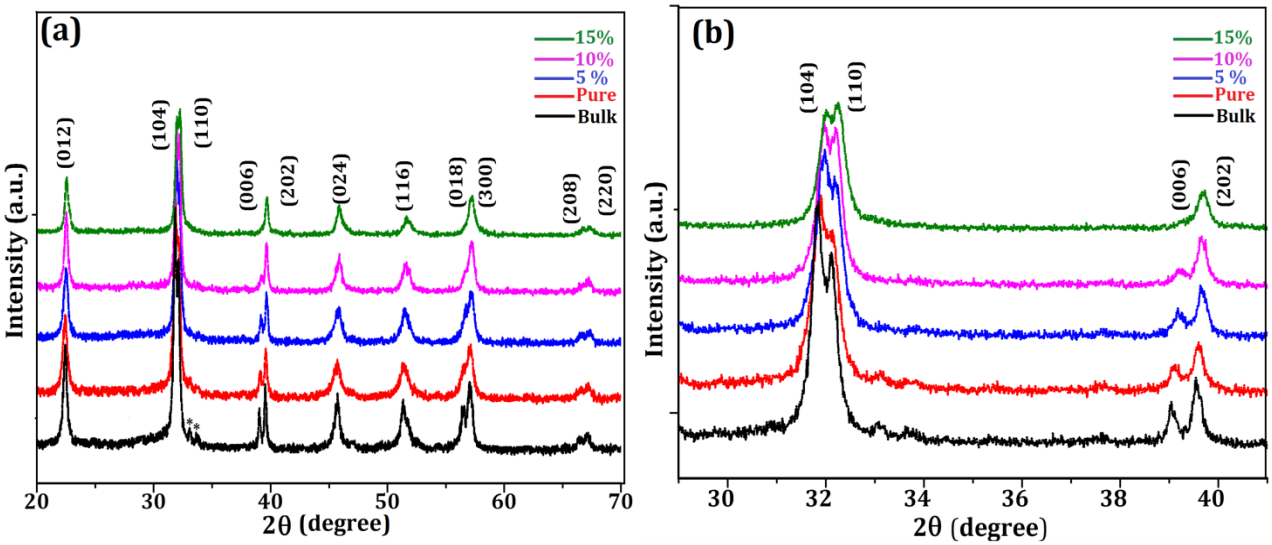

Figure 4.8 (a) X-ray diffraction patterns of bulk, pure and Tb-doped $BiFeO_3$ nanowires (b) Magnified XRD patterns of (104), (110) and (006), (202) reflections at $2\theta \sim 32^o$ and 39^o

This structural transformation might be significant for the ferroelectric as well as dielectric properties of the synthesized nanowires. Moreover, no additional peaks related to Tb or its any compound, has been observed in XRD patterns (Figure 4.8 (a)). It demonstrates the good dispersivity, and incorporation of Tb dopant in the host material. No peak related to anodic alumina oxide (AAO) Al_2O_3 template has been observed in XRD patterns because of their amorphous nature.

4.2.1.3 XPS analysis

Phase purification, chemical bonding and oxidation states of Bi, Fe, O and Tb analyses by x-ray photoelectron spectroscopy (XPS) through wide range of spectrum, from 0 to 1,000 eV of 15% Tb-doped $BiFeO_3$ nanowires, are shown in Figure 4.9.The two peaks (Figure 4.9 (a)) observed at positions, respectively, 158 and 164 eV corresponding to Bi $4f_{7/2}$ and Bi $4f_{5/2}$ confirm the trivalent oxidation state of Bi, i.e., Bi^{3+} in 15 % Tb-doped $BiFeO_3$ nanowires. To plaid the oxidation state of Fe in 15 % Tb-doped $BiFeO_3$ nanowires, the magnified XPS spectrum in range of 705 to 730 eV has been investigated as shown in Figure 4.9 (b).

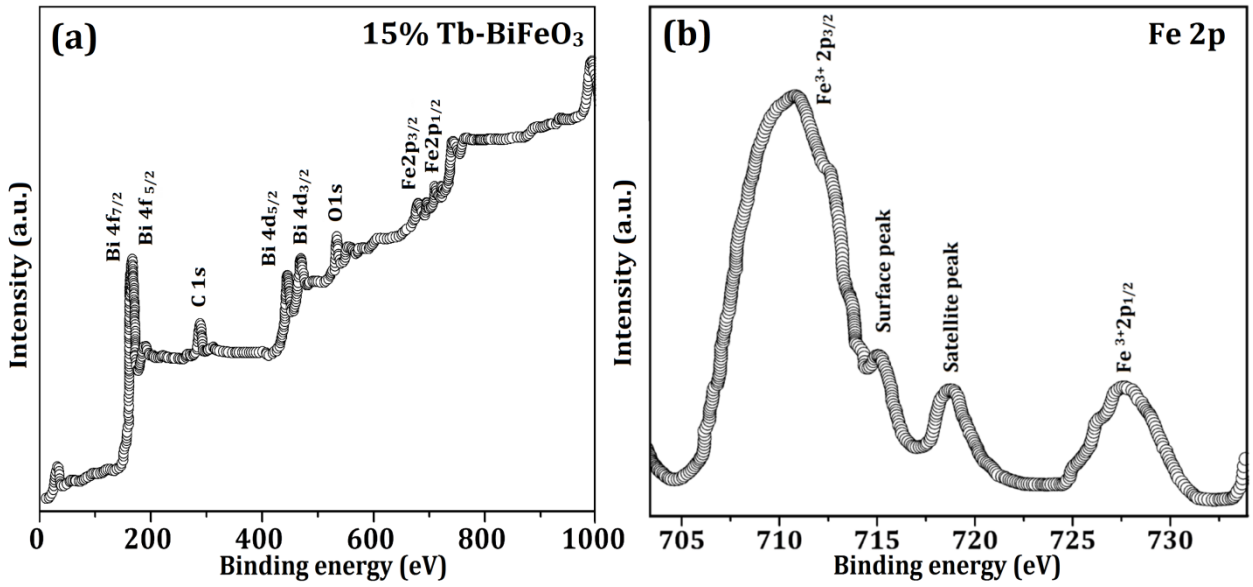

Figure 4.9 XPS wide range spectrum analysis of (a) 15 % Tb-doped $BiFeO_3$ nanowires and (b) Fe 2p

The background correction and oxidation state of Fe in $BiFeO_3$ have been carried out using Shirley background subtraction by non-linear least square fitting using mixed Gauss-Lorentz function. It is clear from the Figure 4.9 (b) that two main photo emission peaks positioned at 711.2 and 723.7eV are the spin orbit doublet $2p_{3/2}$ and $2p_{1/2}$ of Fe^{3+} oxidation state. These confirm the 3+ oxidation state of Fe in synthesized nanowires.

Apart from these peaks, two other additional peaks, positioned around 715 and 717 eV called, respectively, the surface peak and the satellite peak, have also been observed. Surface peak observed at 715 eV is because of the decrease of co-ordination number of Fe^{3+}cations located at

the surface of nanowires with Tb doping. The satellite peak around 717 eV has been observed because of the shake-up process. In this process, when the ejection of photoelectrons from 2p shell takes place, a small amount of kinetic energy of photoelectrons is lost on lifting the electron from 3d orbital to empty 4s orbital, and as a result, a peak related to energy loss has been observed. No extra peak corresponding to Fe^{2+} oxidation has been observed in the XPS spectra; it indicates the dominant role of Fe^{3+} ion, for observed ferromagnetism in pure, and Tb-doped $BiFeO_3$ nanowires (to be discussed in magnetic analysis ahead (Figure 4.10)). The peak positioned at 530.8 eV is attributed to O^{2-} oxidation state in $BiFeO_3$ lattice. It is clear from Figure 4.9 (a) that no additional peaks related to Tb in metallic or oxide form such as Tb and Tb_2O_3 or Tb_2O_3 have been observed in the XPS spectra, despite the Tb concentration being increased up to 15% in the $BiFeO_3$ host. This reveals that the Tb is likely to play the role of Bi, which is also confirmed by the XRD measurement. The peak observed at 285 eV is due to the small amount of adsorbed carbon that was used to calibrate the acquired spectrum. In addition to this, no extra peaks of any impurities or secondary phase, observed in the XPS spectrum, confirm the high purity of samples.

4.2.1.4 Magnetic analysis

The magnetization versus applied magnetic field (M-H) loops, of all the samples (except bulk nanowires) measured at room temperature (Figure 4.10), and indicating the saturation magnetization (Ms), achieved within the applied field of 50 kOe, reveal their typical ferromagnetic character. However, the bulk $BiFeO_3$ nanowires show antiferromagnetic behaviour. The G-type antiferromagnetic spin structure of $BiFeO_3$ leads to cooperative magnetism in $BiFeO_3$; it originates from the half-filled and localized ($t^2_{2g}e^2_g$) Fe^{3+} ions. The Fe^{3+} ions, in the high spin state, prefer to form the G-type antiferromagnetic ordering as the Pauli Exclusion Principle allows the transfer of electron to the neighbouring ion in an antiparallel direction only. Moreover, Figure 4.11 (a) shows that there is a shift in hysteresis loops towards positive axis due to exchange interaction; it results in its antiferromagnetic character. The XPS study rules out the presence of Fe^{2+} ions or any other impurity in 15 % Tb-doped $BiFeO_3$. It confirms that the observed ferromagnetic character is not because of the presence of these ions or any other impurity phases in the nanowires. The observed ferromagnetic behaviour in pure and Tb-doped $BiFeO_3$ nanowires could be ascribed due to following reasons:

- Doping of magnetically active Tb^{3+} ions, having radius smaller than that of the Bi^{3+} ion, result in larger distortion in lattice structure, thereby leading to suppression of spiral spin modulation in $BiFeO_3$; this is precisely because the spin cycloid of Tb^{3+}, which got destroyed on the structural transformation of the rhombohedral to orthorhombic (already observed in the XRD study).
- Decrease in the particle size of $BiFeO_3$ (antiferromagnetic system) results in the net magnetic moment produced due to non-exact compensation of the two magnetic sub-lattices. This non-compensation at the surface of the $BiFeO_3$ nanowires may be a primary cause for the observed ferromagnetism

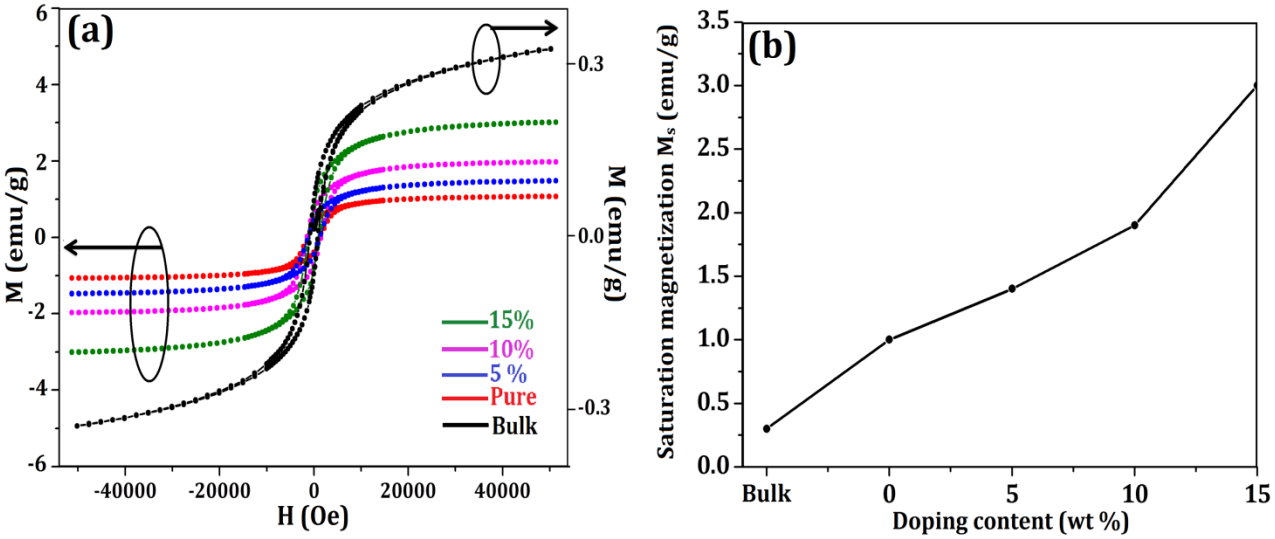

Figure 4.10 (a) M-H hysteresis curves of pure and Tb-doped $BiFeO_3$ nanowires (b) variation of saturation magnetization for the bulk, pure and Tb-doped $BiFeO_3$ nanowires

- Bulk nanowires possess spiral spin structure, and the antiferromagnetic axis rotates through the crystal with an incommensurate long-wavelength period of 62 nm; it cancels the macroscopic magnetization as well as inhibits the linear magnetoelectric effect [25]. However, in the present case, the size of the synthesized pure and Tb-doped $BiFeO_3$ nanowires is around 20 nm, which being less than 62 nm, modifies the cycloidal spin structure and, thus, leads to the observed ferromagnetic ordering [25, 84, 87].

- Enlarged view of M-H curve for pure and doped $BiFeO_3$ nanowires (Figure 4.11 (a)) show that there is no shift in the hysteresis loop towards negative or positive axis (except bulk $BiFeO_3$ nanowires), thus, confirming that there is no exchange coupling between the antiferromagnetic core and ferromagnetic surface [3, 62, 64, 66]. This establishes that the observed ferromagnetism is not due to the exchange interaction.

The dependency of the saturation magnetization on Tb concentration is shown in Figure 4.10 (b).Moreover, with increase in the doping concentration, an increase in saturation magnetization has been observed. Amongst the all samples, 15% Tb-doped $BiFeO_3$ nanowires exhibit the largest value of saturation magnetization, Ms = 2.8 emu/g, which is quite significant at room temperature. The increase in saturation magnetization with increase in the doping concentration may be attributed to the lattice distortion, structural transformation from rhombohedral to orthorhombic, suppression of oxygen vacancy, and doping of magnetically active ion. Consequently, the size of pure and Tb-doped synthesized nanowires (20 nm) being smaller than the long-range cycloidal spin spiral arrangement of wavelength 62 nm, result in the enhancement of the saturation magnetization, and ferromagnetic character.

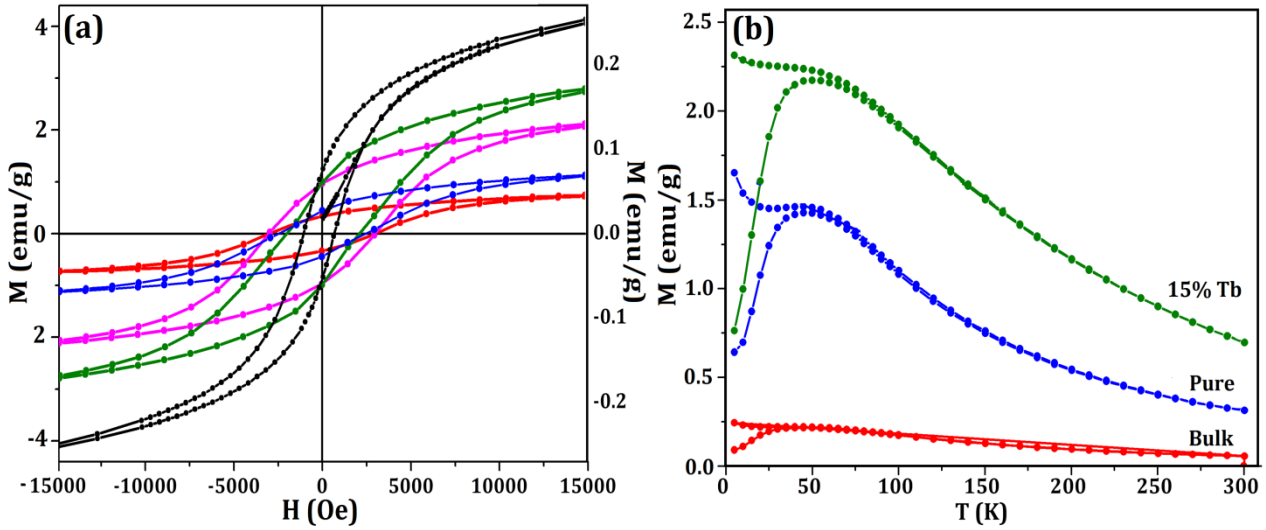

Figure 4.11 (a) Magnified M-H hysteresis view of bulk, pure and Tb-doped $BiFeO_3$ nanowires and (b) Temperature dependence of magnetization for bulk (100 nm diameter), pure and 15% Tb-doped $BiFeO_3$ nanowires showing zero field cooling and field cooling curves with applied field of 1,000 Oe

Magnetic interaction in bulk, pure and 15% Tb-doped $BiFeO_3$ nanowires have been carried out by employing temperature- dependent zero field cooling (ZFC), and, field cooling (FC) magnetization study. Figure 4.11 (b) shows the variation of the magnetic moments as a function of temperature at applied magnetic field of 1000 Oe under ZFC and FC conditions for bulk nanowires, pure and 15% Tb-doped $BiFeO_3$ nanowires.

- Splitting between ZFC and FC curves below 100 K has been observed for the bulk, pure and 15% Tb-doped $BiFeO_3$ nanowires, which suggests their size-dependent ferro/ferri-magnetic behaviour. The divergence between ZFC and FC curves increases with decrease in temperature. The splitting of ZFC and FC curves is more prominent in pure and Tb-doped $BiFeO_3$ nanowires, and it increases at higher applied magnetic field. The observed deviation is due to the nanosize of synthesized nanowires; this induces extra strain, coordination distortion, and lattice disorder on their surface compared to bulk nanowires. It results in a different frustrated spin structure, and high magnitude of magnetic spin-strain interaction. Remarkably, the observed behaviour is unique to the nanosize of $BiFeO_3$ nanowires; this effect is absent in the bulk nanowires.
- Moreover, large and broad splitting between ZFC and FC curves, observed in pure and Tb-doped $BiFeO_3$ nanowires, confirms their spin-glass behaviour [85]. The observed spin-glass behaviour is also, due to the nanosize (size confinement effects), and the phase transformation from rhombohedral to orthorhombic. The ZFC and FC curves also show broad peak at transition temperature (spin reorientation transition) around 75 K due to nanosize effect in pure and Tb-doped $BiFeO_3$ nanowires. But in the bulk nanowires, it starts appearing around 40 K due to their size being higher than the critical spin spiral ordering (62 nm) [3, 62, 64, 66]. SEM confirms that the diameter of pure and Tb-doped $BiFeO_3$ nanowires (~ 20 nm), being smaller than the critical spin spiral structure (62 nm), results in the orientation of Fe^{3+} spins toward the direction of applied field, generated by the breaking of antiferromagnetic spiral ordering [85]. Due to this orientation, there is an overall decrease in the magnetic susceptibility and the transition temperature being shifted from 40 to 75 K.

4.2.1.5 Ferroelectric analysis

In order to ascertain the ferroelectric behaviour, the measurement of polarization, as a function

of electric field (P–E), was carried out at room temperature using ferroelectric loop tracer under an applied electric field (E) of about 550 kV/cm at frequency (f) = 10 kHz (shown in Figure 4.12). It can be easily observed from the P-E loops that doping of Tb and size of nanowires produce significant changes in the ferroelectric properties. P-E loop of the pure $BiFeO_3$ nanowires displays elliptical shape, which may be due to high-leakage current (to be discussed in leakage current density versus electric field measurement), and defects or oxygen vacancies. However, the decrease in the size of nanowires from 100 to 20 nm, along with Tb-doping results in rectangular-shape like loop - a significantly good ferroelectric property. Well-saturated rectangular P-E loops have been observed in case of 10% and 15 % Tb doped $BiFeO_3$ nanowires. Moreover, as we move from bulk nanowires, i.e., 100 to 20 nm, Tb-doped nanowires, the saturation polarization increases (Figure 4.12 (b)).

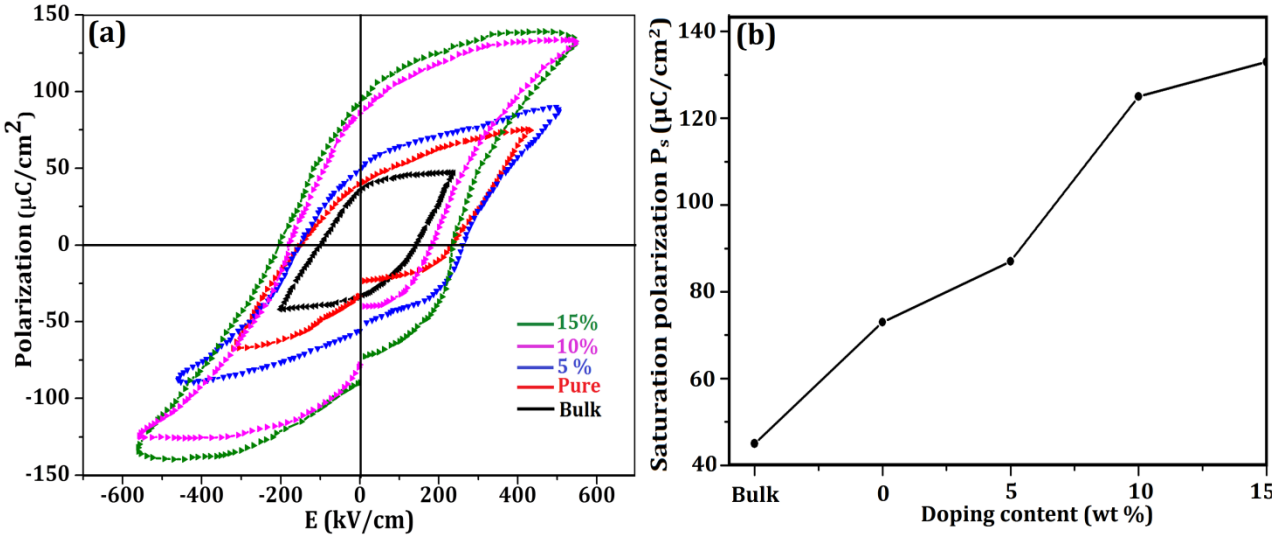

Figure 4.12 Polarization versus electric field (P-E) hysteresis loop, and (b) Variation of saturation polarization for bulk, pure and Tb-doped $BiFeO_3$ nanowires

The observed remarkable improvement in spontaneous and saturation polarization could be attributed due to the following reasons:

- Structural transformation from rhombohedral to orthorhombic perovskite structure results in lattice distortions. There is a strong tussle between the rhombohedral lattice distortion

and the structural transition, which is favourable for the increase in spontaneous polarization, resulting in the best ferroelectric properties.

- Doping decreases the oxygen-related defects, suppresses the formation of secondary phases as well as the space charge defects, which further reduce the leakage current (Figure 4.14). As a result of this, an improvement is observed in the domain pinning effects, and subsequently, the spontaneous polarization [3, 64].
- On moving from bulk to pure, and Tb-doped nanowires, the average grain size decreases, which results in lower space charge density and smaller leakage current density, thereby increasing the spontaneous polarization [3, 64, 133-134].

4.2.1.6 Dielectric analysis

Figure 4.13 shows the frequency dependence of the dielectric constant at room temperature. The dielectric constant decreases with increase in frequency, and remains fairly constant at higher frequencies. The increase in dielectric constant at low frequencies, ≤ 1 kHz, may be due to the dipole relaxation phenomenon where the dipoles at low frequenciesare able to track the frequencies of applied field. These dipoles are formed due to the charge defects and localized charges.

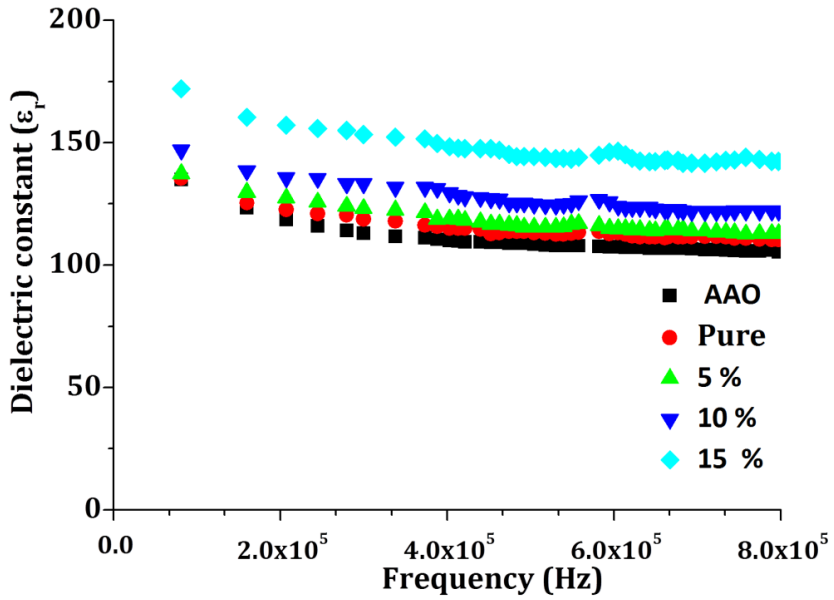

Figure 4.13 Relative dielectric constant (ε_r) vs. frequency (f) curves for the bulk, pure and Tb-doped $BiFeO_3$ nanowires

Also, at room temperature and at all frequency ranges, the dielectric constant increases with increase in doping concentration of Tb.The observation of higher dielectric constant for 15 % Tb-doped $BiFeO_3$ nanowires may be due to the formation of large dipole moment by structural distortion from rhombohedral to orthorhombic. There are four primary mechanisms responsible for the polarization of materials and each involves a short-range motion of charges, which contribute to the net polarization of the material: (i) Electronic polarization - observed at very high frequency of the order of 10^{15} Hz, (ii) Atomic and ionic polarization – observed in the infrared range of frequencies 10^{10}–10^{13} Hz, (iii) Dipolar or oriental polarization - taking place in the sub-infrared range of frequencies 10^{3}–10^{6} Hz, and (iv) Interfacial polarization - sensitive in the low frequency range of 10^{3} Hz. Dipolar and interfacial polarization play main role in present dielectric measurement because in the high frequency range, the dielectric constant becomes saturated. In the sub-infrared range of frequency, dipolar polarization contributes to the dielectric properties [76, 135]. The polarization corresponding to this mechanism occurs at a frequency range 10^{3}–10^{6} Hz at room temperature [135]. The interfacial polarization mechanism occurs when mobile charge carriers are impeded by a physical barrier that inhibits charge migration. The charges pile up at the barrier, producing a localized polarization of the materials. The frequency range of sensitivity for interfacial polarization is in the low frequency range, and may extend to the kilohertz (10^{3}Hz) range [136].

4.2.1.7 Leakage current density versus applied electric field (J-E) characteristics

The characteristics of the leakage current density versus applied electric field (J-E) of nanowires embedded in AAO templates have been studied to get feedback regarding the leakage current phenomenon associated with the $BiFeO_3$ (Figure 4.14). All the J-E curves display excellent symmetry under positive and negative applied electric fields. The bulk nanowires show leaky behaviour, with lowest leakage current density of $1.0x10^{-1}A/cm^2$ at100 kV/cm. The observed high-leakage current density in bulk $BiFeO_3$ nanowires, is attributed to space charges such as oxygen vacancies, defects, volatilization of Bi and secondary phases. These defects act as trapping centres. The trapped electrons can be activated for conduction on applying electric field, which results in increasing leakage current density. However, leakage current density decreases with increase in Tb concentration. At applied electric field of 100kV/cm, the leakage current density of 15 % Tb-doped $BiFeO_3$ nanowires comes out to be 6.0×10^{-4} A/cm^2, which is about

three orders of magnitude less than that observed for the bulk $BiFeO_3$ nanowires($1.0x10^{-1}$ A/cm^2). The substitution of Tb for Bi reduces the defects, oxygen vacancies, thereby resulting in the decrease in the leakage current density.

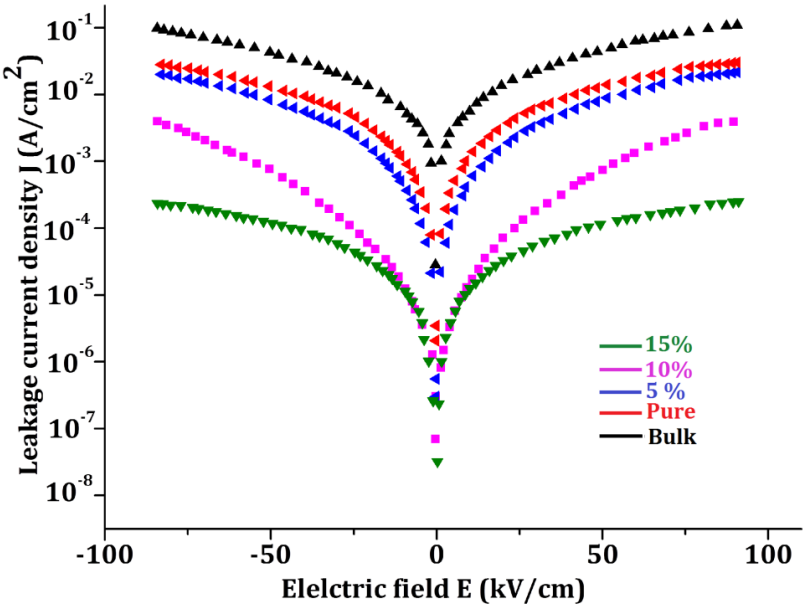

Figure 4. 14 Leakage current density (J) versus applied electric field (E) curves for the bulk nanowires, pure and Tb-doped $BiFeO_3$ nanowires

This clearly reveals that the leakage current can be effectively reduced by substitution of Tb in $BiFeO_3$. The reduction in leakage current in 15 % Tb-doped $BiFeO_3$ nanowires can also be attributed to the mismatch between the radii of Bi and Tb, and, the structural changes from rhombohedral to orthorhombic. Similar observation has been reported by Lotey [61], in which reduction in leakage current has been found in 10% Gd-doped $BiFeO_3$ nanoparticles. The significant decrease in the leakage current density for 15 % Tb-doped $BiFeO_3$ nanowires is an encouraging result, and this would be useful for multiferroic devices. Moreover, the pure and doped $BiFeO_3$ nanowires, having smaller grain boundaries, possess space charge density, which leads to smaller leakage current [61, 64].

4.2.1.8 Magnetoelectric measurements

Magnetoelectric coupling has been indirectly established by measuring the change in dielectric constant in varying applied magnetic field. The effect of size and Tb-substitution in

$BiFeO_3$nanowires on magnetic field-induced changes in dielectric constant, have been measured at 10 kHz as a function of applied magnetic field as shown in Figure 4.15. Magnetodielectric coupling coefficient (MD), i.e. the variation of the dielectric constant as a function of the applied magnetic field, is defined as [62, 64, 66]:

$$MD = \Delta\boldsymbol{\varepsilon}_r/\boldsymbol{\varepsilon}_r(0) = [\boldsymbol{\varepsilon}_r(H) - \boldsymbol{\varepsilon}_r(0)]/\boldsymbol{\varepsilon}_r(0)$$

where$\boldsymbol{\varepsilon}_r$ (H) and $\boldsymbol{\varepsilon}_r$ (0) are the dielectric constants, respectively, with and without the magnetic field, and $\Delta\boldsymbol{\varepsilon}_r$ is the change in dielectric constant. Figure 4.15 reveals that the MD increases with increase in applied magnetic field for all the samples at room temperature. A very high value of MD, 7.2 %, has been observed for 15 % Tb-doped $BiFeO_3$ nanowires. Similar interesting effects are reported elsewhere in Sm, and Co co-doped $BiFeO_3$ ceramics [137]. The increase in MD effect can be explained on the basis of the following facts:

- Reduction in lattice parameters and structural transformation: With decrease in size of nanowires from 100 to 20 nm as well as Tb-doping in $BiFeO_3$ leads to reduction in lattice parameters, and structural transformation from rhombohedral to orthorhombic (as confirmed in XRD study). This improves magnetoelectric coupling.
- Magnetostriction effect: It occurs due to the change in lattice parameters with application of magnetic field. The bulk and Tb-doped $BiFeO_3$ nanowires get strained on application of magnetic field due to the coupling between ferroics domains. This induces stress in the nanowires thereby generating the electric field in nanowires. The induced electric field orients the ferroelectric domains, and subsequently magneto-dielectric behaviour modifies. The high value of MD in Tb-doped $BiFeO_3$ is due to the increase in magnetic ordering, which strengthens the sub-lattice interactions.
- Exchange interactions: The high value of MD in Tb-doped $BiFeO_3$ nanowires is due to the constraint through the exchange interactions between the Tb-dopant and Fe spins. The spin-exchange constriction model, i.e., microscopic origin of ferroelectric polarization has been considered to explain the observed behaviour. Doping of Tb^{3+} ions leads to collapse of modulated space spin structure from long range canted antiferromagnetic orders. The interactions between 4f electrons of Tb^{3+}, and 3d electrons of Fe^{3+} spins lead to parallel distribution of Fe spins with magnetic moments of adjacent Tb^{3+} ions, and, antiparallel with successive Tb^{3+} ions when magnetic field is applied. This results in

cooperatively shifting of Tb^{3+} layers towards or away from Fe^{3+} layers with antiparallel or parallel spins through magnetostriction. This generates polarization, and consequently the MD is enhanced.

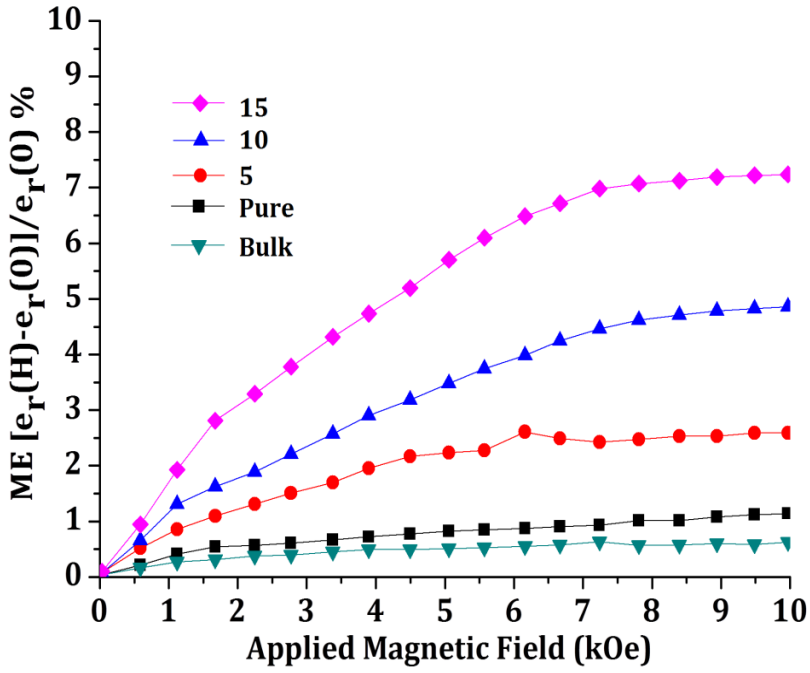

Figure4.15 Magnetoelectric vs. applied magnetic field for bulk, pure and Tb-doped $BiFeO_3$ nanowires

- Leakage current density: MD effect may be observed in low resistive materials in which leakage current can be induced by application of magnetic field. In our case resistivity increases, and, the leakage current density decreases with Tb-doping. This further decreases with decrease in size of nanowires. Therefore, the leakage current density is not responsible for the observed MD coupling.

Moreoveras stated by Catalan et al. 2006 [40, 119], the change in dielectric constant under the applied magnetic field is indirect evidence of magnetoelectric coupling, and the magnetoelectric coupling may also be observed due to combination of magnetoresistance and Maxwell-Wagner effect.

4.3 Phase-dependent multiferroism in Dy-doped $BiFeO_3$ nanowires

In this section, phase-dependent multiferroic properties of pure and Dy-doped $BiFeO_3$ nanowires have been investigated. Pure and 15 % Dy-doped $BiFeO_3$ nanowires of 20-nm size have been synthesized by colloidal dispersion template-assisted technique as explained in chapter 2. X-ray diffraction study reveals that pure $BiFeO_3$ nanowires possess rhombohedral structure; however, 15 % Dy-doped $BiFeO_3$ nanowires are orthorhombic. X-ray photoemission analysis confirms the +3 oxidation state of Fe (Fe^{3+}), and high purity of samples. Magnetic study confirms that the synthesized nanowires exhibit ferromagnetic behaviour, and, that the value of saturation magnetization increased with structural change as well as with Dy-doping. Polarization versus electric field study clearly reveals that the pure $BiFeO_3$ nanowires possess elliptical loop due to leaky behaviour but 15% Dy-doping results in well saturated rectangular loop. Leakage current density decreases with increase in Dy doping. The magnetoelectric coupling in the synthesized nanowires has been estimated by magnetodielectric measurement. High value of magnetodielectric coefficient, 4.85 %, has been observed for 15 % Dy-doped $BiFeO_3$ nanowires [64]

4.3.1 Results and discussions

4.3.1.1 Morphological study

Figure 4.16 (a) to (d) show SEM micrographs for the pure and Dy-doped $BiFeO_3$ nanowires, and, their dense growth. In Figure 4.16 (a), the SEM micrographs of pure $BiFeO_3$ nanowires (at low magnification) reveal crop like uniform growth of nanowires. Moreover, synthesized nanowires have been found to be uniformly dense, homogeneous, parallel, and well aligned. The SEM of pure $BiFeO_3$ nanowires (Figure 4.16 (c)) at higher magnification divulges the uniformity of the synthesized nanowires. Diameter of pure $BiFeO_3$ (Figure 4.16 (b)) and Dy-doped $BiFeO_3$ (figure 4.16 (d)) nanowires have been found to be around 20 nm.

4.3.1.2 Crystallographic analysis

Figure 4.17 shows the x-ray diffraction (XRD) patterns of pure, and Dy-doped $BiFeO_3$ nanowires embedded in AAO matrix. Figure 4.17 (a) reveals that XRD patterns of pure $BiFeO_3$ nanowires exactly match with hexagonal phase having rhombohedral structure (JCPDS file no. 86–1,518). Some additional peaks indicated by "*" associated with secondary impurities, have also been

detected in the pure $BiFeO_3$ nanowires. No such peaks, related to secondary impurities, have been observed in Dy-doped $BiFeO_3$ nanowires. This reveals that 15 % doping of Dy in $BiFeO_3$ host leads to:

- suppression of secondary impurities, and simultaneously
- splitting of peaks indexed as (104), (110) and (006), (202) for 2θ values positioned around 32^o and 39^o, respectively, get merged to a single peak
- complete structural transformation from rhombohedral to orthorhombic

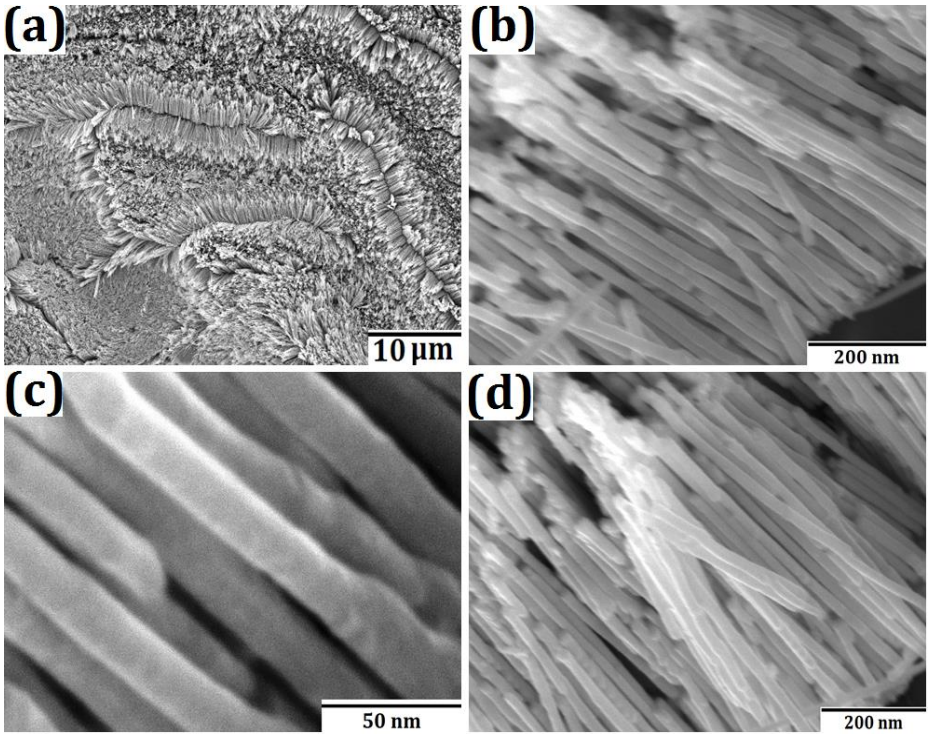

Figure 4.16 SEM micrographs (a) to (c) Pure $BiFeO_3$ nanowires at different magnifications, and (d) 15 % Dy-doped $BiFeO_3$ nanowires

Similar phenomenon of phase transformation with addition of Dy in $BiFeO_3$ host material had been observed by other groups [139-140]. This structural transformation might be significant for the ferroelectric and dielectric properties of the synthesized nanowires. Moreover, no additional peaks related to Dy or any of its compounds have been observed in XRD patterns (Figure 4.17 (a)). It demonstrates the good dispersivity and incorporation of Dy dopant in the host material. Doping of 15% Dy in $BiFeO_3$ found to be optimum as further increase in Dy content leads to

appearance of secondary impurities. Moreover, no peak related anodic alumina oxide (AAO) Al_2O_3 template has been seen in XRD patterns because of their amorphous nature.

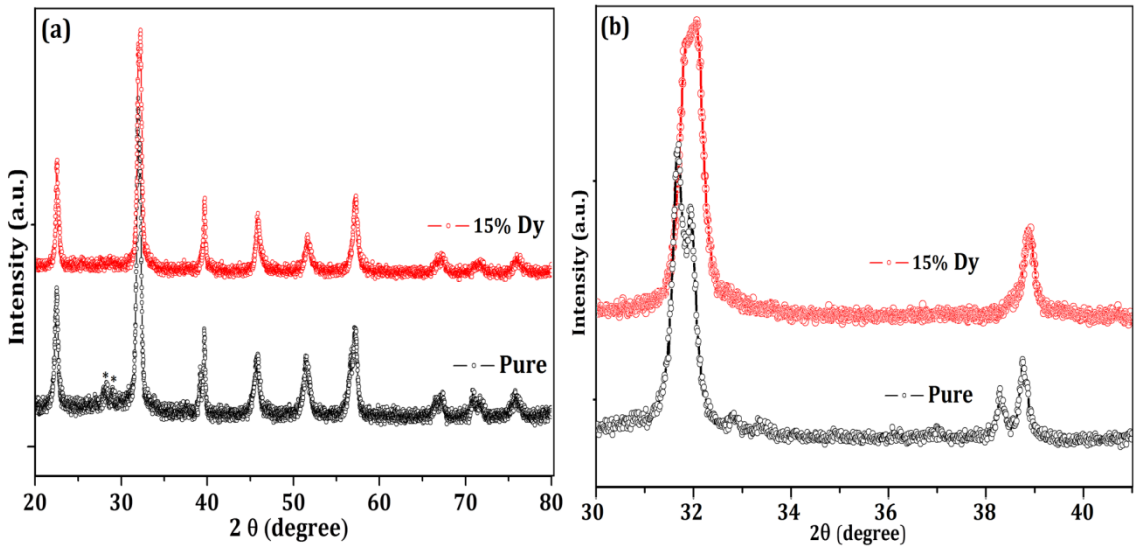

Figure 4.17 X-ray diffraction patterns (a) pure and Dy-doped $BiFeO_3$ nanowires and (b) Magnified XRD patterns of (104), (110) and (006), (202) reflections at $2\theta \sim 32^o$ and 39^o

4.3.1.3 XPS analysis

The XPS analyses of phase purification, chemical bonding and oxidation states of Bi, Fe, O and Dy of 15% Dy-doped $BiFeO_3$ nanowires through wide range of spectrum, from 0 to 1,000 eV, have been shown in Figure 4.18. The two peaks (Figure 4.18) positioned respectively at 158 and 164 eV, corresponding to Bi $4f_{7/2}$ and Bi $4f_{5/2}$, confirm the trivalent oxidation state of Bi (Bi^{3+}). To plaid the oxidation state of Fe, the magnified XPS spectrum in range of 705 to 730 eV has been investigated (inset Figure 4.18). The background correction and oxidation state of Fe in $BiFeO_3$ have been carried out using Shirley background subtraction by non-linear least square fitting using mixed Gauss-Lorentz function. Two main photo emission peaks positioned at 711.2 and 723.7eV, assigned to Fe^{3+}, and are the spin orbit doublet $2p_{3/2}$ and $2p_{1/2}$ of Fe^{3+} the oxidation state. These peaks confirm the 3+ oxidation state of Fe in the synthesized nanowires. Apart from these peaks, two other additional peaks, positioned around 715 and 717 eV, called, respectively, the surface peak and the satellite peak, have also been observed. Surface peak observed at 715 eV is because of the decrease of co-ordination number of Fe^{3+}cations located at the surface of nanowires with Dy doping as also observed in XRD. And satellite peak around 717 eV has been

observed because of the shake-up process. No extra peak corresponding to Fe^{2+} oxidation has been observed in the XPS spectra; it indicates the dominant role of Fe^{3+} ion for observed ferromagnetism in pure and Dy-doped $BiFeO_3$ nanowires (to be discussed in magnetic analysis ahead (Figure 4.19)).

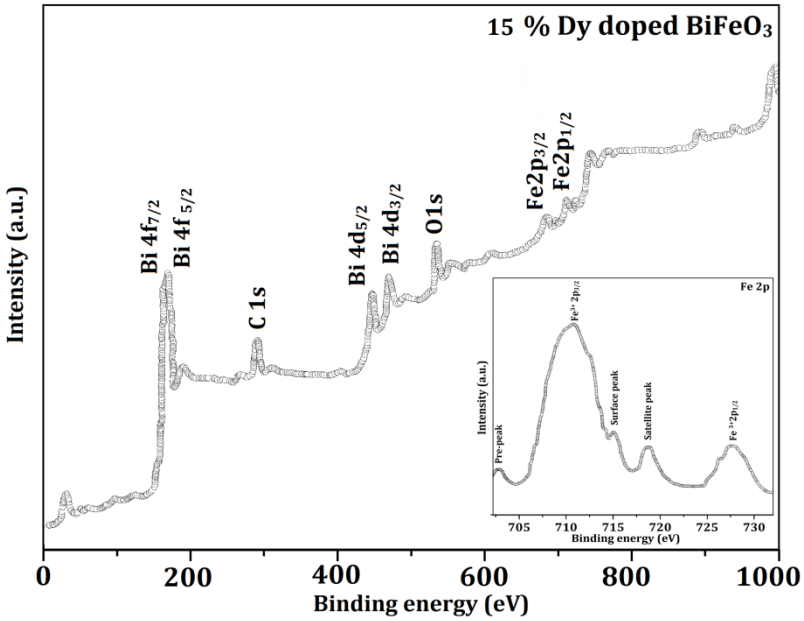

Figure 4.18 XPS spectrum of 15 % Dy-doped $BiFeO_3$ nanowires. Inset show XPS of Fe 2p

The peak positioned at 530.8 eV is attributed to O^{2-} oxidation state in $BiFeO_3$ lattice. It is clear from Figure 4.18 that no additional peak related to Dy in metallic or oxide form such as Dy and Dy_2O_3 or Dy_2O_3 has been observed in the XPS spectra, despite the Dy concentration being increased up to 0.15 in the $BiFeO_3$ host. This reveals that the Dy is likely to play the role of Bi, which is further confirmed by the XRD measurement. The peak observed at 285 eV is due to the small amount of adsorbed carbon that was used to calibrate the acquired spectrum. In addition to this, no extra peaks of any impurities or secondary phase have been observed in the XPS spectrum, which confirms the high purity of the samples.

4.3.1.4 Magnetic analysis

Figure 4.19 shows the magnetization versus applied magnetic field (M-H) hysteresis loops of pure and Dy-doped $BiFeO_3$ nanowires at room temperature. The saturation magnetization has

been achieved within the applied field of 50 kOe revealing their typical ferromagnetic character. The XPS study rules out the presence of Fe^{2+} ions or any other impurity in doped-$BiFeO_3$; it confirms that the observed ferromagnetic character is not because of the presence of these ions or any other impurity phases in the nanowires.

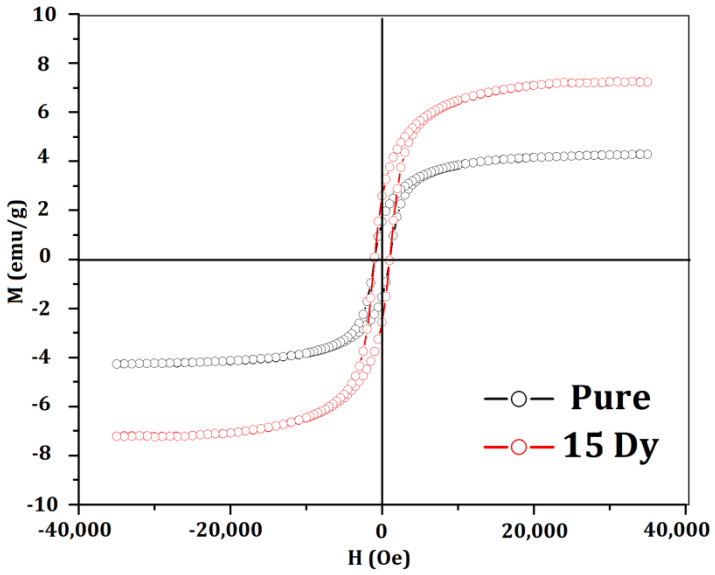

Figure 4.19: Magnetization versus applied field (MH) hysteresis loops of pure and 15% Dy-doped $BiFeO_3$ nanowires

The observed ferromagnetic behaviour in pure and Dy-doped $BiFeO_3$ nanowires could be ascribed to following reasons:

- Bulk $BiFeO_3$ (having size > 62nm) possesses spiral spin structure, and the antiferromagnetic axis rotates through the crystal with an incommensurate long-wavelength period of 62 nm; it cancels the macroscopic magnetization as well as inhibits the linear magnetoelectric effect [40]. However, in the present case, the size of the synthesized pure and doped $BiFeO_3$ nanowires has been found to be around 20 nm, which being less than 62 nm, modifies the cycloidal spin structure and, thus, leads to the observed ferromagnetic ordering [3, 25, 30, 85].
- Decrease in the particle size of $BiFeO_3$ (antiferromagnetic system) results in the net magnetic moment, produced due to non-exact compensation of the two magnetic sub-

lattices. This non-compensation at the surface of the $BiFeO_3$ nanowires may be a primary cause for the observed ferromagnetism [3].

- Doping of magnetically active Dy^{3+} ions, having radius smaller than that of the Bi^{3+} ion, results in larger distortion in lattice structure thereby leading to suppression of spiral spin modulation in $BiFeO_3$. This is precisely because the spin cycloid of Dy^{3+}, which got destroyed on the structural transformation of the rhombohedral to orthorhombic, as has already been observed in the XRD study [3, 62, 65-66, 139-140]

4.3.1.5 Electrical analysis

4.3.1.5.1 Ferroelectric study

Figure 4.20 shows polarization as a function of electric field (P–E) measurements carried out at room temperature using ferroelectric loop tracer under an applied electric field (E) of about 600 kV/cm at frequency (f) = 10 kHz.P-E loops of Dy-doped $BiFeO_3$ reveal that the Dy-doping as well as the size of the synthesized nanowires produce significant changes in the ferroelectric properties.P-E loop of the pure $BiFeO_3$ nanowires displays elliptical shape, which may be due to the high-leakage current (to be discussed in leakage current density versus electric field measurement), and defects/ oxygen vacancies. Well-saturated rectangular P-E loops have been observed in Dy-doped $BiFeO_3$ nanowires. The observed remarkable improvement achieved in spontaneous saturation polarization may be attributed due to structural transformation, and, nano-size of synthesized nanowires.

First, the doping of Dy in $BiFeO_3$ leads to structural transformation from rhombohedral to orthorhombic perovskite structure leading to lattice distortions, and, result in a strong tussle between the rhombohedral lattice distortion, and the structural transition. This is the cause of well saturated rectangular like PE loops, and thereby enhanced ferroelectric properties [3, 136, 138-139]. Moreover, doping decreases the oxygen-related defects, suppresses the formation of secondary phases (confirmed in XRD) as well as the space charge defects: this collectively further reduces the leakage current. As a result, an improvement is observed in the domain pinning effects, and the spontaneous polarization [3].

Second, the average grain size of the synthesised nanowires is small which results in lower space charge density, and, smaller leakage current density, thereby increasing the spontaneous polarization.

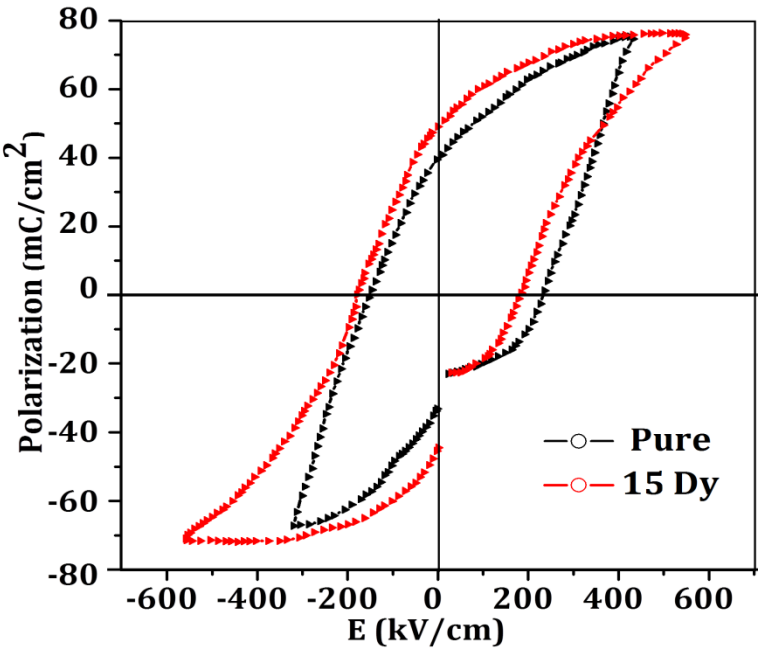

Figure 4.20 Polarization versus electric field hysteresis loops of pure and 15% Dy-doped $BiFeO_3$ nanowires

4.3.1.5.2 Dielectric study

Figure 4.21 illustrates the frequency dependence of the relative dielectric constant, at room temperature, for pure and Dy-doped $BiFeO_3$ nanowires, which has been found to follow a normal pattern, i.e., on the whole, both the curves monotonously decrease with increasing the frequency, however, remaining fairly constant at higher frequencies. In the lower frequency range (~10^3Hz), the dielectric constant reduces rapidly from 137 to 106 for pure $BiFeO_3$ nanowires, and 148 to 121 for Dy-doped $BiFeO_3$ nanowires. The observed trend in the dielectric constant can be credited to two main sources, namely (i) dipole relaxation phenomenon and interfacial polarization occurring at lower frequencies (ii) dipolar and oriental polarization, at higher frequencies [135-136].Firstly, at lower frequencies ≤ 1 kHz, the dipoles formed due to the charge defects and the localized charges, track the frequencies of applied field. More importantly, the interfacial polarization also occurs at frequency range ~ 10^3 Hz. The interfacial polarization befalls when mobile charge carriers are impeded by a physical barrier that inhibits charge migration. The charges pile up at the barrier producing a localized polarization of the materials.

The frequency range of sensitivity for interfacial polarization lies in the low frequency range, and may extend to kHz [136].

Secondly, however, at higher frequencies (~ 10^3–10^6 Hz), the dipolar or oriental polarization takes places, and the dielectric constant becomes saturated. At this frequency range, the diploes are completely formed due to high applied field, and, the dipolar polarization contributes to the dielectric properties at room temperature [135].

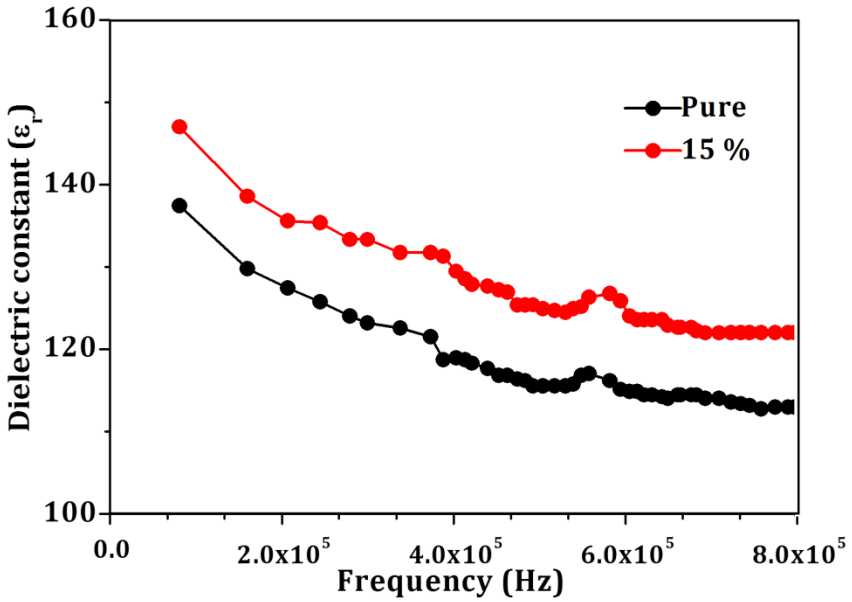

Figure4.21 Relative dielectric constant (ε_r) vs. frequency curves for the bulk, pure and Dy-doped $BiFeO_3$ nanowires

Moreover, Figure 4.21 reveals that the 15% Dy-doping in the host $BiFeO_3$ leads to increase in the value of dielectric constant at all the frequency ranges. The observation of higher dielectric constant for 15 % Dy-doped $BiFeO_3$ nanowires may be due to the formation of large dipole moment due to structural distortion from rhombohedral to orthorhombic [3].

4.3.1.5.3 Leakage current density versus applied electric field (J-E) characteristics

Figure 4.22 shows the leakage current density versus applied electric field (J-E) characteristics of the synthesized nanowires embedded in AAO templates displaying excellent symmetry under positive and negative applied electric fields, and, thus, providing feedback regarding the leakage current phenomenon associated with the $BiFeO_3$ (Figure 4.22). The pure $BiFeO_3$ nanowires

show leaky behaviour with lowest leakage current density of 9x10-^{2}A/cm^{2} at100 kV/cm due to space charges such as oxygen vacancies, defects, volatilization of Bi and secondary phases (as confirmed in XRD). These defects act as trapping centres. The trapped electrons can be activated for conduction on applying electric field, which results in increasing leakage current density [61, 135-136].The 15% Dy-doping in $BiFeO_3$ results in leakage current density, 1.0x10^{-4} A/cm^{2}, at applied electric field of 100kV/cm, which is about three orders of magnitude less than that of pure $BiFeO_3$ nanowire (9x10^{-2}A/cm^{2}). The XRD study reveals (Figure 4.17) that the substitution of Dy for Bi suppresses the secondary impurities reducing defects, and decreases the oxygen vacancies, and, thereby decreasing the leakage current density. The structural distortion also favours the low leakage current. The significant decrease in the leakage current density for doped $BiFeO_3$ nanowires is an encouraging result, and, is useful for multiferroic devices.

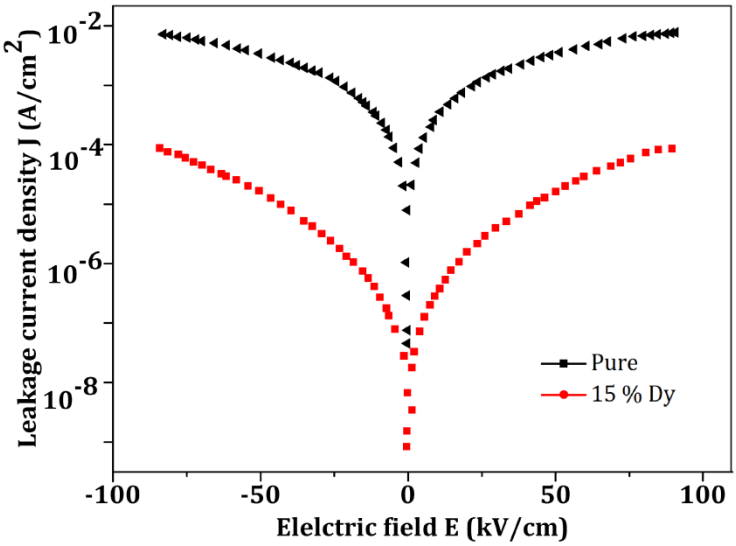

Figure 4.22 Leakage current density (J) versus applied electric field (E) curves for the pure and 15% Dy-doped $BiFeO_3$ nanowires

4.3.1.6 Magnetoelectric coupling analysis

Magnetoelectric coupling investigation, in the synthesized nanowires, has been carried out indirectly by measuring the change in dielectric constant in varying applied magnetic field. The effect of size, phase transformation, as well as Dy-substitution in $BiFeO_3$ nanowires on the magnetic field, inducing changes in dielectric constant, have been measured at 10 kHz as a function of applied magnetic field as shown in Figure 4.23. Magnetodielectric coupling (MD),

i.e. the variation of the dielectric constant as a function of the applied magnetic field is defined as [65-66, 137]:

$$MD = \Delta\boldsymbol{\varepsilon}_r/\boldsymbol{\varepsilon}_r(0) = [\boldsymbol{\varepsilon}_r(H) - \boldsymbol{\varepsilon}_r(0)]/\boldsymbol{\varepsilon}_r(0)$$

where $\boldsymbol{\varepsilon}_r(H)$ and $\boldsymbol{\varepsilon}_r(0)$ are the dielectric constants, respectively, with and without the magnetic field, and $\Delta\boldsymbol{\varepsilon}_r$ is the change in dielectric constant.

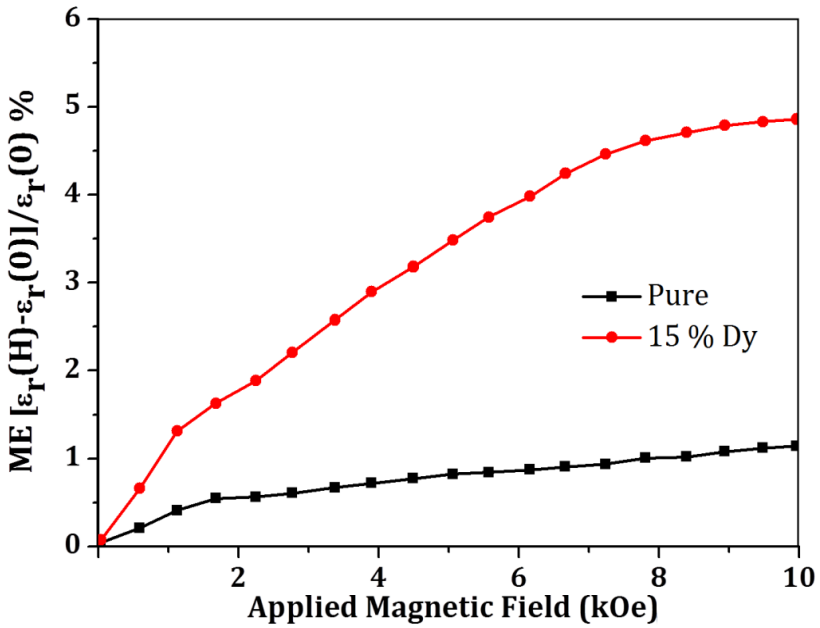

Figure 4.23 Magnetoelectric vs. applied magnetic field for pure and Dy-doped $BiFeO_3$ nanowires

It is clear from the Figure 4.23 that the MD increases with increase in applied magnetic field for pure and Dy-doped $BiFeO_3$ nanowires at room temperature. For 15% Dy-doped $BiFeO_3$ nanowires, a very high value of MD, 4.85 %, has been observed. Similar interesting effects are reported elsewhere in Sm, and Co co-doped $BiFeO_3$ ceramics [137]. The observed high value of MD can be attributed to the following reasons:

- Enhancement in magnetoelectric coupling resulting due to nano-sized $BiFeO_3$ wires as well as simultaneous doping of Dy leading to reduction in lattice parameters, and structural transformation from rhombohedral to orthorhombic (as confirmed in XRD study) [40, 138-139]

- Simultaneous existence of ferromagnetism and ferroelectricity (Figure 4.19 and 4.20) in the synthesized nanowires
- Change in the lattice parameters with the application of magnetic field (in fact, the nanowires get strained on application of magnetic field due to the coupling between ferroics domains and, as a result, inducing stress thereby generating the electric field, which, further, orients the ferroelectric domains and subsequently magneto-dielectric behaviour modifies)
- Spin-exchange constriction, and exchange interactions between the Dy-dopant and Fe spins (what actually happens is as under: Doping of magnetically active ions, Dy^{3+}, leads to collapse of modulated space spin structure from long range canted antiferromagnetic orders. The interactions between 4f electrons of Dy^{3+}, and 3d electrons of Fe^{3+} spins lead to parallel distribution of Fe spins with magnetic moments of adjacent Dy^{3+} ions, and antiparallel with successive Dy^{3+} ions when magnetic field is applied. This results in cooperatively shifting of Dy^{3+} layers towards or away from Fe^{3+} layers with antiparallel or parallel spins through magnetostriction so that it generates polarization, and consequently the MD gets enhanced

Moreover, as stated by Catalan et al. 2006 [40, 119], the change in dielectric constant under the applied magnetic field is an indirect evidence of magnetoelectric coupling, which may also be observed due to combination of magneto-resistance and Maxwell-Wagner effect.

4.4 Multiferroism in rare earth metals-doped $BiFeO_3$ nanowires

In this section, multifunctional undoped and rare earth metals ions (Gd^{3+}, Tb^{3+}, Dy^{3+})-doped $BiFeO_3$ nanowires, with 20 nm diameter, have been synthesized by template-assisted colloidal dispersion technique as explained in chapter 2. The effect of the size of synthesized nanowires, as well as, the doping of rare earth ions on the structural, magnetic, dielectric and magnetodielectric properties have been studied. The doping of rare earth metal ions leads to structural transition from rhombohedral to orthorhombic $BiFeO_3$ nanowires. The synthesized nanowires exhibit ferromagnetic nature with high value of saturation magnetization, dielectric constant and magnetodielectric coefficient [66].

4.4.1 Results and discussion

4.4.1.1 Crystallographic and morphological analyses

Figure 4.24 shows XRD patterns of the synthesized nanowires. XRD reflection peaks of undoped $BiFeO_3$ are indexed, and well matched with polycrystalline rhombohedral distorted perovskite (R3c) possessing hexagonal phase (JCPDS file no. 86–1518) [3, 30, 64-65, 104, 141-142].The peak marked by "#" attributed to secondary impurity - $Bi_2Fe_4O_9$, and, it is non-ferromagnetic (JCPDS file no. 20-0836) [104]. XRD patterns of RE-doped $BiFeO_3$ nanowires show that the splitting of reflection peaks (marked by "*") in undoped $BiFeO_3$ around $2\theta \sim 31\text{-}32^o$, $39\text{-}39^o$, $61\text{-}62^o$ and $75.5\text{-}76.5^o$ decrease, and get merged to a single peak corresponding to lattice planes (110), (202), (220) and (042) possessing orthorhombic crystal structure with P$n2_1a$ space group [3, 64-65, 105-107, 143-144]. This shows that the doping of RE leads to structural transition from rhombohedral (R$3c$) to orthorhombic (P$n2_1a$) phase. Considering the non-centrosymmetric and polar ionic displacement of $Pn2_1a$ space group, it may be concluded that the 15% substitution of RE induces polar-to-polar, i.e., R$3c$ - to - P$n2_1a$ transition.

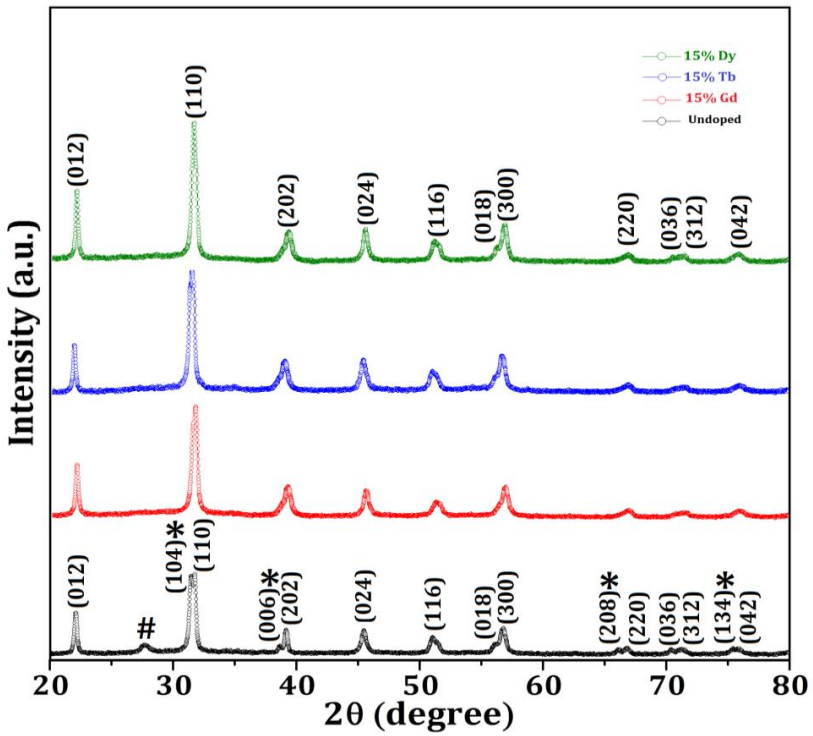

Figure 4.24: XRD patterns of undoped and RE-doped $BiFeO_3$ nanowires

The observed structural transition can be attributed to the smaller size of rare earth metal ions (RE) as compared to Bi ions, which has been explained on the basis of Goldschmidt's tolerance factor (t). The tolerance factor (t) indicates the stability and distortion of crystal structures and is given by

$$t = \frac{(R_A + R_B)}{\sqrt{2(R_B + R_o)}}$$

where R_A, R_B, R_o are the radii of A and B site ions and the O-ion, respectively, in ABO_3 perovskite structure. In general, for cubic structure, its value is 0.9 – 1 and, the size of A and B ion is same. For orthorhombic/rhombohedral structures, the value of tolerance factor lies between 0.71-0.9. The tolerance factor quantifies size mismatch between A and B ions in the cubic perovskite (ABO_3) structure. The origin of the observed orthorhombic phase in RE–$BiFeO_3$ nanowires can be explained on the basis of tolerance factor. The tolerance factor of the pure to RE-doped $BiFeO_3$ nanowires has been found to be 0.954 to 0.947, respectively. The substitution of RE in $BiFeO_3$ declines the tolerance factor value, respectively, from 0.954 to 0.947 (from undoped to Dy-doped nanowires).

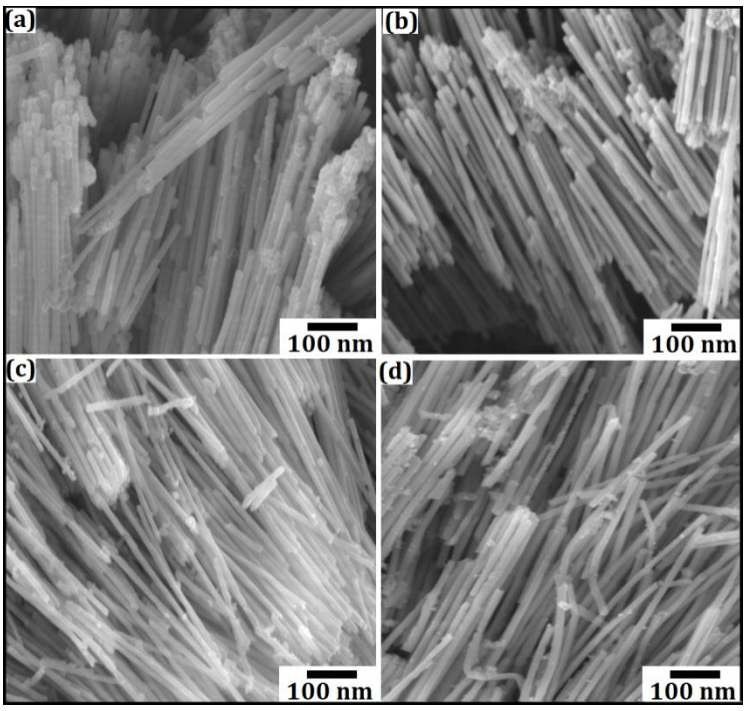

Figure 4.25: SEM micrographs of (a) undoped (b) Gd^{3+} (c) Tb^{3+} (d) Dy^{3+} doped $BiFeO_3$ nanowires

The value of tolerance factor, 0.954 to 0.947, signifies that the Fe–O and Bi^{3+}/RE^{3+}–O bonds are under compression and tension strain, respectively [105-107].This reveals that the substitution of RE in $BiFeO_3$ modifies the octahedral tilting.This in turn leads to right-shifting of characteristically diffraction peaks towards higher 2θ as well as reduction in the unit cell volume due to smaller ionic radii of the RE (Gd^{3+} = 1.27Å; Tb^{3+} = 1.25Å; Dy^{3+} = 1.24Å) than Bi^{3+} = 1.36Å [105-107]. These induced distortions make the rhombohedral phase unstable, and consequently stabilizes the orthorhombic phase.Therefore, variance of A-site cations' size and tolerance factors are responsible for the formation of orthorhombic phase along with R*3c* in RE-doped $BiFeO_3$ [105-107].Figs. 4.25 (a), (b), (c) and (d) show SEM micrographs of respectively, undoped and 15% Gd^{3+}, Tb^{3+}, Dy^{3+}-doped $BiFeO_3$ nanowires. These micrographs reveal that the synthesized nanowires are well aligned and of size 20 nm.

4.4.1.2 Magnetic analyses

Figure 4.26 shows the M-H hysteresis loops of the synthesized nanowires revealing their ferromagnetic character. It has been found that the saturation magnetization further increases with doping of RE (Figure 4.26 (inset)).

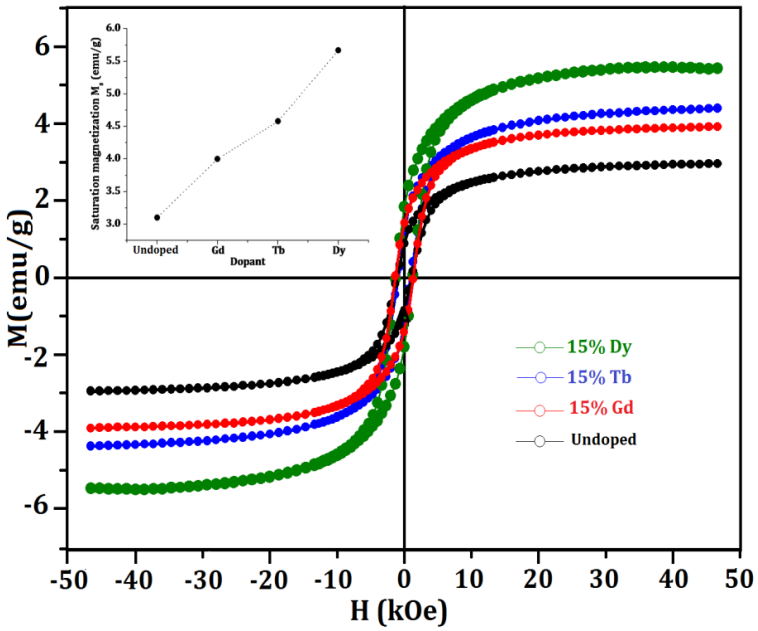

Figure 4.26: Magnetization versus applied magnetic field hysteresis loops of undoped and RE-doped $BiFeO_3$ nanowires

The observed high value of saturation magnetization in the Dy-doped $BiFeO_3$ as compared to the other ones can be attributed to first, their large magnetic moment, and, second, the smaller size of Dy^{3+} ions.The observed magnetic character and, high value of saturation magnetization in synthesized nanowires can be explained on the following facts: First, the effect of substitution of magnetically active RE having ionic radii smaller than Bi^{3+} results in larger distortion in lattice structure thereby leading to destruction of SMSS. This is precisely because the spin cycloids of RE^{3+} ions are getting destroyed with structural transition.Also, the first principle calculation suggests that the effective magnetic moment of RE is large, and on substitution in $BiFeO_3$, these coupled with Fe^{3+} ions and resulting in improved magnetism [3, 64-65]. Second, the smaller size of the synthesized nanowires. Bulk $BiFeO_3$ nanowires exhibits antiferromagnetic ordering due to the presence of SMSS [3, 15, 25, 30, 64-65, 141]. However, the size of the synthesized nanowires is 20 nm which is less than SMSS period (~ 62 nm). This modifies the cycloidal spin structure, and leads to the ferromagnetism [3, 25, 64-65]. Moreover, the smaller size of nanowires resulting in the net magnetic moment on the surface of $BiFeO_3$ due to non-exact compensation of the two magnetic sub-lattices and results in ferromagnetism [3, 25, 64-65]. Third, No shift in the MH hysteresis loop, towards negative or positive axis, establishes that the observed ferromagnetism is not due to the exchange interaction [3]. Last, the possibility of the presence of Fe^{2+} ions cannot be ruled out, which may be responsible for the observed magnetic behaviour.

4.27.1.3 **Dielectric analysis**

Figure 4.27 shows the variation of relative dielectric constant (ε_r) and dielectric loss (tan (δ)) of the synthesized nanowires at room temperature as function of frequency. Figure 4.27 reveals that both ε_r, and, tan (δ) decrease monotonously with increase in frequency at lower frequencies, but remaining fairly constant at higher frequencies. Dielectric constant at 100 kHz has been found to be 88, 114, 126 and 140 for undoped, Gd, Tb and Dy doped $BiFeO_3$ nanowires respectively. The doping of RE resulting in the high dielectric constant may be due to the formation of large dipole moment as a result of structural transition, reduction of lattice parameters or nano-size of the synthesized nanowires [64-65, 141-142]. The observed trend in the dielectric constant can be credited to two main sources;

- Dipole relaxation phenomenon and interfacial polarization – At lower frequencies (≤ 1 kHz) the dipoles got formed due to the charge defects, and localized charges tracks the frequencies of applied field. The interfacial polarization befalls when mobile charge carriers are impeded by a physical barrier that inhibits charge migration. The charges pile up at the barrier producing a localized polarization of the material [136].

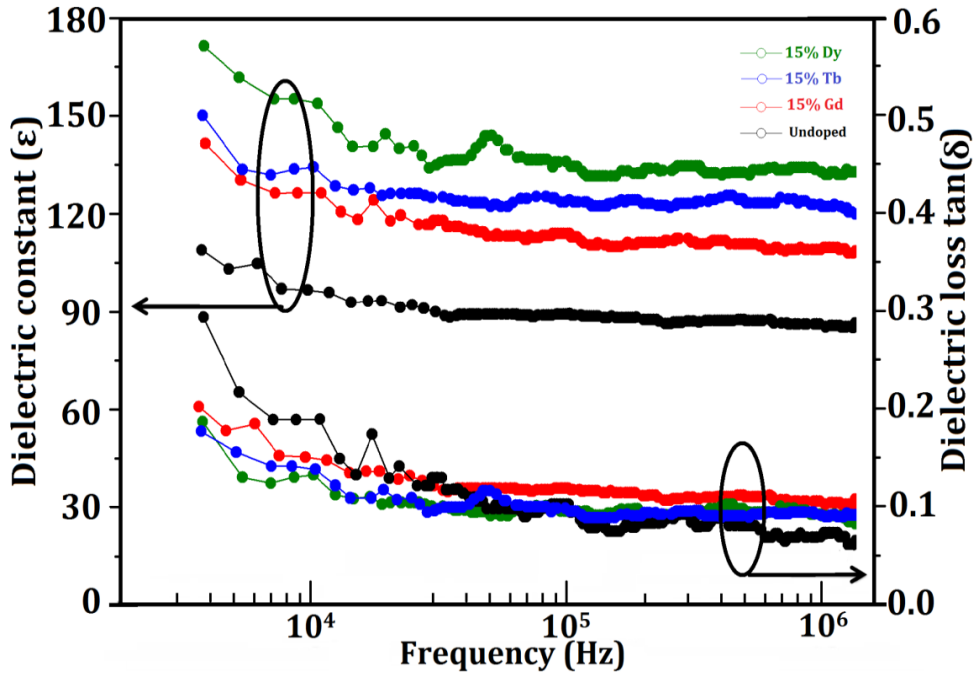

Figure 4.27: Dielectric traits of undoped and RE-doped $BiFeO_3$ nanowires

- Dipolar and oriental polarization - At higher frequencies ~ 10^3–10^6 Hz, the diploes are completely formed due to high applied field, and the dielectric constant becomes saturated due to the dipolar or oriental polarization [64-65].

4.4.1.4 Magnetodielectric coupling

Figure 4.28 shows the magnetoelectric coupling coefficient (MD) in the synthesized nanowires, i.e., variation in the dielectric constant measured at 10 kHz as a function of applied magnetic field. MD is defined as [64-65]:

$$\mathrm{MD} = \frac{\Delta\varepsilon_r}{\varepsilon_r(0)} = \frac{\varepsilon_r(\mathrm{H}) - \varepsilon_r(0)}{\varepsilon_r(0)}$$

where $\varepsilon_r(H)$ and $\varepsilon_r(0)$ are the dielectric constants at applied, and zero magnetic field as well as $\Delta\varepsilon_r$ is the change in dielectric constant with and without magnetic field, respectively. The value of MD at 20 kOe for undoped, Gd, Tb and Dy-doped $BiFeO_3$ nanowires has been found to be 2.60, 5.92, 7.65 and 8.9 % respectively.No changes in the MD upto 14 kOe for undoped nanowires have been observed, and afterward it abruptly increased.However non-linear trend has been noticed in the RE-doped nanowires.

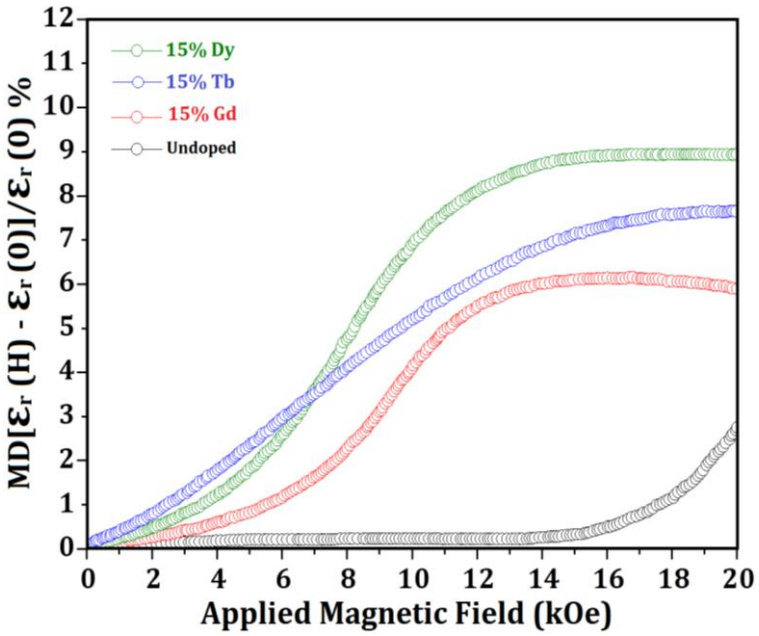

Figure 4.28: Magneto-dielectric coupling in undoped and RE-doped $BiFeO_3$ nanowires

The value of MD gets saturated for Gd and Dy doped nanowires after 12 and 14 kOe respectively. But no such behaviour has been found in undoped and Tb-doped nanowires.The observed MD effect in the synthesized nanowires can be attributed to following reasons:

- Size - Nanosize of the synthesized wires
- Doping – Doping of RE resulting in structural transition reduces lattice parameters and improving MD
- Magnetostriction - Lattice parameters of the synthesized nanowires change with application of magnetic field. This enhances MD due to the increase in the magnetic ordering and strengthening of sub-lattice interactions [25, 64-65, 115, 145]

- Spin-exchange interactions between the RE^{3+} and Fe^{3+} - Doping of RE^{3+} ions collapse SMSS of $BiFeO_3$. The interactions between 4f electrons of RE^{3+} and 3d electrons of Fe^{3+} spins lead to parallel distribution of Fe spins with magnetic moments of adjacent RE^{3+} ions and antiparallel with successive RE^{3+} ions on the application of magnetic field. This leads to cooperatively shifting of RE^{3+} layers towards or away from Fe^{3+} layers with antiparallel or parallel spins, respectively, generating polarization and consequently improving MD [25, 64-65, 119, 146].

The contribution of magneto-resistance and Maxwell-Wagner effect for the observed MD cannot be ignored [119].

Chapter 5

Conclusions and future scope

Overview

This chapter presents the brief summary of the results obtained from the morphological, structural, magnetic, electric, dielectric, magneto-dielectric/electric coupling of pure and rare earth metal ions (Gd^{3+}, Tb^{3+}, Dy^{3+})-doped $BiFeO_3$ nanostructures, viz., nanoparticles and nanowires, as described in chapters 3 and 4. The thesis discusses the synthesis and characterization of $BiFeO_3$ nanostructures with enhanced multiferroic properties. The effect of 'doping of rare earth metal ions as well as the effect of size of the synthesized nanostructures' on the multiferroic properties has also been investigated. In the end, the scope for 'future work in this area' has been discussed.

6.1 Conclusions

Following are chapter-wise conclusions:

Chapter 1: Introduction

presents the brief idea about the multifunctional materials, their magnetoelectric coupling properties, and relevant literature.

Chapter 2: Experimental Techniques

presents the synthesis techniques used for the synthesis of pure and rare earth metals, viz., Gd, Tb, Dy-doped $BiFeO_3$ nanostructures with appropriate mechanism along with the characterization techniques.

Chapter 3: $BiFeO_3$ nanoparticles

presents the study on multiferroic properties of rare earth metal ions (Gd^{3+}, Tb^{3+}, Dy^{3+})-doped $BiFeO_3$ nanoparticles synthesized by the sol-gel method. The doping-wise account is as under:

- $Bi_{1-x}Gd_xFeO_3$ nanoparticles (x = 0, 0.02, 0.04, 0.06, 0.08, 0.10, 0.12 and 0.15) have been prepared. The gradual change in the structure from rhombhohedral to orthorombic, and increase in lattice strain have been observed with increase in Gd concentration in $BiFeO_3$. XRD has been found to fix the solution limit for Gd doping in $BiFeO_3$ as 10%. The synthesized nanoparticles have been found to be homogeneous and spherical in nature having average particle size in the range of 25-15 nm. Nanoparticles exhibit ferromagnetic character and the magnetization values have been found to increase with increase in Gd concentration. XPS study confirms the oxidation state of Fe to be +3 confirming that Fe^{2+} ions are not responsible for observed magnetic behavior. Gd-doping has been found to reduce grain size, distort structure, stabilize the +3 oxidation state of Fe – as is evidenced by XPS as well as reduce the leakage current by an order of four and enhance the ferroelectric properties.
- $Bi_{1-x}Tb_xFeO_3$ nanoparticles (x = 0, 0.05, 0.10 and 0.15) of size 30-39 nm, have been synthesized. Crystallographic analysis reveals the structural transition from rhombohedral (R3*c*) to orthorhombic (P*n*2_1*a*) phase, i.e., polar-to-polar phase takes place with 15% Tb-doping in $BiFeO_3$. The synthesized nanoparticles exhibit ferromagnetic behaviour, and, the 15% Tb-doped $BiFeO_3$ nanoparticles possess large magnetic saturation, 2.92 emu/g. The longitudinal (L-α_{ME}) and transverse (T-α_{ME}) magnetoelectric coupling coefficients have been found to be respectively 11.01, 10.35, 11.92, 13.18 mV/cm.Oe and 6.81, 6.85, 6.88, 7.86 mV/cm.Oe for x = 0, 0.05, 0.10, and 0.15.

- Pure and 15% rare earth metal ions (Gd^{3+}, Tb^{3+}, Dy^{3+})-doped $BiFeO_3$ nanoparticles, with average particle size, 25-46 nm have been synthesized. Structural study confirms that 15% mole fraction doping of the rare earth metal ions results in structural transformation from rhombohedral to orthorhombic phase and leads to contraction in lattice parameters, and unit cell volume. Magnetic study confirms their ferromagnetic character with the highest saturation magnetization in Dy-doped $BiFeO_3$ nanoparticles (Table 5.1). Dielectric measurements show that doped nanoparticles possess high dielectric constant. The doped-nanoparticles exhibit high magnetodielectric coefficient as compared to that for its pure form. The high value of saturation magnetization, 5.22 emu/g, dielectric constant, 900, and magnetodielectric coefficient, 5.82%, have been observed in case of Dy-doped $BiFeO_3$ nanoparticles.

Chapter 4: $BiFeO_3$ nanowires

presents the study of magnetoelectric coupling in pure and of rare earth metal ions (Gd^{3+}, Tb^{3+}, Dy^{3+}) doped-$BiFeO_3$ nanowires synthesized by colloidal dispersion template-assisted technique. For the comparative study nanowires of different size, viz., 100 nm (bulk in present case) as well as 20 nm have been synthesized.

- Pure $BiFeO_3$ nanowires having diameter, 20 nm, have been synthesized. XRD confirms their rhombohedral perovskite structure with R3*c* space group. Magnetic and electrical investigations confirm the ferromagnetic and ferroelectric behavior of synthesized nanowires, respectively, with low leakage-current density at room temperature. XRD, EDAX and XPS analyses reveal the phase purity of the synthesized nanowires. The high magnetoelectric coupling coefficients, viz., longitudinal, L-α_{ME} = 10.738 $mVcm^{-1}$.Oe, and transverse, T-α_{ME} = 6.866 $mVcm^{-1}$. Oe have been observed.
- Multiferroic properties of $Bi_{1-x}Tb_xFeO_3$ nanowires (x = 0, 0.05, 0.10 and 0.15) of diameter, 20 nm, as well as their comparison with their bulk counterpart (100 nm) have been studied. Synthesized nanowires exhibit size-dependent magnetic, electrical, dielectric and magnetoelectric properties. XRD confirms that the Tb-doping leads to structural transformation from rhombohedral to orthorhombic. Bulk nanowires display antiferromagnetic character having small saturation magnetization, 0.3 emu g^{-1} whereas the Tb-doped $BiFeO_3$ nanowires possess ferromagnetic character. Temperature- dependent magnetization study suggests their size-dependent spin-glass, ferro/ferri magnetic behavior.

XPS study rules out the presence of Fe^{2+}. A very high value of the magnetoelectric coupling, 7.2 %, has been noticed for 15% Tb-doped $BiFeO_3$ nanowires.

- Phase-dependent magnetic, electric, and multiferroic properties of pure and 15% Dy-doped $BiFeO_3$ nanowires have been investigated. XRD confirms that the doping of 15% Dy in $BiFeO_3$ nanowires leads to structural transformation from rhombohedral to orthorhombic. Magnetic study confirms that both pure and doped-$BiFeO_3$ nanowires exhibit ferromagnetic behavior and, the saturated magnetization increases with Dy-doping. Phase transformations, doping of Dy^{3+} ions as well as smaller size of synthesized nanowires generate structural distortion and stabilizes the 3+ oxidation state of Fe. Further, it reduces the leakage current by three orders and enhances the ferroelectric properties. In Dy-doped $BiFeO_3$ nanowires, high value of magnetodielectric coupling coefficient, 4.85 %, has been found.

Table 5.1A comparative study of multiferroic properties of synthesized nanostructures

Property → **Sample description** ↓	**Size (nm)**	**Magnetic saturation, M_s, (emu/g)**	**Dielectric constant**	**Magnetodielectric coupling coefficient (%)**
		$BiFeO_3$ nanoparticles		
Pure $BiFeO_3$	44	1.98	138	2.20
15 % Gd	46	3.00	412	3.47
15% Tb	25	4.38	643	4.36
15 % Dy	36	5.22	900	5.82
		$BiFeO_3$ nanowires		
Pure $BiFeO_3$	100	0.30	138	0.40
Pure $BiFeO_3$	20	3.18	88	2.60
15 % Gd	20	4.10	114	5.92
15% Tb	20	4.60	126	7.65
15 % Dy	20	5.48	140	8.90

- Template-assisted colloidal dispersion technique has been successfully employed for the synthesis of undoped and rare earth metal ions (Gd^{3+}, Tb^{3+}, Dy^{3+})-doped $BiFeO_3$ nanowires with 20 nm diameter. The crystallographic analysis confirms that the doping of rare earth ions results in structural transition from rhombohedral (R*3c*) to orthorhombic (P$n2_1a$) phase, i.e., polar-phase (R*3c*) to polar-phase (P$n2_1a$). Magnetic study reveals that the undoped and rare earth ion doped-$BiFeO_3$ nanowires possess ferromagnetic character with high saturation magnetization. Dy-doped $BiFeO_3$ nanowires show highest saturation magnetization and dielectric constant. The high magnetodielectric coupling coefficients, 2.60, 5.92, 7.65 and 8.9 percent, have been observed for undoped as well as the Gd, Tb and Dy-doped $BiFeO_3$ nanowires, respectively. Non-linear trend has been noticed in the rare earth-doped nanowires. Synthesized nanowires display excellent dielectric and magnetodielectric coupling with low dielectric loss, which may be useful in future nanoelectronics.

Table 5.1 presents comparative study of multiferroic properties of synthesized nanostructures. It shows that the $BiFeO_3$ nanostructures possess ferromagnetic character and, further doping of rare earth enhances the magnetic saturation. The doped $BiFeO_3$ nanowires possess high magnetic saturation and excellent magnetodielectric coupling coefficients compared to nanoparticles. The Table also reveals that the Dy-dopant is the best dopant.

6.2 Future scope

Multifunctional nanostructural multiferroics are the promising candidate materials for future s*pintronics, nanoelectronics, multi-state and high data storage memory devices* because of the fact that they simultaneously exhibit both electric and magnetic properties. The detailed study of mechanism responsible for magnetoelectric coupling in the nanostructures is required, for their incorporation into microelectronic/nanoelectronic devices.

Therefore, I propose to study in detail the implementation of multiferroics into micro/nanoelectronics and associated spin transport phenomena.

References

1. S.M. Mukhopadhyay, Nanoscale Multifunctional Materials: Science and Applications, Wiley Science, 1st Edition, 2011.
2. D.L. McDowell, J.H. Panchal, Hae-Jin Choi, C.C. Seepersad, J.K. Allen, F. Mistree, Integrated Design of Multiscale, Multifunctional Materials and Products, Elsevier, 1st Edition, 2009.
3. G.S. Lotey, N.K. Verma, Structural, magnetic, and electrical properties of Gd-doped $BiFeO_3$ nanoparticles with reduced particle size, Journal of Nanoparticles Research 14 (2012) 742.
4. J. F. Scott, Data storage: multiferroic memories, Nature Materials, 6 (4) (2007) 256–257.
5. J. F. Scott, C.A. Araujo, Ferroelectric memories, Science, 246 (4936) (1989)1400-1405.
6. G. A. Prinz, Magnetoelectronics, Science, 282 (5394) (1998)1660-1663.
7. C. Chappert, A. Fert, F.N. Van Dau, The emergence of spin electronics in data storage, Nature Materials, 6(11) (2007) 813-823.
8. S. X. Wang, A. M. Taratorin, Magnetic Information Storage Technology, Academic Press, Elsevier, 1st Edition, 1999.
9. A. Roy, R. Gupta, A. Garg, Multiferroic memories, Advances in Condensed Matter Physics, 2012 (2012) ID 926290.
10. M. Bibes, A. Barthélémy, Multiferroics: towards a magnetoelectric memory, Nature Materials, 7(6) (2008) 425-426.
11. A. Jaiswal, Introduction to nanomultiferroics: fabrication of magnetoelectrics and their size dependent tunable properties, 1st Edition, LAP LAMBERT Academic Publishing, 2012.
12. F. Nasirpouri, A. Nogaret, Nanomagnetism and spintronics: Fabrication, Materials, Characterization and Applications, 1st Edition, World Scientific, 2010.
13. E. Roduner, Nanoscopic materials: Size-Dependent Phenomena, 1st Edition, Royal Society of Chemistry, 2006.
14. H. Schmid, Multi-ferroic magnetoelectrics, Ferroelectrics, 162 (1994) 317-368.
15. N.A. Hill, Why Are There so Few Magnetic Ferroelectrics?, The Journal of Physical Chemistry B, 104 (2000) 6694-6709.
16. N.A. Hill, Density Functional Studies Of Multiferroic Magnetoelectrics, Annual Review of Materials Research 32 (2002) 1-37.
17. P. Curie, Sur La Symétrie Dans Les Phénomènes Physiques, Symétrie D'un Champ

Électriglue Et D'un Champ Magnétique, Journal de Physique, 3 (1894)393-415

18. I. E. Dzyaloshinskii, Topological model of a heisenberg spin glass, Journal of Experimental and Theoretical Physics Letters, 37(4) (1983) 227-229 [English version of Zhurnal Eksperimental'noi i Teoreticheskoi Fiziki, 37 (4) (1983) 190-192]

19. (a) D.N. Astrov, The magnetoelectric effect in antiferromagnetics, Journal of Experimental and Theoretical Physics Letters, 11 (1960) 708–709 [English version of Zhurnal Eksperimental'noi i Teoreticheskoi Fiziki, 38 (1960) 984-985]. (b) D.N. Astrov, Magnetoelectric effect in chromium oxide, Journal of Experimental and Theoretical Physics Letters 13 (1961) 729-733 [English version of Zhurnal Eksperimental'noi i Teoreticheskoi Fiziki 40 (1961) 1035-1041].
20. E. Ascher, H. Rieder, H. Schmid, H. Stössel, Some Properties of Ferromagnetoelectric Nickel-Iodine Boracite, $Ni_3B_7O_{13}I$, Journal of Applied Physics 37(3) (1966)1404.
21. N. Mufti, Magnetic and Electric Response in Multiferroic Manganites (2008) Zernike Institute for Advanced Materials, University of Groningen, ISSN 1570-1530 (ISBN No: 978-90-367-3673-2).
22. C. Chappert, A. Fert, F.N.V. Dau, The emergence of spin electronics in data storage, Nature Materials 6 (2007) 813-823.
23. M. Fiebig, Revival of the magnetoelectric effect, Journal of Physics D: Applied Physics, 38 (8) (2005) R123–R152
24. N.A. Spaldin, M. Fiebg, The Renaissance of Magnetoelectric Multiferroics, Science. 309 (5733) (2005) 391-392.
25. T.J. Park, G.C. Papaefthymiou, A.J. Viescas, A.R. Moodenbaugh, S.S. Wong, Size-dependent magnetic properties of single-crystalline multiferroic $BiFeO_3$ nanoparticles, Nano Letter 7 (3) (2007) 766-772.
26. R.K. Govind, V.H. Babu, C.-T. Chiang, E. Magnano, F. Bondino, R. Denecke, K.-M. Schindler, Magnetic properties of self-assembled Fe nanoislands on $BaTiO_3$(001), Journal of Magnetism and Magnetic Materials, 346 (2013) 16-20.
27. H. Béa, S. Fusil, K. Bouzehouane, M. Bibes, M. Sirena, G. Herranz, E. Jacquet, J. -P. Contour and A. Barthélémy, Ferroelectricity down to at least 2 nm in multiferroic $BiFeO_3$ epitaxial thin films, Japanese Journal of Applied Physics, 45 (2006) L187-L189.

28. G.S. Lotey, S. Kumar, N.K. Verma, Fabrication and Electrical Characterization of Highly Ordered Copper Nanowires, Applied Nanoscience, 2 (1) (2012) 7-13.
29. A. Gruverman, D. Wu, H. Lu, Y. Wang, H. W. Jang, C.M. Folkman, M.Y. Zhuravlev, D. Felker, M. Rzchowski, C.-B. Eom, E.Y. Tsymbal, Tunneling Electroresistance Effect in Ferroelectric Tunnel Junctions at the Nanoscale" Nano Letter 9 (10) (2009) 3539-3543.
30. S.M. Selbach, T. Tybell, M. Einarsrud, T. Grande, Size-Dependent Properties of Multiferroic $BiFeO_3$ Nanoparticles, Chemistry of Materials, **19** (26) (2007) 6478-6484.
31. H. Béa, M. Bibes, S. Cherifi, F. Nolting, B. Warot-Fonrose, S. Fusil, G. Herranz, C. Deranlot, E. Jacquet, K. Bouzehouane and A. Barthélémy, Tunnel magnetoresistance and robust room temperature exchange bias with multiferroic $BiFeO_3$ epitaxial thin films, Applied Physics Letter, 89 (2006) 242114
32. M.D. Biegalski, D.H. Kim, S. Choudhury, L.Q. Chen, H.M. Christen, K. Dörr, Strong strain dependence of ferroelectric coercivity in a $BiFeO_3$ film, Applied Physics Letter 98 (2011) 142902.
33. M. Forshaw, R. Stadler, D. Crawley, K. Nikolić, A short review of nanoelectronic Architectures, Nanotechnology 15 (2004) S220-S223.
34. W. Eerenstein, N.D. Mathur, J.F. Scott, Multiferroic and magnetoelectric materials, Nature 442 (2006) 759-765.
35. H. Béa, M. Bibes, F. Ott, B. Dupe, X. H. Zhu, S. Petit, S. Fusil, C. Deranlot, K. Bouzehouane and A. Barthélémy, Mechanisms of exchange bias with multiferroic $BiFeO_3$ epitaxial thin films, Physical Review Letters, 100 (2008) 017204.
36. J. Wang, J.B. Neaton, H. Zheng, V. Nagarajan, S.B. Ogale, B. Liu, D. Viehland, V. Vaithyanathan, D.G. Schlom, U.V. Waghmare, N.A. Spaldin, K.M. Rabe, M. Wuttig, R. Ramesh, Epitaxial $BiFeO_3$ Multiferroic Thin Film Heterostructures, Science, 299 (5613) (2003)1719-1722.
37. NA Hill, Density Functional Studies of Multiferroic Magnetoelectrics, Annual Review of Materials Research, 32 (2002)1-37.
38. Y.K. Jeong, C.W. Bark, S. Ryu, J.-H. Lee, H.M. Jang, *R3c-R3m* Octahedron-tilting Transition in Rhombohedrally-distorted $BiFeO_3$ Multiferroics, Journal of the Korean Physical Society, 58(4) (2011) 817-820.
39. B. Ruette, S. Zvyagin, A. P. Pyatakov, A. Bush, J. F. Li, V. I. Belotelov, A. K. Zvezdin, D.

Viehland, Magnetic-field-induced phase transition in $BiFeO_3$ observed by high-field electron spin resonance : Cycloidal to homogeneous spin order, Physical Review B, 69 (2004) 064114.

40. G. Catalan, J.F. Scott, Physics and Applications of Bismuth Ferrite, Advanced Materials, 21(24) (2009) 2463-2485.
41. C.-W. Nan, M.I. Bichurin, S. Dong, D. Viehland, G. Srinivasan, Multiferroic magnetoelectric composites: Historical perspective, status, and future directions, Journal of Applied Physics, 103 (2008) 031101.
42. D.I. Khomskii, Multiferroics: Different ways to combine magnetism and ferroelectricity, Journal of Magnetism and Magnetic Materials, 306(1) (2006) 1-8.
43. Z. Shi, C. Wang, X. Liu, C.-W, Nan, A four-state memory cell based on magnetoelectric composite, Chinese Science Bulletin, 53(14) (2008) 2135-2138.
44. A.M. Kadomtseva, Y.F. Popov, A.P. Pyatakov, G.P. Vorob´ev, A. K. Zvezdin, D. Viehland, Phase transitions in multiferroic $BiFeO_3$ crystals, thin-layers, and ceramics: enduring potential for a single phase, room-temperature magnetoelectric 'holy grail, Phase Transitions: A Multinational Journal, 79(12) (2006) 1019-1042.
45. http://dissertations.ub.rug.nl/FILES/faculties/science/2008/d.fausti/02-c2.pdf
46. C. Tabares-Munoz, J.-P. Rivera, A. Bezinges, A. Monnier, H. Schmid, Measurement of the Quadratic Magnetoelectric Effect on Single Crystalline $BiFeO_3$, Japanese Journal of Applied Physics, 24(2) (1985) 1051-1053.
47. J. R. Teague, R. Gerson, W.J. James, Dielectric Hysteresis in Single Crystal $BiFeO_3$, Solid State Communication, 8 (13) (1970) 1073-1074.
48. P. Ravindran, R. Vidya, A. Kjekshus, H. Fjellvåg, O. Eriksson, Theoretical investigation of magnetoelectric behavior in $BiFeO_3$, Physical Review B, 74(22) (2006) 224412.
49. Y. F. Popov, A. K. Zvezdin, G.P. Vorob´ev, A. M. Kadomtseva, V.A. Murashev, D. N. Rakov, Linear magnetoelectric effect and phase transitions in bismuth ferrite $BiFeO_3$, Journal of Experimental and Theoretical Physics, 57 (1993) 69-73.
50. C. Ederer, N.A. Spaldin, Weak ferromagnetism and magnetoelectric coupling in bismuth ferrite, Physical Review B, 71(6) (2005) 060401(R).
51. P. Rovillain, M. Cazayous, Y. Gallais, A. Sacuto, R.P.S.M. Lobo, D. Lebeugle, D. Colson, Polar phonons and spin excitations coupling in multiferroic $BiFeO_3$ crystals, Physical

Review B, 79(18) (2009)180411(R).

52. D. Lebeugle, D. Colson, A. Forget, M. Viret, A. M. Bataille, A. Gukasov, Electric-Field-Induced Spin Flop in $BiFeO_3$ Single Crystals at Room Temperature, Physical Review Letter, 100(22) (2008) 227602.
53. T. Zhao, A. Scholl, F. Zavaliche, K. Lee, M. Barry, A. Doran, M.P. Cruz, Y.H. Chu, C. Ederer, N.A. Spaldin, R. R. Das, D. M. Kim, S. H. Baek, C.B. Eom, R. Ramesh, Electrical control of antiferromagnetic domains in multiferroic $BiFeO_3$ films at room temperature" Nature Materials, 5 (2006) 823-829.
54. J.C. Wojdeł, J. Íñiguez, Magnetoelectric Response of Multiferroic $BiFeO_3$ and Related Materials from First-Principles Calculations, Physical Review Letter, 103 (26) (2009) 267205.
55. A.K. Zvezdin, A.M. Kadomtseva, S.S. Krotov, A.P. Pyatakov, Y.F. Popov, G.P. Vorob'ev, Journal of Magnetism and Magnetic Materials, 300 (1) (2006) 224-228.
56. Y.-H. Chu, L.W. Martin, M.B. Holcomb, M. Gajek, S.-J. Han, Q. He, N. Balke, C.-H. Yang, D. Lee, W. Hu, Q. Zhan, P.-L.Yang, A.F.-Rodríguez, A. Scholl, S.X. Wang, R. Ramesh, Electric-field control of local ferromagnetism using a magnetoelectric multiferroic, Nature Materials 7 (2008) 478-482.
57. N. Wang, J. Cheng, A. Pyatakov, A.K. Zvezdin, J.F. Li, L.E. Cross, D. Viehland, Multiferroic properties of modified $BiFeO_3$-$PbTiO_3$-based ceramics: Random-field induced release of latent magnetization and polarization, Physical Review B, 72(10) (2005)104434.
58. F. Bai, J. Wang, M. Wuttig, J.F. Li, N. Wang, A. P. Pyatakov, A. K. Zvezdin, L. E. Cross, D. Viehland, Destruction of spin cycloid in (111)c-oriented $BiFeO_3$ thin films by epitiaxial constraint: Enhanced polarization and release of latent magnetization, Applied Physics Letter, 86 (3) (2005) 032511.
59. G.S. Lotey, N.K. Verma, Magnetoelectric coupling in multiferroic Tb-doped $BiFeO_3$ nanoparticles, Materials Letter, 111 (2013) 55-58.
60. G.S. Lotey, N.K. Verma, Gd-doped $BiFeO_3$ nanoparticles - A novel material for highly efficient dye-sensitized solar cells, Chemical Physics Letters 574 (2013) 71-77.
61. G.S. Lotey, N.K. Verma, Structural, electrical, magnetic and multiferroism in Dy-doped $BiFeO_3$ nanoparticles, AIP Conference Proceeding 1536 (2013) 55-56.
62. G.S. Lotey, N.K. Verma, Magnetodielectric properties of rare earth metal-doped $BiFeO_3$

nanoparticles, Journal of Materials Science: Materials in Electronics, 24 (2013) 3723-3729.

63. (a) K. Takahashi, Y. Wang, K. Lee, G. Cao, Fabrication and Li^+-interaction properties of V_2O_5–TiO_2 composite nanorod arrays, Applied Physics A, 82 (2006) 27-31. (b) Y. Wang, G. Cao, Synthesis and electrochemical properties of $InVO_4$ nanotube arrays, Journal of Materials Chemistry, 17 (2007) 894-899.
64. G.S. Lotey, N.K. Verma, Phase-dependent multiferroism in Dy-doped $BiFeO_3$ nanowires, Superlattices and Microstructures 53 (2013)184-194.
65. G.S. Lotey, N.K. Verma**,** Multiferroic properties of Tb-doped $BiFeO_3$ nanowires Journal of Nanoparticle Research 15 (2013) 1553
66. G.S. Lotey, N.K. Verma, Multiferroism in rare earth metals-doped $BiFeO_3$nanowires, Superlattices and Microstructures 60 (2013) 60-66.
67. G. Cao, Y. Wang, Nanostructures and Nanomaterials: Synthesis, Properties, and Applications, 2nd Edition, World Scientific, 2011.
68. W.D. Callister, Materials science and engineering: An introduction, 7th Edition John Willey and Sons Inc., 2007.
69. V.K. Pecharsky, P.Y. Zavalij, Fundamentals of powder diffraction and structural characterization of materials, 2nd Edition, Springer Science, 2009.
70. B.D. Cullity, S.R. Stock, Elements of X-ray Diffraction, 3rd Edition, Prentice Hall, 2011.
71. J.F. Moulder, W.F. Stickle, P.E. Sobol, and K.D. Bomben, Handbook of x-ray photoelectron spectroscopy, Perkin-Elmer Corp.,1992.
72. B.V. Crist, Handbook of Monochromatic XPS Spectra: The Elements and Native Oxides, Wiley, USA, (2000).
73. J. Goldstein , D. E. Newbury, D.C. Joy, C.E. Lyman, P. Echlin, E. Lifshin, L. Sawyer, J.R. Michael, Scanning Electron Microscopy and X-Ray Microanalysis, 3rd Edition, Kluwer Academic/Plenum Publishers, 2003.
74. B. Fultz, J. Howe, Transmission Electron Microscopy and Diffractometry of Materials, 4th Edition, Springer, 2013.
75. J. Clarke, A.I. Braginski, The SQUID Handbook: fundamentals and technology of SQUIDs and SQUID systems, 1st Edition, Wiley VCH, 2004.
76. A.J. Moulson, J.M. Herbert, Electroceramics: Materials, Properties, Applications, 2nd Edition, Wiley, 2003.

77. K.C. Kao, Dielectric phenomena in solids, 1st Edition, Elsevier, 2004.
78. H. Yang, H. Wang, J. Yoon, Y. Wang, M. Jain, D.M. Feldmann, P.C. Dowden, J.L. MacManus-Driscoll, Q. Jia, Vertical Interface Effect on the Physical Properties of Self-Assembled Nanocomposite Epitaxial Films, Advanced Materials, 21(37) (2009) 3794-3798.
79. G.S.Lotey, N.K. Verma, Magnetoelectric coupling in multiferroic BiFeO3 nanowires, Chemical Physics Letters 579 (2013) 78-84.
80. G.V. Duong, R. Groessinger, M. Schoenhart, D.B. Basques, The Lock-In Technique For Studying Magnetoelectric Effect, Journal of Magnetism and Magnetic Materials, 316 (2) (2007) 390-393.
81. V.B. Naik, R. Mahendiran, Magnetic and magnetoelectric studies in pure and cation doped $BiFeO_3$, Solid State Communication, 149 (19-20) (2009) 754-758.
82. J.M. Caicedo, J.A. Zapata, M.E. Gómez, P. Prieto, Magnetoelectric coefficient in $BiFeO_3$ compounds, Journal of Applied Physics 103 (2008) 07E306.
83. V.A. Khomchenko, V.V. Shvartsman, P. Borisov, W. Kleemann, D.A. Kiselev, I.K. Bdikin, J.M. Vieira, A.L. Kholkin, Effect of Gd substitution on the crystal structure and multiferroic properties of $BiFeO_3$, Acta Materialia, 57 (2009) 5137-5145.
84. R. Guo, L. Fang, W. Dong, F. Zheng, M. Shen, Enhanced Photocatalytic Activity and Ferromagnetism in Gd Doped $BiFeO_3$ Nanoparticles, Journal Physical Chemistry C, 144 (49) (2010) 21390-21396.
85. A. Jaiswal, R. Das, K. Vivekanand, P. Abraham, S. Adyanthaya, P. Poddar, Effect of Reduced Particle Size on the Magnetic Properties of Chemically Synthesized $BiFeO_3$ Nanocrystals, Journal Physical Chemistry C, 114(5) (2010) 2108-2115.
86. Reetu, A. Agarwal, S. Sanghi, Ashima, N. Ahlawat, Monica, Phase transformation, dielectric and magnetic properties of Nb doped $Bi_{0.8}Sr_{0.2}FeO_3$ multiferroics, Journal of Applied Physics, 111(11) (2012) 113917.
87. B. Bhushan, A. Basumallick, N.Y. Vasanthacharya, S. Kumar, D. Das, Sr induced modification of structural, optical and magnetic properties in $Bi_{1-x}Sr_xFeO_3$ (x = 0, 0.01, 0.03, 0.05 and 0.07) multiferroic nanoparticles, Solid State Sciences, 12 (7) (2010) 1063-1069.
88. G.D. Hu, S.H. Fan, C.H. Yang, W.B. Wu, Low leakage current and enhanced ferroelectric properties of Ti and Zn codoped $BiFeO_3$ thin film, Applied Physics Letter, 92 (2008)192905.
89. R. Das, A. Jaiswal, S. Adyanthaya, P. Poddar, Effect of particle size and annealing on spin

and phonon behavior in $TbMnO_3$, Journal of Applied Physics, 109 (2011) 064309.

90. Y.P. Wang, L. Zhou, M.F. Zhang, X.Y. Chen, J.-M. Liu, Z.G. Liu, Room-temperature saturated ferroelectric polarization in $BiFeO_3$ ceramics synthesized by rapid liquid phase sintering, Applied Physics Letter, 84(2004)1731.
91. K. Abe, N. Sakai, J. Takahashi, H. Itoh, N. Adachi, T. Ota, Leakage Current Properties of Cation-Substituted $BiFeO_3$ Ceramics, Japanese Journal of Applied Physics, 49(9) (2010) 09MB01.
92. R. Schmidt, W. Eerenstein, T. Winiechi, F.D. Morrison, P.A. Midgley, Impedance spectroscopy of epitaxial multiferroic thin films, Physical Review B, 75(24) (2007) 24511.
93. K.M. Rabe, C.H. Ahn, J.-M. Triscone, Physics of Ferroelectrics: A Modern Perspective, Springer, 2007.
94. Y. Zhang, H. Zhang, J. Yin, H. Zhang, J. Chen, W. Wang, G. Wu, Structural and magnetic properties in $Bi_{1-x}R_xFeO_3$ (x=0-1, R=La, Nd, Sm, Eu and Tb) polycrystalline ceramics, Journal of Magnetism and Magnetic Materials, 322 (15) (2010) 2251-2255.
95. P. Singh, A. Agarwal, S Sanghi,N. Singh, S. Khasa, Study of $(Bi_2O_3)(Ba_xMo_{1-x}O_3)$ polycrystalline ceramic as relaxor ferroelectric, Physica B: Condensed Matter. 407 (24) (2012) 4752-4759.
96. D. Pandey, A. Singh, Structure, synthesis and multiferroic nature of $BiFeO_3$ and $_{0.9}BiFeO_3$-$0.1BaTiO_3$: An overview, Bulletin of Materials Science, 32(3)(2009)361-367.
97. K.F. Wang, J.-M. Liu, Z.F. Ren, Multiferroicity: the coupling between magnetic and polarization orders, Advances in Physics, 58(4) (2009) 321.
98. L. Neel, Compt. Rend, 253 (1961) 9.
99. L. Neel, Compt. Rend, 253 (1961) 203.
100. P. Uniyal, K.L. Yadav, Room temperature multiferroic properties of Eu doped $BiFeO_3$ Journal of Applied Physics, 105(7) (2009) 07D914.
101. R. Mazumder, P.S. Devi, D. Bhattacharya, P. Choudhury, A. Sen, M. Raja,Ferromagnetism in nanoscale BiFeO3, Applied Physics Letter, 91(6) (2007) 62510.
102. F. Gao, X.Y. Chen, K. Yin, S. Dong, Z. Ren, F.Yuan, T.Yu, Z. Zou, J.-M. Liu, Visible-Light Photocatalytic Properties of Weak Magnetic BiFeO3 Nanoparticles, Advanced Material 19(19) (2007) 2889-2892.
103. B. Bhushan, A. Basumallick, S.K. Bandopadhyay, N.Y. Vasanthacharya, D. Das, Effect of

alkaline earth metal doping on thermal, optical, magnetic and dielectric properties of $BiFeO_3$ nanoparticles, Journal of Physics D: Applied Physics, 42(6) (2009) 06500.

104. R. Mazumder, S. Ghosh, P. Mondal, D. Bhattacharya, S. Dasgupta, N. Das, A. Sen, A.K. Tyagi, M. Sivakumar, T. Takami, H. Ikuta, Particle size dependence of magnetization and phase transition near T_N in multiferroic $BiFeO_3$, Journal of Applied Physics ,100(3) (2006) 033908.
105. S. Karimi, I.M. Reaney, Y. Han, J. Pokorny, I. Sterianou, Crystal chemistry and domain structure of rare-earth doped $BiFeO_3$ ceramics, Journal Materials Science 44 (19)(2009) 5102-5112.
106. T. Karthik, T.D. Rao, A. Srinivas, S. Asthana , A-Site Cation disorder and Size variance effects on the physical properties of multiferroic $Bi_{0.9}RE_{0.1}FeO_3$ Ceramics (RE =Gd^{3+},Tb^{3+},Dy^{3+}), arXiv:1206.5606, (2012).
107. Y. Yao, W. Liu, Y. Chan, C. Leung, C. Mak, B. Ploss, Studies of Rare-Earth-Doped $BiFeO_3$ Ceramics, International Journal of Applied Ceramic Technology, 8(5) (2011) 1246-1253.
108. L. Neel, Compt. Rend, 252 (1961) 4075-4080.
109. W.M. Zhu, L.W. Su, Z.G. Ye, W. Ren, Enhanced magnetization and polarization in chemically modified multiferroic (1-x)$BiFeO_3$–x$DyFeO_3$ solid solution, Applied Physics Letter, 94(14) (2009)142908.
110. J .C. Maxwell, Electricity and Magnetism, Oxford University Press, 1973.
111. C.G. Koops, On the Dispersion of Resistivity and Dielectric Constant of Some Semiconductors at Audio frequencies, Physical Review, 83(1951) 121-124.
112. B.H. Park, B.S. Kang, S.D. Bu, T.W. Noh, J. Lee, W. Jo, Lanthanum-substituted bismuth titanate for use in non-volatile memories, Nature, **401** (1999) 682-684.
113. D. R. Patil, S. A. Lokare, R. S. Devan, S. S. Chougule, C. M. Kanamadi, Y. D. Kokekar, B. K. Chougule, Studies on electrical and dielectric properties of $Ba_{1-x}Sr_xTiO_3$, Materials Chemistry and Physics, 104 (2-3) (2007) 254-257.
114. S.K. Pradhan, B.K. Roul, Effect of Gd doping on structural, electrical and magnetic properties of $BiFeO_3$ electroceramic, Journal of Physics and Chemistry of Solids, 72(10) (2011) 1180-1187.
115. S. Goswami, D. Bhattacharya, P. Choudhury, B. Ouladdiaf, T. Chatterji, Multiferroic

coupling in nanoscale $BiFeO_3$, Applied Physics Letter, **99(7) (2011)** 073106.

116. S.H. Xie, J.Y. Li, R. Proksch, Y.M. Liu, Y.C. Zhou, Y.Y. Liu, Y. Ou, L.N. Lan, Y. Qiao, Nanocrystalline multiferroic $BiFeO_3$ ultrafine fibers by sol-gel based electrospinning, Applied Physics Letter, 93(22) (2008) 222904.
117. S. Shetty, V.R. Palkar, R. Pinto, Size effect study in magnetoelectric $BiFeO_3$ system, PRAMANA – Journal of Physics **58** (5 & 6) (2002)1027.
118. D.P Dutta, B.P. Mandal, R. Naik, G. Lawes, A.K. Tyagi, Magnetic, Ferroelectric, and Magnetocapacitive Properties of Sonochemically Synthesized Sc-Doped $BiFeO_3$ Nanoparticles, Journal of Physical Chemistry C,117 (5) (2013) 2382-2389.
119. G. Catalan, Magnetocapacitance without magnetoelectric coupling, Applied Physics Letter, 88(10) (2006) 102902.
120. V. M. Petrov, G. Srinivasan, M. I. Bichurin, A Gupta, Theory of magnetoelectric effects in ferrite piezoelectric nanocomposites, Physical Review B, 75(22) (2007) 224407.
121. E. A. Eliseev, A. N. Morozovska, M. D. Glinchuk, B. Y. Zaulychny, V. V. Skorokhod, R. Blinc, Surface-induced piezomagnetic, piezoelectric, and linear magnetoelectric effects in nanosystems, Physical Review B 82(8) (2010) 085408.
122. T. N. Narayanan, B. P. Mandal, A. K. Tyagi, A. Kumarasiri, X. Zhan, M. G. Hahm, M. R. Anantharaman, G. Lawes, P.M. Ajayan, Hybrid Multiferroic Nanostructure with Magnetic−Dielectric Coupling, Nano Letter, 12(6)(2012)3025-3030.
123. K. Prashanthi, P.M. Shaibani, A. Sohrabi, T.S. Natarajan, T. Thundat, Nanoscale magnetoelectric coupling in multiferroic $BiFeO_3$ nanowires, Physica Status Solidi (RRL) - Rapid Research Letters, 6(6) (2012) 244–246.
124. B. Liu, B. Hu, Z. Du, Hydrothermal synthesis and magnetic properties of single-crystalline $BiFeO_3$ nanowires, Chemical Communications, 47 (2011) 8166–8168.
125. X. Zhang, H. Liu, B. Zheng, Y. Lin, D. Liu, C.-W. Nan, Photocatalytic and Magnetic Behaviors Observed in $BiFeO_3$ Nanofibers by Electrospinning, Journal of Nanomaterials, 2013 (2013)917948.
126. Y. Zhao, J. Miao, X. Zhang, Y. Chen, X.G. Xu, Y.J. Jiang, Ultra-thin $BiFeO_3$ nanowires prepared by a sol–gel combustion method: an investigation of its multiferroic and optical properties, Journal of Materials Science: Materials in Electronics, 23(2012) 180–184.
127. T.J. Park, Y. Mao, S.S. Wong, Synthesis and characterization of multiferroic $BiFeO_3$

nanotubes, Chemical Communications, 23 (2004) 2708-2709.

128. W. Jing, L.M. Ya, L.X. Lian, P. Ling, L. Jun, Y.B. Fang, Z.X. Zhong, Synthesis and Multiferroic Properties of $BiFeO_3$ Nanotubes, Chinese Physics Letters, 26(11) (2009) 117301.
129. D. Fiorani, Surface Effects in Magnetic Nanoparticles, Springer, 2005.
130. X.Y. Zhang, C.W. Lai, X. Zhao, D.Y. Wang, J.Y. Dai, Synthesis and ferroelectric properties of multiferroic $BiFeO_3$ nanotube arrays, Applied Physics Letter, 87 (2005) 143102.
131. I. Sosnowska, T.P. Neumaier, E. Streichele, Spiral magnetic ordering in bismuth ferrite, Journal of Physics C: Solid State Physics, 15 (23)(1982) 4835-4846.
132. W.H. Rothery, R.E. Smallman, C.W. Haworth, The Structure of Metals and Alloys, Metals & Metallurgy Trust., (1969).
133. S.K. Singh, H. Ishiwara, Doping Effect of Rare-Earth Ions on Electrical Properties of $BiFeO_3$ Thin Films Fabricated by Chemical Solution Deposition, Japanese Journal Applied Physics 45(4B) (2006) 3194-3197.
134. J. Liu, L. Fang, F. Zheng, S. Ju, M. Shen, Enhancement of magnetization in Eu doped BiFeO3 nanoparticles, Applied Physics Letter, 95(2) (2009) 022511.
135. S. Cavdar, H. Koralay, N. Tugluoglu, A. Gunen, Frequency-dependent dielectric characteristics of Tl–Ba–Ca–Cu–O bulk superconductor, Superconductor Science and Technology, 18(9) (2005)1204–1209.
136. L.L. Hench, J.L.West, Principles of Electronic Ceramic. Wiley, 1990.
137. G.L. Song, H.X. Zhang, T.X. Wang, H.G. Yang, F.G. Chang, Effect of Sm, Co codoping on the dielectric and magnetoelectric properties of $BiFeO_3$ polycrystalline ceramics, Journal of Magnetism and Magnetic Materials 324 (13) (2012) 2121-2126.
138. J. Xu, G. Wang, H. Wang, D. Ding, Y. He, Synthesis and weak ferromagnetism of Dy-doped $BiFeO_3$ powders, Materials Letters, 63 (11) (2009) 855-857.
139. F.Z. Qian, J.S. Jiang, S.Z. Guo, D.M. Jiang, W.G. Zhang, Multiferroic properties of $Bi_{1-x}Dy_xFeO_3$ nanoparticles, Journal of Applied Physics, 106(8) (2009) 084312.
140. Y. Li, J. Yu, J. Li, C. Zheng, Y. Wu, Y. Zhao, M. Wang, Y. Wang, Influence of Dy-doping on ferroelectric and dielectric properties in $Bi_{1.05-x}Dy_xFeO_3$ ceramics, Journal of Materials Science: Materials in Electronics, 22(4) (2011) 323-327.

141. R. Das, G.G. Khan, K. Mandal, Pr and Cr co-doped $BiFeO_3$ nanotubes: an advance multiferroic oxide material, EPJ Web of Conference, 40 (2013) 15015.

142. J. Wang, M. Li, X. Liu, P. Pei, J. Liu, B. Yu, X. Zhao, Synthesis and ferroelectric properties of Nd doped multiferroic $BiFeO_3$ nanotubes, Chinese Science Bulletin, 55 (16) (2010) 1594-1597.

143. D. Kan, L. Pálová, V. Anbusathaiah, C.J. Cheng, S. Fujino, V. Nagarajan, K.M. Rabe KM, I. Takeuchi, Universal Behavior and Electric-Field-Induced Structural Transition in Rare-Earth-Substituted $BiFeO_3$, Advanced Functional Materials, 20 (7) (2010) 1108-1115.

144. S. Kumar, Structural, dielectric and magnetic characterization of large scale template synthesized Gd doped $BiFeO_3$ nanowires, Journal of Materials Science: Materials in Electronics, 24 (6) (2013) 2112-2115.

145. S.H. Johnson, P. Finkel, O.D. Leaffer, S.S. Nonnenmann, K. Bussmann, J. E. Spanier, Magneto-elastic tuning of ferroelectricity within a magnetoelectric nanowire, Applied Physics Letter, 99 (2011) 182901.

146. J. Dho, X.Qi, H. Kim, J.L. MacManus-Driscoll, M.G. Blamire, Large Electric Polarization and Exchange Bias in Multiferroic $BiFeO_3$, Advanced Materials, 18 (11) (2006) 1445-1448.